Investigations of Redox-Labeled Silica and Gold Nanoparticles in Solution and as Films on Electrodes

Christopher A. Beasley

A dissertation submitted to the faculty of the University of North Carolina at Chapel Hill in partial fulfillment of the requirements for the degree of Doctorate of Philosophy in the Department of Chemistry (Analytical Chemistry).

Chapel Hill

2010

Approved by,

Advisor: Dr. Royce W. Murray

Reader: Dr. R. Mark Wightman

Reader: Dr. Mark H. Schoenfisch

Committee Member: Dr. Thomas J. Meyer

Committee Member: Dr. Wei You

Abstract

Christopher A. Beasley: Investigations of Redox-Labeled Silica and Gold Nanoparticles in Solution and as Films on Electrodes

(Under the direction of Dr. Royce W. Murray)

Chapter One serves as a background for Au nanoparticles (AuNP) and silica nanoparticles (SiNP). A brief history of the synthesis and characterization of AuNPs will be followed by a discussion on the recent application of the particles in sensing and energy-related applications. The second portion of the chapter will be a discussion on the functionalization of SiNPs and their application in a variety of sensing systems.

Chapter Two discusses the irreversible adsorption onto electrode surfaces of highly ionic, mixed-monolayer AuNPs containing an N,N,N-triethylammonium terminated thiol and an 6-(ferrocenylhexane) thiol. The AuNP films are entropically stabilized due to the multidentate nature of the particles and can be transferred to *NP-free* electrolyte solutions for further investigation. The most interesting aspect of the film is the ability to monitor ion and accompanying solvent transfer between the film and electrolyte solution despite the films being one to two monolayers thick. Comparisons will be drawn to ion transfer between two immiscible electrolyte solutions.

Chapter Three will discuss the controlled growth of films of highly ionic, mixed monolayer AuNPs containing deprotonated mercaptoundecanoic acid and 6-(ferrocenylhexane) thiol.

The controlled deposition of films of AuNPs without the addition of a metal ion to facilitate binding between particles provides a new route to controlling film thicknesses for applications in Surface Enhanced Raman Spectroscopy and energy storage. Electrochemical quartz crystal microbalance studies, impedance spectroscopy and theoretical modeling show that the large peak-to-peak separation for the ferrocene/ferrocenium couple in cyclic voltammograms arises solely from uncompensated resistance effects within the film, i.e., the rates of ion permeation.

Chapter Four examines ferrocenated SiNPs as charge storage devices. Focus is initially on the surface functionalization. Spectroscopic characterizations are used to estimate the number ferrocenes per particle. Next, a variety of electrochemical investigations confirm that approximately 600 ferrocenes reside on the surface of the particles. Several interesting investigations are discussed relating to formation of a slurry of SiNPs upon addition of supporting electrolyte or acetonitrile for electrochemical investigations. Despite the formation of the slurry, reproducible electrochemistry was obtained.

Table of Contents

List of Tables

List of Figures

List of Abbreviations and Symbols

2D	Two-Dimensional
3D	Three-Dimensional
A	Absorbance
	Amperes
	Electrode area
abbr.	abbreviation
Ag	Silver
Ag/AgQRE	Silver quasi-reference electrode
Ag/AgCl (aq)	Siliver-silver chloride aqueous reference electrode
Au	Gold
$AuCl_4^-$	Tetrachloroaurate
Au(I)-SR	Au(I) thiolate
a	Atto-
aF	AttoFarad
β-CD	Beta-cyclodextrin
BH_4^-	Borohydride

Bu_4NClO_4	Tetrabutylammonium perchlorate
Bu_4NPF_6	Tetrabutylammonium hexafluorophosphate
C	Carbon
	Concentration
	Coulombs
°C	Degrees Celsius
CD_2Cl_2	Deuterated methylene chloride
CH_2	Methylene group
CH_2Cl_2	Methylene chloride (or dichloromethane)
CH_3	Methyl group
CH_3CN	Acetonitrile
Cn	Alkanethiol with n carbon atoms
COOH	Carboxylic acid group
CV	Cyclic voltammetry
ca.	About
cm	Centimeter
D	Diffusion coefficient
D_{APP}	Apparent diffusion coefficient
D_E	Diffusion coefficient of an electron
D_{PHYS}	Physical diffusion coefficient
D_{NP}	NP diffusion coefficient

d	Diameter
	Length of NP monolayer
E	Potential
ΔE_{peak}	Potential difference between anodic and cathodic peaks
E^o	Formal potential
E^0_{APP}	Apparent Formal Potential
$E_{1/2}$	Electrochemical half-wave potential
EQCM	Electrochemical Quartz Crystal Microbalance
e	Electronic charge
e^-	Electron
equiv	Equivalent
eV	Electron volts
exp	Exponential
F	Farad
	Faraday constant
μF	MicroFarad
Fc	ferrocene
Fc^+	ferrocenium
FTIR	Fourier Transform Infrared Spectroscopy
g	Gram
H	Hydrogen
^1H NMR	Proton Nuclear Magnetic Resonance Spectroscopy
H_2O	Water

H_2SO_4	Sulfuric acid
$HAuCl_4 \bullet xH_2O$	Tetrachloroauric acid hydrate
HO	Alcohol group
HOOC	Carboxylic acid group
HOMO	Highest occupied molecular orbital
HRTEM	High-Resolution Transmission Electron Microscopy
HSC6	Hexanethiol
HSC6Fc	ω-Functionalized ferrocene hexanethiol
Hz	Hertz
h	Hour
I	Intercept
IR	Infrared
i	Current
i_{LIM}	Limiting current
i.e.	That is
J	Joule
K	Degrees Kelvin
k	Kilo-
k_B	Boltzmann constant
kD	Kilodaltons
LUMO	Lowest unoccupied molecular orbital
log	Logarithm
M	Metal

	Molar
MeOH	Methanol
MM	Molar Mass
μM	Micromolar
MHz	MegaHertz
m	Meter
	Milli-
mg	Milligram
min	Minute
mL	Milliliter
mM	Millimolar
mol	Mole
mV	Millivolt
N	Newtons
	Nitrogen
N_2	Nitrogen gas
N_A	Avogadro's number
$NaBH_4$	Sodium borohydride
NaCl	Sodium chloride
NMR	Nuclear magnetic resonance
NP	Nanoparticle
n	Number of electrons transferred
	order of harmonic

nA	NanoAmperes
nm	Nanometer
nmol	Nanomoles
nM	NanoMolar
O	Oxygen
$^{-}$OOC	Deprotonated carboxylic acid group
Oct_4NBr	Tetraoctylammonium bromide
Pt	Platinum
pH	$-\log [H^+]$
QDL	Quantized double-layer
RS	Alkanethiolate
RSH	Alkanethiol
r	Radius
rpm	Rotations per minute
S	Sulfur
S/N	Signal-to-noise ratio
SAM	Self-assembled monolayer
SC6	Hexanethiolate
SC6Fc	ω-Functionalized ferrocene hexanethiolate
SCE	Saturated Calomel Electrode
SP	Surface plasmon

STM	Scanning tunneling microscopy
s	Second
T	Temperature
TEM	Transmission electron microscopy
TGA	Thermogravimetric analysis
THF	Tetrahydrofuran
UV-vis	Ultraviolet-visible
V	Volt
v	Volume
vs	Versus
X	Times
XPS	X-ray photoelectron spectroscopy
z	Charge state
β	Beta
δ	Chemical shift
ε	Dielectric constant
	Molar absorbance coefficient
ε_0	Permittivity of free space
ϕ	quantum efficiency
η	Viscosity
λ	Wavelength
μ	Micro-
	Shear modulus

ν	Scan rate
π	Pi
ω	Omega functional group
ρ	Density
	Packing density
=	Equals to
	Double bond
+	Positive
–	Negative
—	Single bond
<	Less than
>	More than
×	Multiplied by

Chapter One

Introduction to Gold and Silica Nanoparticles

1.1 Introduction

A limited global supply of fossil fuel sources coupled with increasing demand for energy prompted the recent establishment of Energy Frontier Research Centers[1] throughout the United States and highlights the need for basic and applied sciences pointing to new ways for generating, transmitting and storing alternative forms of energy. Localized production of energy, through the use of photovoltaics, solar concentrators and wind turbines is driving a need to change the way people think about energy storage since these production environments are subject to the day/night cycles and weather changes. Even basic transportation is likely to change over the several decades as usage of hybrids, plug-in hybrids, and fully-electric vehicles increases. Controlling, understanding and optimizing the science at the molecular (i.e. nanometer) level will be crucial if the vision for cleaner and more sustainable energy utilization is to be realized.

The ability to produce and store energy (charge) locally using such devices as fuel cells, batteries, and supercapacitors is an important step if these technologies are to be implemented on a large scale. Examination of a Ragone plot[2] (Figure 1.1) shows the tradeoff between power densities and energy densities for fuel cells, batteries, supercapacitors and conventional capacitors. This plot also shows the typical discharge rates for each of these devices. As the discharge rate of a device increases, so does its energy density but at the cost

Figure 1.1. Ragone Plot showing characteristics of energy storage and conversion devices. (Adapted from ref 2.)

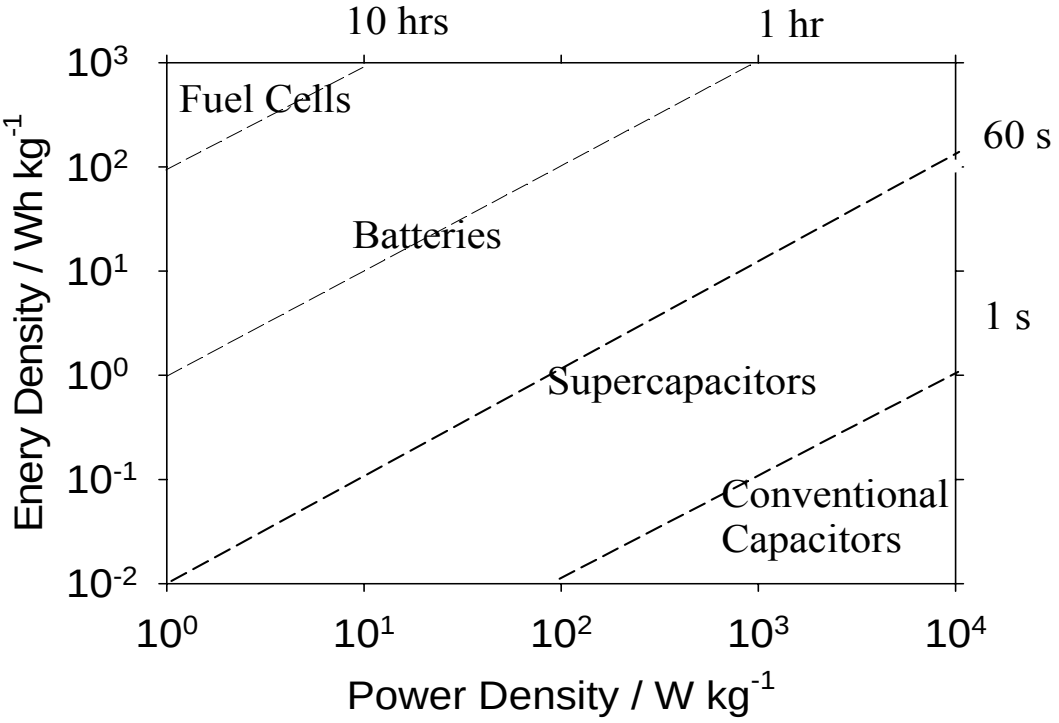
10 hrs
1 hr
Fuel Cells
60 s
Batteries
1 s
Supercapacitors
Conventional
Capacitors
Enery Density / Wh kg-1
Power Density / W kg-1
10^3
10^2
10^1
10^0
10^-1
10^-2
10^0
10^1
10^2
10^3
10^4

of power density. Construction of power supplies based on these devices is likely to take place in a complementary manner. For example, fully-electric vehicles containing a battery stack will likely be supported by supercapacitors during periods of increase energy demand such as merging on to a highway or starting out from a stoplight.

Supercapacitors, which fill the performance gap between the high power densities of conventional capacitors and high energy densities of batteries, are sometimes based on "pseudocapacitance," a combination of capacitance due to double-layer charging and a capacitance due to fast, highly-reversible, faradaic processes. These supercapacitors are differentiated from batteries by having sloping discharge curves, more rapid charge-discharge cycles and longevity to be cycled hundreds or thousands of times.[3] Already, supercapacitors are seeing use in power backup systems, mass-transit, wireless communication, personal electronics, power quality, and improved energy efficiency via regenerative energy capture devices.[3] Redox-active and redox-functionalized nanoparticles are ideally suited for examination as supercapacitors due to their high charge density and the ease with which they can be synthesized and characterized. These nanoparticles would ideally contain a large number of redox units per nanoparticle, giving rise to high charge density, that are all readily accessible and reversible.

Au Nanoparticles

The advent of the Brust Method,[4] was a major step forward in the synthesis of very small, thiol-protected gold nanoparticles (AuNPs) and has helped lead to an ever increasing amount of research regarding their synthesis, characterization and application in a variety of

contexts.[5-8] The two phase Brust synthesis (water-toluene) consists of the creation of an Au(I)-thiolate polymer that is subsequently reduced as shown below

$$AuCl_4^- \text{ (toluene)} + HSR \rightarrow (\text{Au(I)-thiolate-})_n \qquad (1)$$

$$(\text{Au(I)-thiolate-})_n + NaBH_4 \rightarrow Au_x(SR)_y \qquad (2)$$

The feed ratio of HSR to $AuCl_4^-$, the speed at which reducing agent is added, and temperature of the reaction are primary factors controlling the main distribution of AuNP sizes; smaller feed ratios of HSR to $AuCl_4^-$, slower reductant addition and warmer temperatures produce larger particles. Relatively monodisperse size distributions can be obtained through a series of solvent fractionations. More recent advances using modified Brust methods by our lab[9], and others[10] have shown that very monodisperse particle size distributions can be obtained for certain sizes.

Recent X-ray crystallography results[11-13] have shown that the smaller AuNPs (< 102 Au atoms) produced consist of an icosahedron core with "staples" or semi-rings covalently attached, consisting of (-thiolate-Au-thiolate-Au-thiolate-) chains. Theoretical[14] and mass spectrometry results[15] have shown that somewhat larger particles (≥ 102 Au atoms) also contain these "staples" extending from the core. Interestingly, the staples or semi-rings on the larger particles are not only (-thiolate-Au-thiolate-Au-thiolate-) but also (-thiolate-Au-thiolate).

Though X-ray crystallographic data provide absolute determination of the overall structure of an AuNP, producing crystals is a time-consuming and difficult process and for thiolated AuNPs has produced only three determinations.[11-13] Therefore, the analytical chemist must use a combination of techniques for alternative characterization. Transmission

electron microscopy (TEM) has proven useful for approximating the number of gold atoms in the nanoparticle. Thermogravimetric analysis (TGA) has been shown to be useful to measure (relative to the estimated Au atom counts) the number of thiolates on the nanparticles. Mixed monolayer compositions are typically determined using NMR by examining the responses of the incoming ligand to the ligand used in orginal synthesis. In addition, various spectroscopic techniques have been used to investigate monolayer packing or band gap determinations.

As-produced AuNPs are generally stable in air, resistant to aggregation, and can be dried and redissolved without loss in functionality. The larger particles, with core diameters between 1.6 and 2.0 nm exhibit[16,17] quantized double-layer charging in voltammetric experiments, much like coulomb blockade voltammetry exhibited by gold substrates in scanning electrochemical microscopy, due to the extremely low capacitance (< 6 aF) values of the nanoparticles. Smaller particles exhibit HOMO-LUMO gaps and show fine features in the UV-visible region.[18-20]

The main focus of this introduction will be the background of work on the functionalization of AuNPs with redox-active moieties. Functionalization can take place during the AuNP synthesis or by ligand exchange, post-nanoparticle synthesis. Hostetler et al. were the first to add the redox-active molecule ferrocene (Fc), in the form of $Fc(CH_2)_8SH$, to the surface of an AuNP.[21] These mixed-monolayer AuNPs were noted to adsorb to an electrode surface during cyclic voltammetry experiments. Unlike studies which will be discussed later, the adsorption was weak; rinsing with CH_2Cl_2 removed 95% of the adsorbed AuNPs. More robust adsorption occurred through the use of a dithiol linker between the electrode and the AuNPs.

Ingram and Murray synthesized $HS(CH_2)_3SAQ$ (SAQ = 1-(1,3-dithiapropyl)anthracene-9,10-dithione) functionalized AuNPs containing 25 redox active units.[22] These anthraquinone units were all reactive in successive one electron transfers for the radical anion but not for the radical dianion. Cyclic voltammetry experiments indicated that some adsorption was present but the electrochemistry was dominated by the freely diffusing particles.

Ingram et al. synthesized redox functionalized AuNPs through ligand exchange using $Fc(CH_2)_8SH$ and $HS(CH_2)_3SAQ$.[23] Up to 22% of the ligands on the original AuNPs were exchanged with the redox active thiols. Pietron and Murray took advantage of the AuNPs functionalized with the $HS(CH_2)_3SAQ$, mentioned above, to perform redox-mediated electrocatalysis.[24] These nanoparticles, which contained on average 18 redox-active units, mediated the one electron reduction of 1,1-dinitrocyclohexane at higher catalytic efficiency than the anthraquinone monomer. There were no indications of AuNP adsorption in those studies.

Green et al. synthesized redox-labeled AuNPs by exchanging $Fc(CH_2)_8SH$ onto alkylthiolate stabilized nanoparticles.[25] The obtained nanoparticles contained ca. 15 Fc per nanoparticle and would adsorb to an electrode surface when the potential of the electrode was cycled through the Fc/Fc^+ couple. Monolayer coverages were obtained, but as discussed, the poly-hetero-functionalized nanoparticles synthesized by Ingram et al.[23] were reversibly adsorbed, meaning that the nanoparticle film could be washed away with CH_2Cl_2. Chen[26] prepared Langmuir-Blodgett films of redox-labeled AuNPs and examined their electronic and ionic conductances. Electronic conductivity decreased as films became thicker, Fc peak potential shifted anodically, and not all Fc was accessed during voltammetric experiments.

The aqueous electrolyte, KNO_3, assured that the hydrophobic nanoparticles did not become dislodged during the experiments.

Another example of redox functionalization of AuNPs was performed by Fujihara and Nakai.[27] The researchers functionalized the AuNPs with C_{60}-thiol through a simple ligand exchange reaction with alkylthiolate stabilized AuNPs. Overnight immersion in an AuNP solution resulted in a spontaneous adsorption on an electrode surface. These films exhibited two reversible, one electron transfers when immersed in an electrolyte solution.

Miles and Murray[28] prepared phenothiazine functionalized AuNPs and showed that the phenothiazine units all reacted in rapid, successive, one-electron reactions. Adsorption was observed, but the particles were only weakly bound and desorbed from the electrode upon immersion in a nanoparticle-free electrolyte solution. Templeton et al.[29] studied viologen-labeled AuNP adsorption by electrochemical quartz crystal microbalance (EQCM) and were able to show that equivalents of monolayer coverages were possible. The strong adsorption was ascribed to the interaction of viologen reduction products. The preceeding studies consistently suggested that the AuNPs, especially those involving ferrocene ligands, were adsorption-prone, but reversibly so.

Recently, Wolfe et al.[30] synthesized fully-ferrocenated AuNPs using a modified Brust synthesis. This was the first example of the direct synthesis of an AuNP containing a full monolayer of a redox-active species. Cyclic voltammetry investigations showed that these particles strongly adsorbed to any electrode surface, up to monolayer coverages, when the potential of the electrode was cycled through the Fc/Fc^+ couple (which was typically done 25 times). The adsorbed layer of AuNPs could be transferred to fresh electrolyte solutions and

the ferrocene voltammetry stably observed, so the adsorption was nearly irreversible. The strong adsorption was proposed to involve entropically enhanced (multiple) ion-pairs between oxidized (ferrocenium) sites and adsorbed anions. These results can be analogously compared to the strong adsorption of polyelectrolyte films produced by Decher.[31]

The above discovery prompted further study to ascertain and obtain an understanding of the strong surface effect. Such investigations have found the adsorption to be anion dependent,[32] lending more credence to the hypothesis that the stably adherent films are a result of the multiple ion-pairs formed between ferrocenium sites and adsorbed anions. Sardar et al.[33] recently showed that the addition of a sulfonate or carboxylate self-assembled monolayer to the electrode surface resulted in the adsorption of fully-ferrocenated AuNPs at monolayer coverages. Unlike the studies by Wolfe et al.[30] and Stiles et al.[32] where 25 CV cycles resulted in coverages up to a monolayer, one complete CV cycle of the SAM-modified electrode resulted in monolayer coverages.

Expanding upon the idea that multiple ion-pair formation drives film formation and previous work by others[34-37] involving highly ionic nanoparticles, Chapters Two and Three of this thesis examine stably adherent, redox-labeled, highly ionic AuNP films. Utilization of AuNPs as supercapacitors will require controllable film formation and a thorough understanding of the interfacial flux of charge compensating ions through the film/solution interface.

SiO_2 Nanoparticles

Labelled silica nanoparticles (SiNP) have been an object of investigation for some time and have for example been used as imaging agents, in coatings applications, for sensing,[38-40]

catalytic activities[41] and drug delivery[42,43]. SiNPs are also being used to slow corrosion on aluminum current collectors[44] through their incorporation into gel electrolytes. Other gel electrolytes based on lithium modified SiNPs have been prepared.[45] Here, the Li^+ is complexed with a sulfonate group that is covalently attached to the SiNP.

The Stöber Method[46] is a convenient way to synthesize SiO_2 particles with diameters ranging from ca. 10 nm to > 1000 nm, depending on reaction conditions. These nonporous, relatively monodisperse, polar solvent-soluble particles are stable against aggregation, and are easy to manipulate and functionalize. The gel-like matrix derived from the synthesis makes it amenable to functionalization during synthesis, either simply by adding the species of interest into the reaction (e.g. Fc) or by adding a functionalized silane (e.g., here, $(MeO)_3Si(CH_2)_3NHCOFc$) which is then permanently incorporated into the matrix. Synthesis of the latter is slightly complicated by the addition of the functionalized silane, making particle size control more difficult along with accessibility of the functionalized silane questionable. Confirmation and quantitation of these functionalized nanoparticles can be accomplished using a variety of techniques. Solid-state NMR (SS-NMR) is an extremely useful tool that allows examination of changes to the surface of the nanoparticle (e.g. consumption of residual silanols). FTIR allows confirmation of functional groups along with changes in the nanoparticle surface. X-ray photoelectron spectroscopy (XPS) allows the confirmation and approximate quantitation of a species of interest. Finally, a variety of electrochemistry techniques allow examination and quantitation of redox active species.

There are several reports regarding functionalization of SiO_2 with redox active species. Budny et al.[41] covalently bound Fc, a Ru complex and an aniline derivative to nanoparticles ranging in size from 140 to 750 nm. These particles spontaneously adsorbed to an electrode

surface when the electrode was immersed in a stirred SiNP solution; the adsorption was possibility due to residual silanols residing on the surface of the particle. Cyclic voltammetry, used to quantify the number of electroactive sites, were compared with AAS and ICP-MS results and showed that only a small fraction of the total number of sites are electroactive.

Ling et al.[47] prepared 60 nm diameter ferrocenyl-functionalized SiNPs for examining guest-host interactions. Though these particles were smaller, the ferrocene coverage was low and the particles exhibited mixed adsorption-diffusion behavior during electrochemical studies. Plumeré and Speiser[48] synthesized ferrocenyl-functionalized SiNP through hydrosilation. These 200 nm diameter particles spontaneously adsorbed on Pt. Like those studies mentioned above, not all Fc were accessible to electrochemical reaction. In our view, design of systems utilizing redox-active SiNPs requires use of smaller particles such that the rotational diffusion time constant is smaller than the residence time of the nanoparticle near the electrode. This will allow for full reactivity during typical experimental timescales. We therefore focused on very small SiNPs, both for full electrochemical reactivity and for a large volume capacity of electrochemical charge.

Chapter Four of this dissertation will discuss the voltammetry and redox storage capability of ferrocenated SiNPs. These particles are the first example of freely diffusing, fully-ferrocenated SiNPs that show no significant adsorption and full ferrocene reactivity. These results, combined with those results discussed in Chapters Two and Three provide an improved foundation for fabrication of supercapacitors based upon redox-active nanoparticles.

1.2 References

1. *Energy Frontier Research Centers: Tackling our Energy Challenges in a New Era of Science;* Office of Science, U.S. Department of Energy, 1000 Independence Ave., SW
   Washington, DC, **2009**.

2. Rolison, D. R.; Long, J. W.; Lytle, J. C.; Fischer, A. E.; Rhodes, C. P.; McEvoy, T. M.; Bourg, M. E.; Lubers, A. M. *Chem. Soc. Rev.* **2009,** *38,* 226-252.

3. Miller, J. R.; Burke, A. F. *Interface* **2008,** *17,* 53-57.

4. Brust, M.; Walker, M.; Bethell, D.; Schriffrin, D. J.; Whyman, R. *J. Chem. Soc., Chem. Commun.* **1994**, 801 – 802.

5. Templeton, A. C.; Wuelfing, W. P.; Murray, R. W. *Acc. Chem. Res.* **2000,** *33,* 27-36.

6. Sardar, R.; Funston, A. M.; Mulvaney, P.; Murray, R. W. *Langmuir* **2009,** *25,* 13840-13851.

7. Murray, R. W. *Chem. Rev.* **2008,** *108,* 2688-2720.

8. Parker, J. F.; Fields-Zinna, C. A.; Murray, R. W. *Acc. Chem. Res.* ASAP.

9. Parker, J. F. Ph.D., University of North Carolina at Chapel Hill, 2010.

10. Huifeng, Q.; Jin, R. *Nano Lett.* **2009,** *9,* 4083-4087.

11. Heaven, M. W.; Dass, A.; White, P. S.; Holt, K. M.; Murray, R. W. *J. Am. Chem. Soc.* **2008,** *130,* 3754-3755.

12. Jadzinsky, P. D.; Calero, G.; Ackerson, C. J.; Bushnell, D. A.; Kornberg, R. A. *Science* **2007,** *318,* 430-433.

13. Zhu, M.; Eckenhoff, W. T.; Pintauer, T.; Rongchao, J. *J. Phys. Chem. B* **2008,** *112,* 14221-14224.

14. Akola, J.; Walter, M.; Whetten, R. L.; Häkkinen, H.; Grönbeck, H. *J. Am. Chem. Soc.* **2008,** *130,* 3756-3757.

15. Fields-Zinna, C. A.; Sampson, J. S.; Crowe, M. C.; Tracy, J. B.; Parker, J. F.; deNey, A. M.; Muddiman, D. C.; Murray, R. W. *J. Am. Chem. Soc.* **2009,** *131,* 13844-13851.

16. Hicks, J. F.; Miles, D. T.; Murray, R. W. *J. Am. Chem. Soc.* **2002,** *124,* 13322-13328.

17. Wolfe, R. L.; Murray, R. W. *Anal. Chem.* **2006,** *78,* 1167-1173.

18. Donkers, R. L.; Lee, D.; Murray, R. W. *Langmuir* **2004,** *20,* 1945-1952.

19. Lee, D.; Donkers, R. L.; Wang, G.; Harper, A. S.; Murray, R. W. *J. Am. Chem. Soc.* **2004,** *126,* 6193-6199.

20. Yang, Y.; Chen, S. *Nano Lett.* **2003,** *3,* 75-59.

21. Hostetler, M. J.; Green, S. J.; Stokes, J. J.; Murray, R. W. *J. Am. Chem. Soc.* **1996,** *118,* 4212-4213.

22. Ingram, R. S.; Murray, R. W. *Langmuir* **1998,** *14,* 4115-4121.

23. Ingram, R. S.; Hostetler, M. J.; Murray, R. W. *J. Am. Chem. Soc.* **1997,** *119,* 9175-9178.

24. Pietron, J. J.; Murray, R. W. *J. Phys. Chem. B* **1999,** *103,* 4440-4446.

25. Green, S. J.; Pietron, J. J.; Stokes, J. J.; Hostetler, M. J.; Vu, H.; Wuelfing, W. P.; Murray, R. W. *Langmuir* **1998,** *14,* 5612-5619.

26. Chen, S. *Langmuir* **2001,** *17, 6664-6668.*

27. Fujihara, H.; Nakai, H. *Langmuir* **2001,** *17,* 6393-6395.

28. Miles, D. T.; Murray, R. W. *Anal. Chem.* **2001,** *73,* 921-929.

29. Tempelton, A. C.; Cliffel, D. E.; Murray, R. W. *J. Am. Chem. Soc.* **1999,** *121,* 7081-7089.

30. Wolfe, R. L. Balasubramanian, R.; Tracy J. B.; Murray, R. W. *Langmuir* **2007,** *23,* 2247-2254.

31. Decher, G. *Science* **1997,** *277,* 1232-1237.

32. Stiles, R. L.; Balasubramanian, R.; Feldberg, S. W.; Murray, R. W. *J. Am. Chem. Soc.* **2008,** *130,* 1856-1865.

33. Sardar, R. Beasley, C. A.; Murray, R. W. *Anal. Chem.* **2009,** *81,* 6960-6965.

34. Luo, J.; Kariuki, N.; Han, L.; Maye, M. M.; Moussa, L. W.; Kowalski, S. R.; Kirk, F. L.; Hepel, M.; Zhong, C.-J. *J. Phys. Chem. B* **2002,** *106,* 9313-9321.

35. Nair, A. S.; Kimura, K. *J. Chem. Phys.* **2008,** *129,* 184117.

36. Nair, A. S.; Kimura, K. *Langmuir* **2009,** *25,* 1750-1756.

37. Sardar, R. Beasley, C. A.; Murray, R. W. *J. Am. Chem. Soc.* **2010,** *132,* 2058-2063.

38. Wang, J.; Liu, G.; Lin, Y. *Small* **2006,** *2,* 1134-1138.

39. Guo, Z.; Shen, Y.; Wang, M.; Zhao, F.; Dong, S. *Anal. Chem.* **2004,** *76,* 184-191.

40. Zhang, F.-F.; Wan, Q.; Wang, X.-L.; Sun, Z.-D.; Zhu, Z.-Q.; Xian, Y.-Z.; Jin, L.-T.; Yamamoto, K. *J. Electroanal. Chem.* **2004,** *571,* 133-138.

41. Budny, A.; Novak, F.; Plumeré, N. Schetter, B.; Speiser, B.; Straub, D.; Mayer, H. A.; Reginek, M. *Langmuir* **2006,** *22,* 10605-10611.

42. Slowing, I. I.; Trewyn, B. G.; Lin, V. S.-Y. *J. Am. Chem. Soc.* **2007,** *129,* 8845-8849.

43. Slowing, I. I.; Trewyn, B. G.; Giri, S.; Lin, V. S.-Y. *Adv. Funct. Mater.* **2007,** *17,* 1225-1236.

44. Li, Y.; Fedkiw, P. S. *Electrochim. Acta* **2007,** *52,* 2471-2477.

45. Sun, J.; Bayley, P.; MacFarlane, D. R.; Forsyth, M. *Electrochim. Acta* **2007,** *52,* 7083-7090.

46. Stöber, W.; Fink, A.; Bohn, E. *J. Colloid Interface Sci.* **1968,** *26,* 62-69.

47. Ling, X. Y.; Reinhoudt, D. N.; Huskens, J. *Langmuir* **2006,** *22,* 8777-8783.

48. Plumeré, N.; Speiser, B. *Electrochim. Acta* **2007,** *53,* 1244-1251.

Chapter Two

Entropically Driven Poly-Cationic Au NP Adsorption on an Electrode Surface

2.1 Introduction

Our group has previously reported on the irreversible adsorption of fully-ferrocenated Au nanoparticles (AuFcNPs) on bare or self-assembled monolayer (SAM) modified electrode surfaces.[1-3] The driving force of strong adsorption was due to multiple ion-pair formation between adsorbed anions on the electrode surface and ferrocenium ions present on the nanoparticle (NP), as well as multiple ion-pair bridging interactions between NPs. In this chapter, we investigate the adsorption in more detail. The adsorption process was followed for a mixed monolayer NP where permanent positive charge [$-N^{+}(CH_2CH_3)_3$] was introduced on the nanoparticle surface, Au_{225}(TEA-thiolate)$_{22}$(SC6Fc)$_9$. The mixed monolayer NP contained a few ferrocene groups as an internal reference for the determination of nanoparticle coverage on the electrode surface (Γ_{NP}). The main points of this chapter are (i) incorporation of permanent positive charge influences the surface coverage, (ii) the effects of various electrolytes on the Γ_{NP}, and (iii) support for our original hypothesis that entropically favored ion-pairing drives film formation.

The important aspects of gold nanoparticles have been the breadth of their impact for molecular detection system,[4-5] in device fabrication,[6,7] and for electronic sensor applications[8,9]. Voltammetry of thiolated AuNPs has been studied extensively due to their interesting electrochemical behavior,[10] including bulk-continuum voltammetry, quantized double layer charging voltammetry, and molecule-like voltammetry.[11-18] These near-

molecular species display interesting multi-electron reactivities upon functionalization with various redox groups.[10,19-24] The chemistry of interactions of protected Au nanoparticles with electrode surfaces is still an expanding topic. A variety of attachment chemistries has been described, using both covalent and ionic interactions.[25-30]

Films based on metal nanoparticles as building blocks on planar substrates have attracted substantial interest due to their unique optical, or electrical properties[26,31,32] and high thermal, or chemical stability[33]. Moreover, applications using these hybrid films in chemiresistors or biological sensing have been reported by various groups.[10,34-38] Films on solid supports, have been prepared using various techniques and one of the most standard procedures is layer-by-layer (LBL) deposition.[26,32,38-41] In this method, multiple electrostatic ionic interactions between functionalized nanoparticles and polyelectrolytes promote the formation of films. The method mostly relies on a simple dipping protocol between functionalized NPs and polyelectrolyte solutions. Multilayer films have also been prepared based on ligand/metal ion/ligand linkers as reported earlier.[25,27]

Herein, we describe irreversible NP film formation on an electrode surface via an electrochemical method. Three different MPC compositions, Au_{225}(TEA-thiolate)$_X$(SC6Fc)$_Y$ (X=18, Y=13; X= 22, Y= 9; X= 27, Y= 4) were used to show that coverages equivalent to 2-4 NP layers are formed. This is the first example where multilayer NP films form on an electrode surface during potential scanning in an electrochemical experiment. The full-width-half-maximum ($E_{fwhm,OX}$) of the oxidation peak (83, 89 or 130 mV) is considerably higher than the value reported previously and reasons for this will be explored.[2,3] Finally, as will be explained, the film formation is believed to be entropically driven process.

2.2 Experimental Section

Chemicals. 11-Bromo-1-undecene (>95%), triethylamine (NEt_3, >99%), thioacetic acid (>98%), t-Butylammonium borohydride (Bu_4NBH_4,>98%) *t*-octylammonium bromide (Oct_4NBr, >98%), sodium borohydride ($NaBH_4$, >98%), *t*-butylammonium perchlorate (Bu_4NClO_4, >99%), lithium perchlorate (LiClO4, >98%), *t*-butylammonium *p*-toluenesulfonate ($Bu_4NC_7H_7SO_3$, puress), and *t*-butylammonium hexafluorophosphate (Bu_4NPF_6, puress), *t*-ethylammonium perchlorate (Et_4NClO_4, >99%) from Aldrich and toluene (reagent grade), acetonitrile (Optima), methylene chloride (HPLC grade), tetrahydrofuran (HPLC grade), and ethanol (HPLC grade) from Fisher were used as received. $HAuCl_4$ *x*H2O (from 99.999% pure gold) was synthesized using a literature procedure (Brauer, G 1965) and stored in a freezer at -20 °C. Water was purified using a Barnstead NANOpure system (18 MΩ).

Synthesis of Ferrocene hexanethiol. Ferrocene hexanethiol (HSC6Fc) was synthesized as previously described.[3] ^{1}H NMR (400 MHz, CD_2Cl_2) of the thiol gave the appropriate NMR peaks: δ = 4.0 (Fc, s, 9 H), 2.49 (*CH_2*SH, q, 2H *J=7.2 Hz)*,, 2.30 (*CH_2*Fc, t, 2H, *J=7.6 Hz*), 1.56 (*CH_2*CH_2SH, m, 2 H), 1.46 (*CH_2*CH_2Fc, m, 2 H), and 1.32 (m, 4 H) ppm with no dithiol peaks (t, 4H, 2.66 ppm) present and no significant broadening, indicating that the majority of the ferrocenyl groups were in the reduced state .

Synthesis of *N, N, N*-triethyl(11-undecnylmercapto)ammonium chloride (TEA-thiolate). *N,N,N-Triethyl-10-undecnylammonium bromide*. The thiol was synthesized as previously reported literature.[42]

Synthesis of Quaternary-Ammonium Thiolate Functionalized NPs. The thiol-protected gold nanoparticles were synthesized as previously described.[43]

Synthesis of Mixed Monolayer NPs. Three different mixed monolayer NPs were prepared by ligand exchange between Au_{225}(TEA-thiolate)$_{31}$ and HSC6Fc at a 1:0.5, 1:1, or 1:2 mole ratio of ω-ferrocenyl hexanethiol to TEA-thiolate ligand for Au_{225}(TEA-thiolate)$_{27}Fc_4$, Au_{225}(TEA-thiolate)$_{22}Fc_9$, and Au_{225}(TEA-thiolate)$_{18}Fc_{13}$, respectively. A 50-mL ethanol solution of Au_{225}(TEA-thiolate)$_{31}$ and HSC6Fc was stirred for 4 hrs at room temperature. Then 0.102 g of $LiClO_4$ was added, resulting in the formation of solid, and the reaction mixture was stirred for 30 additional minutes. The solid then collected by filtering with a fine glass frit, followed by washing with ethanol. Extent of ligand exchange was determined by ^{1}H NMR.

Electrochemistry. Voltammetry of was typically done in 0.05 mM mM Au_{225}(TEA-thiolate)$_{22}$(SC6Fc)$_9$ CH_3CN solutions containing various concentrations of electrolyte. A 1.6 mm diameter Pt disc and a Pt wire were used as the working and counter electrodes, respectively. The roughness factor (2.8) of the working electrode was determined from the charge under the hydrogen desorption peak in voltammetry of 0.10 M H_2SO_4, using the standard 210 μC/cm^2.[44] A Ag/AgCl/ 3M KCl (aq) was used as the reference electrode. Measurements were performed using a CH Instruments (Austin, TX) model 760C electrochemical analyzer. In "*scanning*" experiments, the adsorption step was carried out by cyclically scanning the electrode in unstirred 0.05 mM Au_{225}(TEA-thiolate)$_{22}$(SC6Fc)$_9$ solutions in CH_3CN containing various concentrations (1.0, 0.1, and 0.01 M) of Bu_4NClO_4, between the potential limits of -0.1 to 1.0 V vs Ag/AgCl (aq) for one time. The electrode was then rinsed and transferred to fresh electrolyte of a particular concentration. Surface coverages, Γ_{NP} (mol NP/cm^2), of adsorbed NPs were calculated from the charge, q, under the ferrocene oxidation peak using

$$q = n A_m F \Gamma_{NP} \qquad (1)$$

where *n* is the average number of ferrocenes per nanoparticle, and A_m is the Pt working electrode area, corrected for roughness. The experimentally determined values of Γ_{NP} are compared to estimates of a model monolayer, of $\Gamma_{MONO,NP} = 5.2 \times 10^{-12}$ mol NP/cm^2 (assuming 32.2 nm^2/ Au_{225}(TEA-thiolate)$_{22}$(SC6Fc)$_9$, and based on an overall particle radius of ca. 3.2 nm).

In the current vs. time (i-t curve) experiments, a freshly polished Pt electrode was placed into 0.05 mM Au_{225}(TEA-thiolate)$_{22}$(SC6Fc)$_9$ in 1.0 M Bu_4NClO_4/CH_3CN and applied -0.1 V potential vs. Ag/AgCl (aq) for 5 minutes. The electrode was then rinsed with CH_3CN and immersed in *NP-free* 1.0 M Bu_4NClO_4/CH_3CN, and Γ_{NP} was determined by scanning between -0.1 to 1.0 V vs. Ag/AgCl (aq) potential window at 0.5 V/s for one cycle. The electrode was then repolished and returned to the another set of 0.05 mM Au_{225}(TEA-thiolate)$_{22}$(SC6Fc)$_9$ in 1.0 M Bu_4NClO_4/CH_3CN solution for different applied potential such as -0.2, -0.4, -0.5, -0.75, and -1.0 V vs. Ag/AgCl (aq).

In an isotherm experimental protocol (*no-scan survey*), a clean Pt disk electrode was exposed at open circuit to an unstirred solution of 0.025 mM Au_{225}(TEA-thiolate)$_{22}$(SC6Fc)$_9$ in 0.1 M Bu_4NClO_4/CH_3CN for 15 minutes. The electrode was rinsed with CH_3CN and immersed in *NP-free* 0.1 M Bu_4NClO_4/CH_3CN, and Γ_{NP} was determined by scanning between -0.1 to 1.0 V vs. Ag/AgCl (aq) potential window at 0.5 V/s for one cycle. This process was then repeated for different MPC concentrations such as 0.04, 0.05, 0.075, 0.085, 0.1, 0.15, and 0.2 mM.

In the electrolyte effects experiments (*survey experiment*) a freshly polished Pt electrode was placed in unstirred 0.05 mM of Au_{225}(TEA-thiolate)$_{22}$(SC6Fc)$_9$ in CH_3CN solutions

contained 1.0 M of $Bu_4N^+X^-$ electrolyte ($X^- = PF_6^-$, or *p*-toluene sulfonate$^-$) and scanned for one full cycle between the potential limits of -0.1 to 1.0 V vs Ag/AgCl (aq). The electrode was then electrode the rinsed with CH_3CN and transferred to *NP-free* 1.0 M electrolyte/CH_3CN solution for coverage determination. A similar procedure was followed for other electrolytes having different cations, $Y^+ClO_4^-$ ($Y^+ = Li^+$, Et_4N^+, or Bu_4N^+).

2.3 Results and Discussion

Study of the Adsorption of Au_{225}(TEA-thiolate)$_{22}$(SC6Fc)$_9$ in CH_3CN. Au_{225}(TEA-thiolate)$_{22}$(SC6Fc)$_9$ was adsorbed to an electrode from a 0.05 mM solution containing 1.0 M Bu_4NClO_4/CH_3CN. After scanning the electrode between the potential limits of -0.1 to 1.0 V vs. Ag/AgCl(aq), the electrode was rinsed with CH_3CN and transferred to *NP-free* 1.0 M Bu_4NClO_4/CH_3CN solution and scanned over the same potential range to determine the coverage, Γ_{NP} (mol/cm^2). Figure 2.1 represents the cyclic voltammogram of the adsorbed film. Coverage was determined to be 9.3 X 10^{-12} mol/cm^2. This coverage is almost 9-fold higher than the previous report, where the electrode was not modified with a SAM[2] and 3-fold higher than in the case of SAM modified electrode[3]. A similar experimental protocol was followed to determine the adsorption of Au_{225}(TEA-thiolate)$_{22}$(SC6Fc)$_9$ from 0.1 and 0.01 M Bu_4NClO_4/CH_3CN and transferred to *NP-free* 0.1, or 0.01 M Bu_4NClO_4/CH_3CN solutions, see Figure 2.1 and Table 2.1. The coverage, Γ_{NP}, for 0.1 and 0.01 M Bu_4NClO_4/CH_3CN are 8.7 and 7.5 X 10^{-12} mol/cm^2 respectively. These coverages are also higher in value in comparison to our previous studies.[2,3] In both those two previous reports, we mentioned that the adsorption was irreversible and promoted by multiple ion-pair formations between oxidized ferrocenes (ferrocenium) and electrolyte anions. We also

showed that ionic interactions between carboxylate ions in a SAM and ferrocenium did play a major role in producing a stably adherent film.[3] Those results suggested that, the oxidized form of ferrocene was almost essential to take part in previously mentioned ionic interactions. In this present study, the mixed monolayer NP contains 22 permanent positive charges in the form of a quaternary ammonium salt-terminated thiol, [$-N^{+}(CH_2CH_3)_3$]. The positive charges help to form multiple, simultaneous, different ion-pair formations between nanoparticles using electrolyte anions. The Γ_{NP} in these instances varies with electrolyte concentration but it effects is much less prominent than the previous studies. In the present study we have found coverages equivalent to ca. two monolayers are formed on the electrode surface for 0.01, 0.1 or 1.0 M Bu_4NClO_4/CH_3CN. This multilayer film formation indicates that multiple interactions between adsorbed anions and NP on the electrode surface are present. Additionally, there are numerous lateral interactions, which are mostly directed by the positive charge on particle surface. Now the question arises, while we have observed an electrolyte concentration effect on surface coverage previously,[2,3] we have not observed one in the present study. In this present scenario, Au_{225}(TEA-thiolate)$_{22}$(SC6Fc)$_9$ has perchlorate (ClO_4^-) counter anions and as a result the amount of electrolyte present during the potential scanning did not influence the film formation as much. The ClO_4^- attached to the NP takes part in multiple bridging-ion pair interactions.

The cyclic voltammetric peak shape has provided us an informative account regarding the ferrocenium/X-/ferrocenium interaction. Previously it was found that the oxidation peak of ferrocene for fully-ferrocenated NPs[2,3] is very sharp and the full width half maximum (E_{fwhm}) was 35 mV. The results suggested there were multiple ferrocenium/X^-/ferrocenium lateral interactions.[45,46] In this present study $E_{fwhm,OX}$ values for Au_{225}(TEA-

Figure 2.1. Cyclic voltammetry of adsorbed Au_{225}(TEA-thiolate)$_{22}$(SC6Fc)$_9$ for different electrolyte concentrations (*NP-free*) in Bu_4NClO_4/CH_3CN with potential scan rate of 0.5 V/s. The NP film was prepared in 0.05 mM Au_{225}(TEA-thiolate)$_{22}$(SC6Fc)$_9$ in either 1.0 (black curve), 0.1 (red curve), or 0.01 (blue curve) M Bu_4NClO_4/CH_3CN with potential scan rate 0.5 V/s. The film was transferred to *NP-free* solution containing the same concentration of Bu_4NClO_4/CH_3CN.

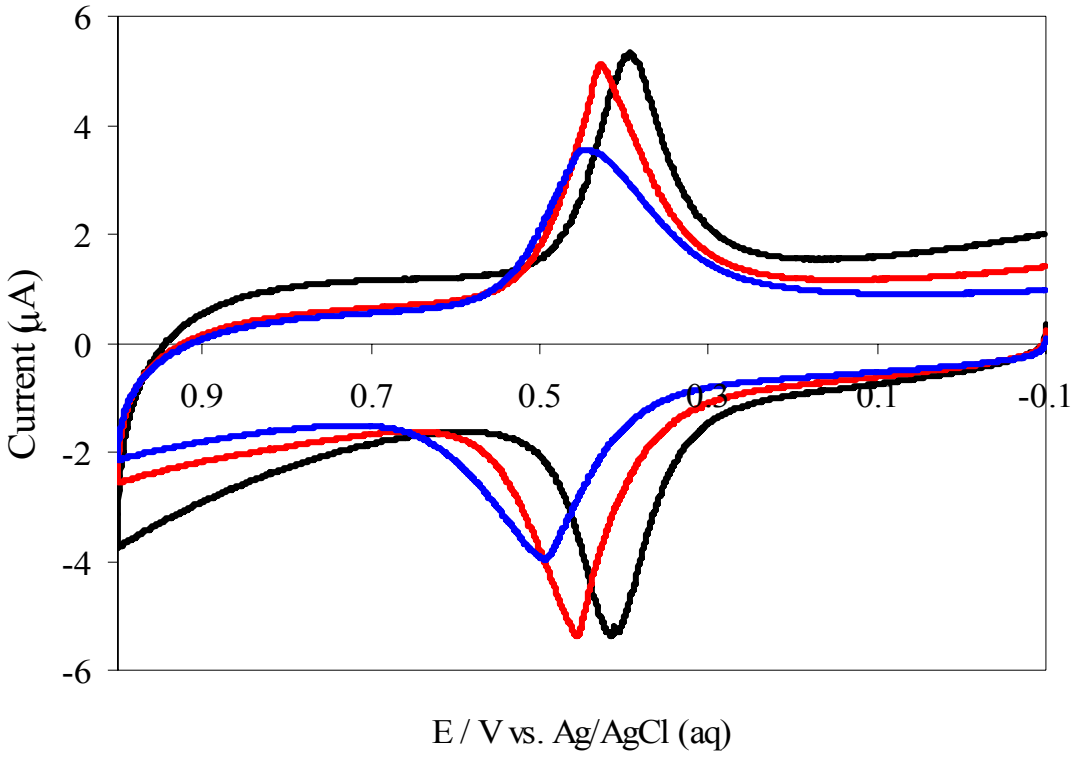
6
4
2
0
-2
-4
-6
Current (μA)
0.9
0.7
0.5
0.3
0.1
-0.1
E / V vs. Ag/AgCl (aq)

Table 2.1. Effect of Concentration of Supporting Electrolyte on Surface Coverage of Au_{225}(TEA-thiolate)$_{22}$(SC6Fc)$_9$ Adsorbed on a Pt Electrode from a 0.05 mM NP solution/CH_3CN. The Electrode was then Rinsed and Transferred to *NP-free* Electrolyte Solution at the Same Concentration.[a,b]

Supporting Electrolyte	[Supporting Electrolyte]	Γ_{NP} (x 10^{-12} mol / cm^2)
Bu_4NClO_4	1.0	9.3
	0.1	8.7
	0.01	7.5

[a]The scan rate is 0.5 V/s. [b]Scan between -0.1 and 1.0 V vs. Ag/AgCl (aq).

thiolate)$_{18}$(SC_6Fc)$_{13}$, Au_{225}(TEA-thiolate)$_{22}$(SC_6Fc)$_9$ and Au_{225}(TEA-thiolate)$_{27}$(SC_6Fc)$_4$ are 83, 89, and 130 mV, respectively. The theoretical E_{fwhm} for a surface confined, non-interacting electroactive monolayer is 90.6 mV and is based on a linear relationship between surface coverage and activity.[44] Fully-ferrocenated NPs, give rise to a number of opportunities for lateral interactions because the particle surface is covered with ferrocene groups. Scanning was a requirement to produce a stably adherent film in this instance, indicating that the oxidation of ferrocene to produce ferrocenium was crucial, resulting in ferrocenium/X-/ferrocenium attractive interactions. This is why we saw E_{fwhm} values of 35 mV. Our new particles have ferrocene imbedded within the monolayer due to the longer TEA-thiolate chain, and therefore are harder to access, resulting in a reduced probability of inter-particle ferrocenium/X^-/ferrocenium interactions. Additionally, scanning is not a requirement (vida supra) with the present mixed monolayer NPs to produce stably adherent films, meaning interparticle ferrocenium/X-/ferrocenium attractive interactions are not necessary.

The formation of multilayer NP films could be analogous to multilayer polyelectrolyte films on solid supports.[47-51] In the case of the polyelectrolyte films, the removal of a large solvent and small counter ions gives an entropic gain, imparting stability of the film. The stability Au_{225}(TEA-thiolate)$_{22}$(SC6Fc)$_9$ films to repeated cycling was examined by cycling the potential of the electrode between -0.1 and 1.0 V vs. Ag/AgCl (aq) There was an approximate 2.8% loss of coverage between first and 25th scans. After 25 scans ca. two NP layers still remain on the electrode surface. These data suggest a large number of multi-directional lateral interactions are present between the NP and electrolyte anions. The data also imply that adsorption of first layer is very strong which holds the remaining layers on

top of it. This would be only possible if the first layer would interact very strongly with electrode surface. This strong interaction comes between the adsorbed electrolyte anions and quaternary ammonium ions from the NP.

The result we have discussed so far implies that the value of Γ_{NP} is mostly directed by vertical and lateral interactions between positively charged [$-N^{+}(CH_2CH_3)_3$] and electrolyte anions. In our previous reports,[2,3] we discussed that the vertical and lateral interactions were formed between ferroceniums and electrolyte anions. As there are large number of permanent positive charges are present in Au_{225}(TEA-thiolate)$_{22}$(SC6Fc)$_9$, the number of ferrocene groups should not influence greatly the surface coverage and stability of the films. To prove that fact, the electrode was scanned over a smaller window, -0.1 to 0.6 to -0.1 V vs. Ag/AgCl (aq), in a solution of 0.05 mM Au_{225}(TEA-thiolate)$_{22}$(SC6Fc)$_9$ in 1.0 M Bu_4NClO_4/CH_3CN, then rinsed and transferred to *NP-free* 1.0 M Bu_4NClO_4/CH_3CN and scanned over the same scale. The purpose of the experiment is to oxidize on a fraction of the ferrocene. In other words, if the ferrocene oxidation process does influence the lateral and vertical interactions, then Γ_{NP} would be less than the value we have obtained before for a larger potential scale window, -0.1 to 1.0 V ($\Gamma_{NP} = 9.3 \times 10^{-12}$ mol/cm^2). As we expected, the ferrocene oxidation did not influence the Γ_{NP} and is found to be 9.6×10^{-12} mol/cm^2.

Our group has previously reported on the NP adsorption on an electrode surface where either the NP was fully-ferrocenated[2] or partially-ferrocenated (10-15% of monolayer)[52,53]. In the case of fully-ferrocenated NPs, even though the coverage was less than the present case, the film was very robust and could only be removed by mechanical polishing. On the other hand, a less robust film was observed for the partially-ferrocenated NPs. In this present investigation, we have observed very high coverage of NP, $6.2\text{-}13.9 \times 10^{-12}$ mol/cm^2, which

is almost equal to 2-4 monolayers. Such a high coverage could be possible if there is enormous amount of lateral interactions present. This also implies, bridging ion-pair interaction is very strong, which helps irreversible NP adsorption. As the NP contains ClO_4^- as counter anions on its surface, the formation of bridging ion-pair would be entropically favorable process.

Adsorption Isotherm of Au_{225}(TEA-thiolate)$_{22}$(SC6Fc)$_9$. In a previous report, we showed that adsorption of fully-ferrocenated NPs did take place on the electrode surface without any potential scanning of electrode (*no-scan survey* experiment).[2] Lower surface coverage was achieved in comparison to an experiment where the electrode potential was scanned. We stated that the fully ferrocenated NPs could contain a small number of ferrocenium sites which influence the adsorption process via bridging ion-pair interactions. Besides the NP adsorption phenomenon, ferrocenated dendrimers are also known to adsorb without oxidation.[46] Since the present particles, Au_{225}(TEA-thiolate)$_{22}$(SC6Fc)$_9$, contain permanent positive charges, it would be interesting to see how coverage varied in a *no-scan survey* experiment using different NP concentrations. The typical experimental procedure was as follows: a clean Pt disk electrode was exposed at open circuit to unstirred solutions of Au_{225}(TEA-thiolate)$_{22}$(SC6Fc)$_9$ in 0.1 M Bu_4NClO_4/CH_3CN for 15 minutes. The electrode was then rinsed with CH_3CN and immersed in *NP-free* 0.1 M Bu_4NClO_4/CH_3CN, and Γ_{NP} was determined from the charge under the ferrocene oxidation peak by scanning between -0.1 to 1.0 V potential window at 0.5 V/s for one cycle. Depending on the NP concentration, the coverage varies from 6.9-13.8 X 10^{-12} mol/cm^2. The highest coverage was achieved when 0.1 mM NP was used. Figure 2.2 shows an isotherm for the NP coverage. Increasing the NP concentration above 0.1 mM did not cause an increase in coverage. From the graph, it is clear

Figure 2.2. MPC concentration dependent coverage of adsorbed film (*no-scan survey* experiment). Various concentrations, 0.025-0.20 mM, of $Au_{225}(TEA\text{-}thiolate)_{22}(SC6Fc)_9$ in 0.1 M Bu_4NClO_4/CH_3CN for 15 minutes. The electrode was rinsed with CH_3CN and immersed in *NP-free* 0.1 M Bu_4NClO_4/CH_3CN, and Γ_{NP} was determined by scanning between -0.1 to 1.0 V vs. Ag/AgCl (aq) potential window at 0.5 V/s for one cycle.

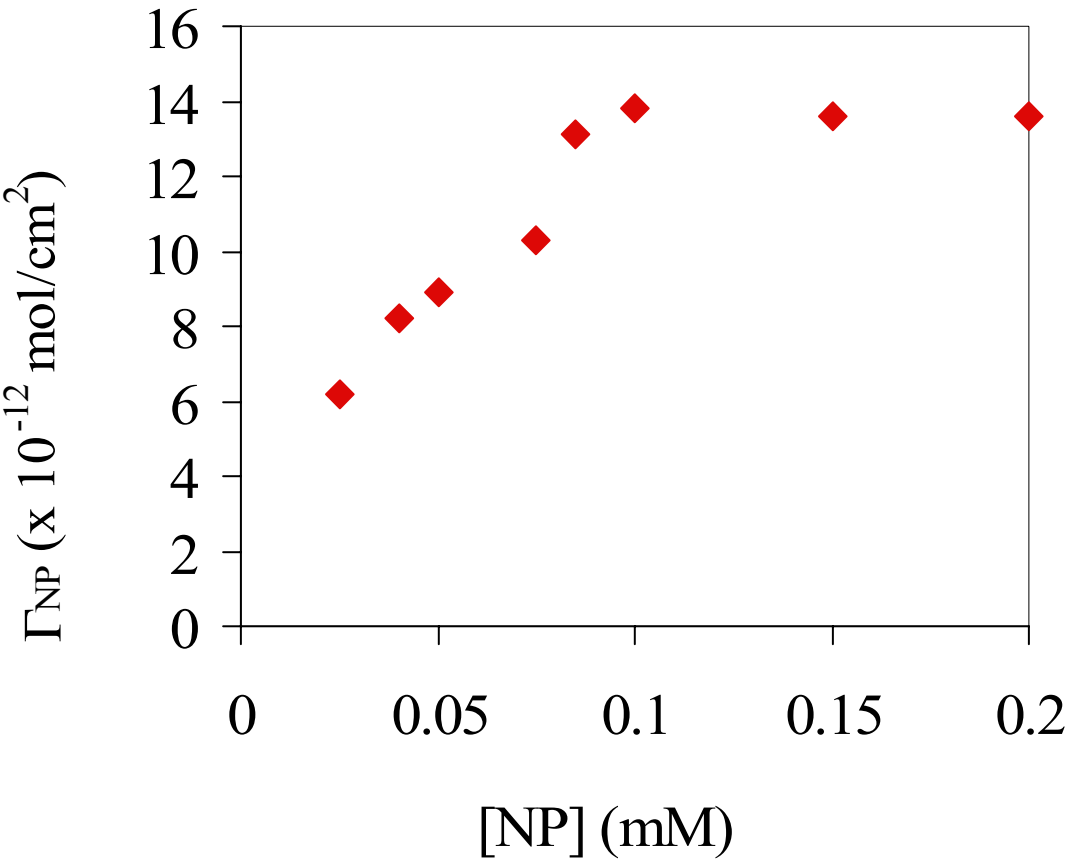
16
14
12
10
8
6
4
2
0
0
0.05
0.1
0.15
0.2
ΓNP (x 10-12 mol/cm2)
[NP] (mM)

that little more than a monolayer coverage (6.9 X 10^{-12} mol/cm^2) is achieved at a low NP concentration (0.025 mM) and multilayer coverage does occur at higher NP concentrations.

Effect on Film-Coverage of Initial Applied Potential. We have postulated that the adsorption of Au_{225}(TEA-thiolate)$_{22}$(SC6Fc)$_9$ is dependent upon vertical interactions between adsorbed electrolyte anions on electrode surface and -$N^+(CH_2CH_3)_3$, on the nanoparticle surface. Another way to examine this interaction is by applying different potentials to the electrode and examining the effect on coverage. Applying a more negative potential should cause a decrease in surface coverage due to decreased electrolyte anions present on the electrode surface. A freshly polished Pt electrode was placed in 0.05 mM Au_{225}(TEA-thiolate)$_{22}$(SC6Fc)$_9$ in 1.0 M Bu_4NClO_4/CH_3CN at an applied potential of -0.1 V vs. Ag/AgCl(aq) for 5 minutes. The electrode then rinsed with CH_3CN and placed in *NP-free* 1.0 M Bu_4NClO_4/CH_3CN solution and scanned over -0.1 to 1.0 V vs. Ag/AgCl(aq) potential window to determine Γ_{NP}. The experiment was also repeated for applied potentials of -0.2, -0.4, -0.5, -0.75, and -1.0. The corresponding surface coverages are 11.1, 9.4, 9.2, 8.9, 8.6, and 8.0 X 10^{-12} mol/cm^2 for –0.1, -0.2, -0.4, -0.5, -0.75, and -1.0 V vs. Ag/AgCl (aq), respectively, see Figure 2.3. These results show an exponential decay of surface coverage against the initial applied potential.

Over the change of potential from -0.1 to -1.0 V, the surface coverage decreased to 8.8 x 10^{-12} mol/cm^2, which is almost two monolayers of NP ($\Gamma_{MONO,NP}$ = 5.2 X 10^{-12} mol/cm^2). Increasing amounts of electrolyte cation adsorb on the electrode surface as a more negative potential is applied. The electrode surface now appears positively charged resulting in repulsive interactions between the NP and the electrode surface. What is significant is that

the coverage does not decrease to zero, implying that the lateral interactions between particles are important for imparting stability in the film.

Solvent Effects on Adsorbed Au_{225}(TEA-thiolate)$_{22}$(SC6Fc)$_9$ Film. The stability and the surface coverage of the NP film were also investigated in various organic solvents. In this study the film was prepared in CH_3CN and then transferred to *NP-free* electrolyte in various solvents. A fresh film was prepared for each solvent. Adsorption was carried out by cyclically scanning the electrode in unstirred 0.05 mM Au_{225}(TEA-thiolate)$_{22}$(SC6Fc)$_9$ solutions of 0.1 M Bu_4NClO_4/CH_3CN, over the potential limits of -0.1 to 1.0 V vs Ag/AgCl (aq) for one full cycle. The electrode was then rinsed with CH_3CN and transferred to fresh 0.1 M Bu_4NClO_4/CH_3CN solution. Coverage was 24.2 x 10^{-12} mol/cm^2. Under similar reaction conditions and reagent concentrations, films was prepared in CH_3CN and transferred to various solvents, such as THF, CH_3OH, and CH_2Cl_2. Figure 2.4 shows the cyclic voltammogram of adsorbed NP film in different solvents. The coverages in CH_3CN and CH_2Cl_2 are 8.7 and 8.4 X 10^{-12} mol/cm^2, respectively. In comparison the Γ_{NP} for THF and CH_3OH are lower, with both these solvents having Γ_{NP} of 6.9 X 10^{-12} mol/cm^2, see Table 2.2.

ΔE_{peak} values of NP films in different solvents reveal that the flow of current from the adsorbed layer to the electrode experiences resistance. The ΔE_{peak} values of an adsorbed film in CH_3CN, CH_2Cl_2, CH_3OH, and THF are 28, 108, 66, and 305 mV respectively. In an ideal situation, ΔE_{peak} value should not change with solvent if the adsorbed layer's resistance involved fast heterogeneous electron transfer. This phenomenon is a defining characteristic of an uncompensated ohmic resistance. The stability of the NP film in all the above-mentioned solvents was also investigated, and it found that the films are stable in organic

Figure 2.3. Comparison of surface coverage of adsorbed film at different initial applied potential, V vs. Ag/AgCl (aq). The current vs. time (i-t) experiment was carried out for five minutes of 0.05 mM Au_{225}(TEA-thiolate)$_{22}$(SC6Fc)$_9$ in 1.0 M Bu_4NClO_4/CH_3CN at different initial potential. The electrode then rinsed and transferred to *NP-free* 1.0 M Bu_4NClO_4/CH_3CN solution and scanned over -0.1 to 1.0 V vs. Ag/AgCl (aq) at a scan rate of 0.5 V/s to determine coverage.

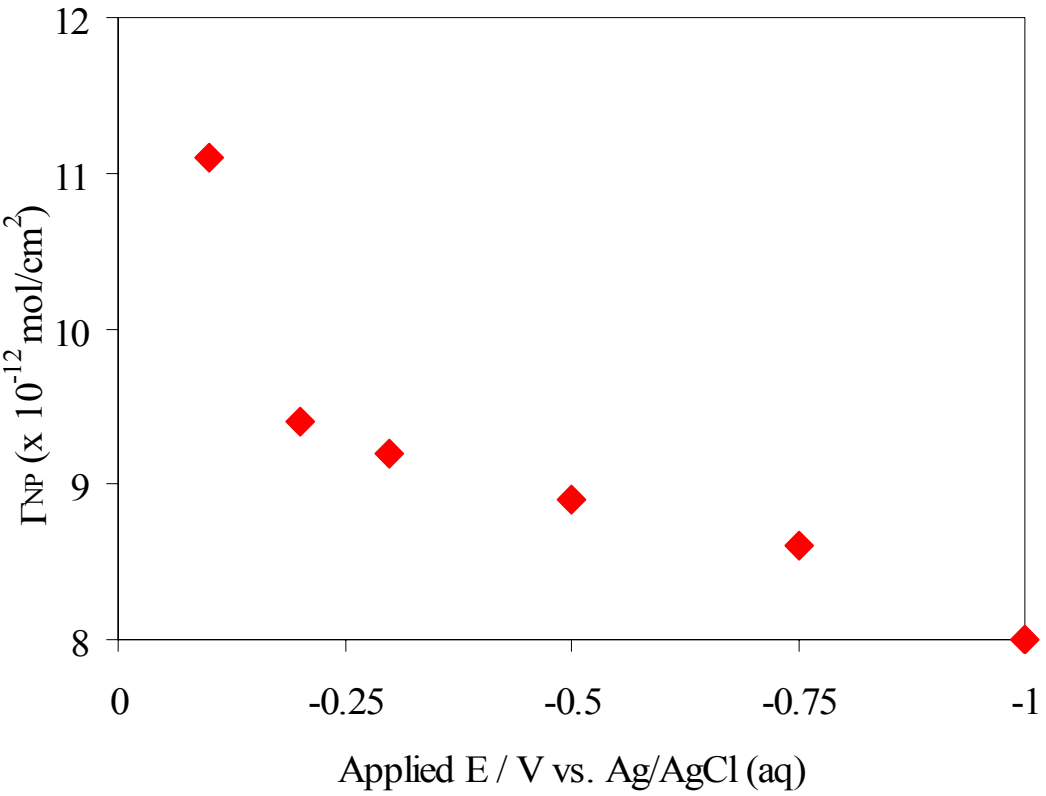
12
11
10
9
8
Γ_{NP} (x 10^{-12} mol/cm^2)
0
-0.25
-0.5
-0.75
-1
Applied E / V vs. Ag/AgCl (aq)

solvents. For example, in THF, after 25 potential cycles between -0.1 to 1.0 V vs. Ag/AgCl (aq), there is only a 3% loss between the first and 50th scan.

Study the Coverage of Au_{225}(TEA-thiolate)$_{18}$(SC_6Fc)$_{13}$ vs. Au_{225}(TEA-thiolate)$_{22}$(SC_6Fc)$_9$ vs. Au_{225}(TEA-thiolate)$_{27}$(SC_6Fc)$_4$. So far, we have discussed about the film formation of Au_{225}(TEA-thiolate)$_{22}$(SC6Fc)$_9$ and various interactions present to create stable films on the electrode surface. We have also seen that, the $E_{fwhm,OX}$ is 89 mV, which is higher than the values, 35 mV, that we have reported in our previous publication for fully-ferrocenated NP.[2,3] We mentioned that the very sharp peaks and $E_{fwhm} < 90$ suggested that there were multiple ferrocenium/X^-/ferrocenium lateral interaction.[45,46] The $E_{fwhm,OX}$ of Au_{225}(TEA-thiolate)$_{22}$(SC6Fc)$_9$ film, 89 mV implies negligible ferrocenium/X^-/ferrocenium lateral interaction, which makes sense as in the NP, the few ferrocene groups that are present could be well distributed through out the nanoparticle surface and less likely to interact. Additionally, the ferrocene thiols are shorter in length than the TEA-thiol and therefore embedded inside the monolayer. In order to prove the fact more in detail, we compared Au_{225}(TEA-thiolate)$_{18}$(SC6Fc)$_{13}$, Au_{225}(TEA-thiolate)$_{22}$(SC6Fc)$_9$, and Au_{225}(TEA-thiolate)$_{27}$(SC6Fc)$_4$ films. In Au_{225}(TEA-thiolate)$_{27}$(SC6Fc)$_4$, the number of ferrocene groups (4 Fc) reduced by more than half than Au_{225}(TEA-thiolate)$_{22}$(SC6Fc)$_9$ (9 Fc). The Au_{225}(TEA-thiolate)$_{27}$(SC6Fc)$_4$ and Au_{225}(TEA-thiolate)$_{18}$(SC6Fc)$_{13}$ films were prepared as described before (see the experimental section) and transferred to *NP-free* 1.0 M Bu_4NClO_4/CH_3CN solution. The surface coverage, 10.5 x 10^{-12} mol/cm^2, is higher than the film produced by Au_{225}(TEA-thiolate)$_{22}$(SC6Fc)$_9$, 9.3 x 10^{-12} mol/cm^2. Finally, a Au_{225}(TEA-thiolate)$_{18}$(SC_6FC)$_{13}$ film was prepared the same way as the other two films and coverage was determined to be 4.6 x 10^{-12} mol/cm^2. Comparing the three values, it is not surprising

Figure 2.4. Cyclic voltammetry of adsorbed Au_{225}(TEA-thiolate)$_{22}$(SC6Fc)$_9$ for different solvents (*NP-free*) at 0.1 M $Bu_4NClO_4$with potential scan rate 0.5 V/s. The NP film was prepared in 0.05 mM Au_{225}(TEA-thiolate)$_{22}$(SC6Fc)$_9$ in 0.1 M Bu_4NClO_4/CH_3CN with potential scan rate 0.5 V/s.

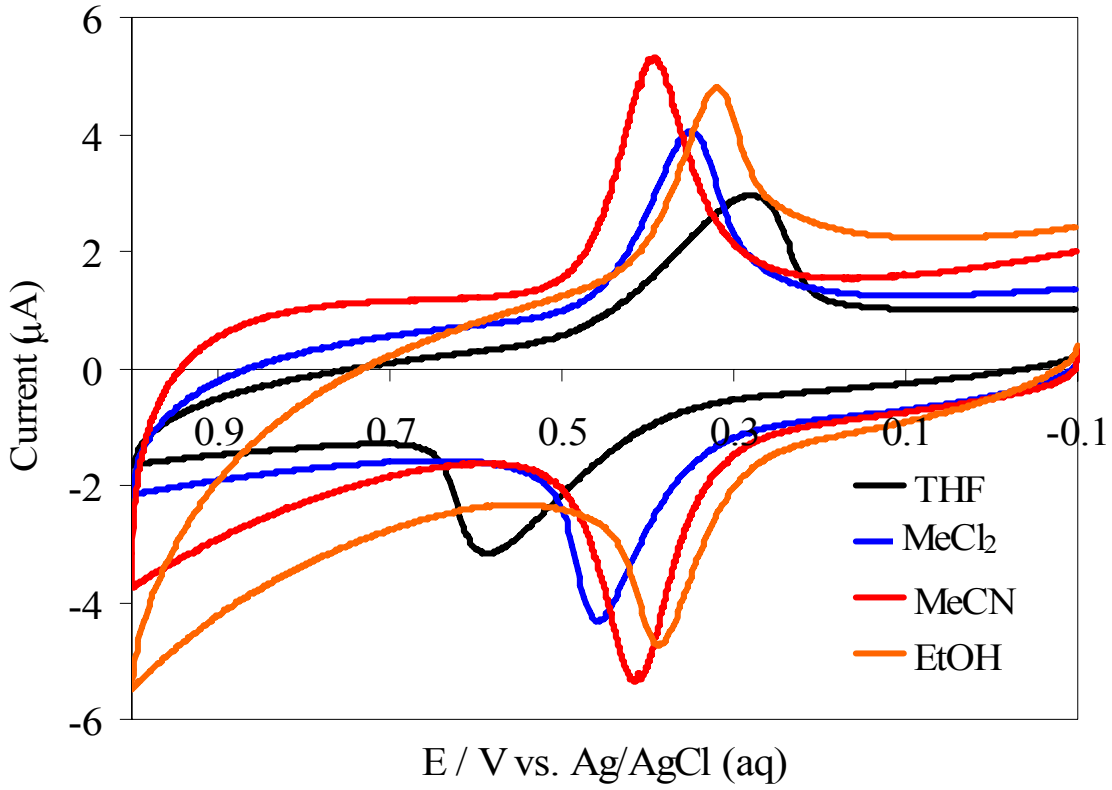
6
4
2
0
-2
-4
-6
Current (μA)
0.9
0.7
0.5
0.3
0.1
-0.1
THF
MeCl2
MeCN
EtOH
E / V vs. Ag/AgCl (aq)

Table 2.2 Effect of Solvent on Surface Coverage of Au_{225}(TEA-thiolate)$_{22}$(SC6Fc)$_9$ Adsorbed on a Pt Electrode from a 0.05 mM NP containing 0.1 M Bu_4NClO_4/CH_3CN. The Electrode was then Rinsed and Transferred to *NP-Free* 0.1 M Bu_4NClO_4 Solution in Different Solvents.[a,b]

Solvent	Γ_{NP} (x 10^{-12} mol/cm^2)
CH_3CN	8.7
CH_2Cl_2	8.4
THF	6.9
EtOH	6.9

[a]The potential scan rate is 0.5 V/s. [b]Scan between -0.1 and 1.0 V vs. Ag/AgCl (aq).

that Au_{225}(TEA-thiolate)$_{27}$(SC6Fc)$_4$ gives the highest coverage, since it more highly ionic, thereby increasing the number of vertical and horizontal interactions in the film.

Comparing the voltammetric wave-shape between Au_{225}(TEA-thiolate)$_{27}$(SC6Fc)$_4$, Au_{225}(TEA-thiolate)$_{22}$(SC6Fc)$_9$ and Au_{225}(TEA-thiolate)$_{18}$(SC6Fc)$_{13}$ reveals that $E_{fwhm,OX}$ decreased as you increase the number of ferrocene. Figure 2.5 represents the comparison of peak shape for the three different films. There are three possible reasons for why E_{fwhm} can increase above 90 mV, repulsive interactions,[54-57] spatial distribution of redox sites,[58,59] and a distribution of formal potentials.[60] The attractive or repulsive forces between two species are driven by the activities. Separating the activity of the highly charged particle from the activity of the ferrocene is likely not possible and the overall repulsive forces between the highly charged particles play some role in increasing E_{fwhm}. Secondly, the ferrocene sites on the particles are likely randomly distributed creating a spatial distribution of redox sites in the films. Thirdly, these sites may have slightly different environments, creating the opportunity for different ferrocene formal potentials. Finally, our group has previously seen no evidence of peak broadening or narrowing for the mixed-monolayer NP, $Au_{144}(SC_6)_{45}(SC_6Fc)_{15}$. Submonolayer films were produced in this instance indicating that the driving force for formation was ion-pair interaction between ferrocenium and electrolyte anions on the surface of the electrode. We can now reasonably conclude that the main reason for an increase in $E_{fwhm,OX}$ for Au_{225}(TEA-thiolate)$_{18}(SC_6Fc)_{13}$, Au_{225}(TEA-thiolate)$_{22}(SC_6Fc)_9$ and Au_{225}(TEA-thiolate)$_{27}(SC_6Fc)_4$ compared to [$Au_{225}(SC_6Fc)_{43}$] is repulsive interactions due to the highly charged particles, however we cannot definitively say that a spatial distribution of redox sites and a distribution of formal potentials do not contribute to the increase in E_{fwhm}.

Figure 2.5. Cyclic voltammetry of adsorbed NP in 1.0 M Bu_4NClO_4/CH_3CN with potential scan rate 0.5 V/s. The NP films were prepared in 0.05 mM $Au_{225}(TEA\text{-}thiolate)_{18}(SC6Fc)_{13}$, $Au_{225}(TEA\text{-}thiolate)_{22}(SC6Fc)_9$ or $Au_{225}(TEA\text{-}thiolate)_{27}(SC6Fc)_4$ in 1.0 M Bu_4NClO_4/CH_3CN with potential scan rate 0.5 V/s and then transferred to the same concentration *NP-free* 1.0 M Bu_4NClO_4/CH_3CN electrolyte solution.

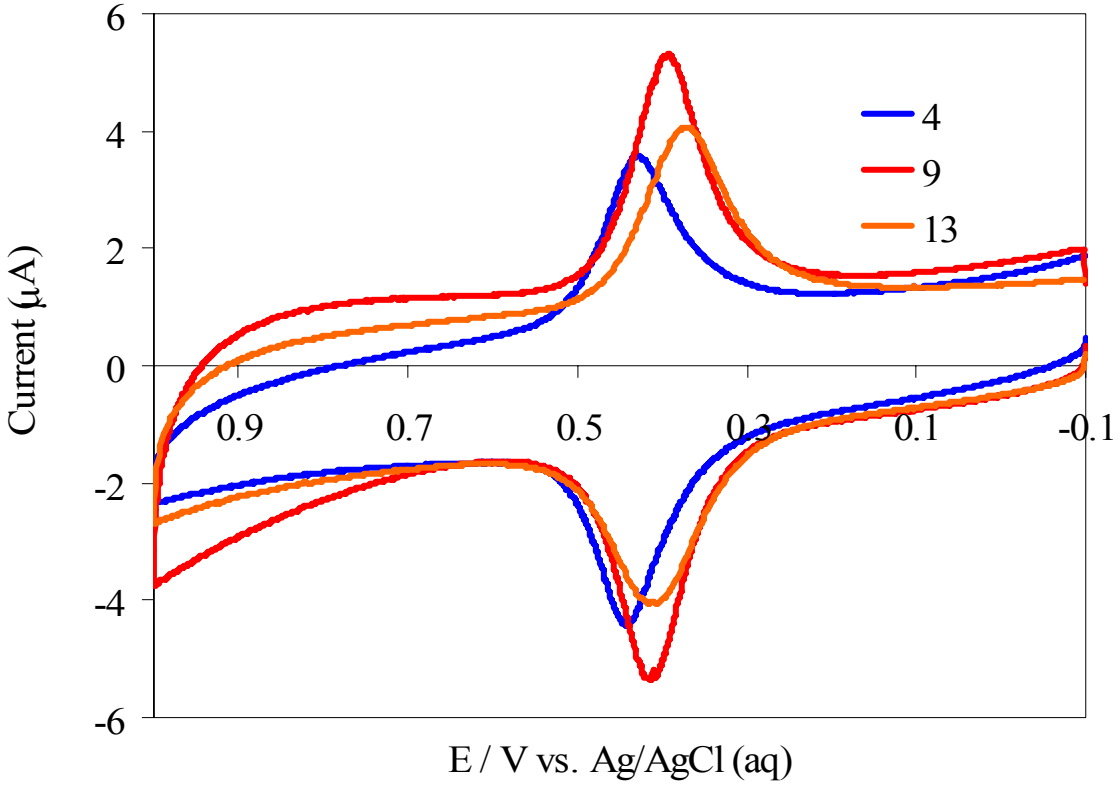
6
4
2
0
-2
-4
-6
Current (μA)
0.9
0.7
0.5
0.3
0.1
-0.1
E / V vs. Ag/AgCl (aq)
4
9
13

Study of the Adsorption of Au_{225}(TEA-thiolate)$_{22}$(SC_6Fc)$_9$ in Different Supporting Electrolyte. The results we discuss so far provide us substantial information regarding the mixed-NP adsorption on the electrode surface for a particular electrolyte, Bu_4NClO_4. The remaining part of this report will be focused on the effect of various electrolytes on film formation,. For this investigation, we used electrolytes with varying anions, $Bu_4N^+X^-$ (X^- = ClO_4^-, PF_6^-, or *p*-toluene sulfonate$^-$)

Previously we have reported that the supporting electrolyte varying anions have strongly influenced the film coverage as well the stability of the film.[2] Comparing the values of Γ_{NP} for fully-ferrocented NPs, we observed the coverage for 1.0 M Bu_4NClO_4 is less than that for the same concentration of Bu_4NPF_6 and no film was detected for 1.0 M of $Bu_4NC_7H_7SO_3$. In the present study we observe the same trend in coverage for Au_{225}(TEA-thiolate)$_{22}$(SC6Fc)$_9$ in the presence of 1 M Bu_4NClO_4 and 1 M Bu_4NPF_6. We also observed film formation for $Bu_4NC_7H_7SO_3$. Figure 2.6 represents the cyclic voltammogram of the NP film in three different electrolytes. The Γ_{NP} is strongly dependent on the particular electrolyte anion used, see Table 2.3. The Γ_{NP} results in Table 2.3 taken under *survey* experiments with potential scanning, are all greater than the model estimate for a full monolayer ca. 5.2 x 10^{-12} mol/cm^2. We have seen before that adsorption did not take place for $Bu_4NC_7H_7SO_3$ even at high concentration in solution, but for Au_{225}(TEA-thiolate)$_{22}$(SC_6Fc)$_9$, the Γ_{NP} is17.3 x 10^{-12} mol/cm^2.

Figure 2.6. Cyclic voltammetry of adsorbed NP in different electrolytes with potential scan rate of 0.5 V/s. The NP films were prepared in 0.05 mM Au_{225}(TEA-thiolate)$_{22}$(SC6Fc)$_9$ in 1.0 M electrolyte/CH_3CN with potential scan rate 0.5 V/s and then transferred to the same concentration *NP-free* same electrolyte/CH_3CN solution. The electrolytes, $Bu_4NC_7H_7SO_3$, Bu_4NClO_4, and Bu_4NPF_6 were used in the investigation.

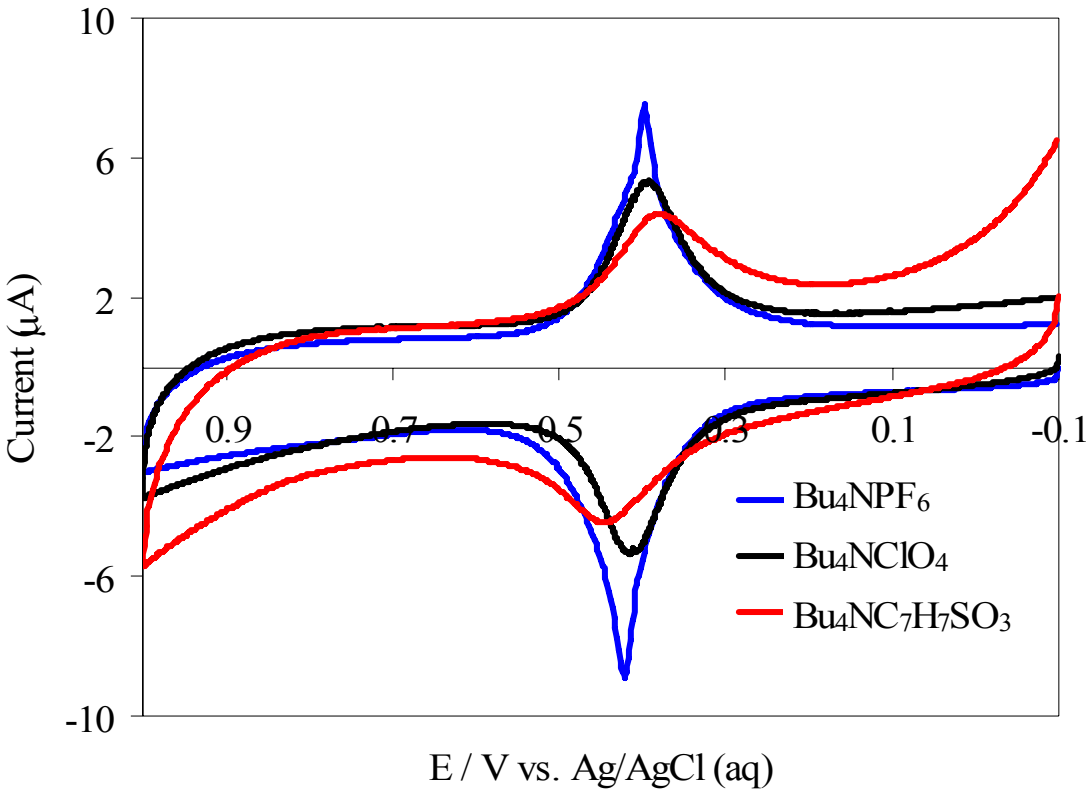
10
6
2
-2
-6
-10
Current (μA)
0.9
0.7
0.5
0.3
0.1
-0.1
E / V vs. Ag/AgCl (aq)
Bu4NPF6
Bu4NClO4
Bu4NC7H7SO3

Table 2.3. Effect of Supporting Electrolyte Anion on Surface Coverage of Au_{225}(TEA-thiolate)$_{22}$(SC6Fc)$_9$ Adsorbed on a Pt Electrode from a 0.05 mM NP solution/CH_3CN. The Electrode was then Rinsed and Transferred to *NP-free* Electrolyte Solution at the Same Concentration.[a,b]

Supporting Electrolyte	[Supporting Electrolyte]	Γ_{NP} (x 10^{-12} mol/cm^2)
$Bu_4NC_7H_7SO_3$	1.0	6.2
Bu_4NClO_4	1.0	9.3
Bu_4NPF_6	1.0	12.5

[a]The potential scan rate is 0.5 V/s. [b]Scan between -0.1 and 1.0 V.

2.4 Conclusions

In conclusion, we have successfully demonstrated that incorporation of permanent positive charge, $[-N^{+}(CH_2CH_3)_3]$ on NP substantially influences the coverage on an electrode. Depending on the reaction conditions, single to multilayers of NP were assembled on the electrode surface in a single potential scanning of the electrode. The high surface coverage and multilayer films imply a large number of lateral interactions have taken place through ion-pair formation. Additionally, the highly-ionic NPs formed ion-pairs with negatively charged anions adsorbed on the electrode surface, which produced a stably adherent film. High surface coverage was obtained even at low supporting electrolyte concentration. This proved our initial hypothesis that in order to have various interactions, some form of positive charge should present on the NP surface. The *no-scan survey* experiments suggested that, bridging ion-pair interaction is present. The NP adsorption on electrode surface is sensitive to the initial applied potential of the electrode in NP/electrolyte solution. The as-prepared NP film was shown to be stable in variety of solvents. The $E_{fwhm,OX}$ of the ferrocene oxidation peak depends upon the number of ferrocene on the particle and is larger than those measured for fully-ferrocenated NPs.

2.5 Acknowledgments

This research was supported part of grants from National Science Foundation and Office of Naval Research.

2.6 References

1. Wolfe, R. L.; Balasubramanian, R.; Tracy, J. B.; Murray, R. W. *Langmuir* **2007**, *23*, 2247−2254.
2. Stiles, R. L.; Balasubramanian, R.; Feldberg, S. W.; Murray, R. W. *J. Am. Chem. Soc.* **2008**, *130,* 1856-1865.

3. Sardar, R.; Beasley, C. A.; Murray, R. W. *Anal. Chem.* 2009, *81,* 6960-6965.

4. Daniel, M. C.; Astruc, D. *Chem. Rev*. **2004**, *104*, 293-346 and references therein.

5. Plillips, R, L.; Miranda, O. R.; You, C.-C.; Rotello, V. M.; Bunz, U, H. F. *Angew. Chem. Int. Ed*. **2008**, *47*, 2590-2594.

6. Thomas, K. G.; Kamat, P. V. *Acc. Chem. Res*. **2003**, *36*, 888-898.

7. Maier, S. A.; Kik, P. G.; Atwater, H. A.; Meltzer, S.; Harel, E.; Koel, B. E.; Requicha, A. A. G. *Nat. Mater*. **2003**, *2*, 229-232.

8. Shipway, A. N.; Lahav, M.; Blonder, R.; Willner, I. *Chem. Mater*. **1999**, *11*, 13-15.

9. Katz, E.; Willner, I. *Angew. Chem., Int. Ed*. **2004**, *43*, 6042-6108.

10. Murray, R. W. *Chem. Rev*. **2008**, *108*, 2688-2720.

11. Ingram, R. S., Hostetler, M. J., Murray, R. W., Schaaf, T. G., Khoury, J., Whetten, R. L., Bigioni, T. P., Guthrie, D. K., and First, P. N. *J. Am. Chem. Soc*. **1997**, *119,* 9279-9280.

12. Chen, S. W.; Ingram, R. S.; Hostetler, M. J.; Pietron, J. J.; Murray, R. W.; Schaaff, T. G.; Khoury, J. T.; Alvarez, M. M.; Whetten, R. L. *Science* **1998**, *280*, 2098-2101.

13. Templeton, A. C., Wuelfing, W. P., and Murray, R. W. *Acc. Chem. Res*. **2000**, *33*, 27-36.

14. Quinn, B. M., Liljeroth, P., Ruiz, V., Laaksonen, T., and Kontturi, K. *J. Am. Chem. Soc*. **2003**, *125*, 6644-6645.

15. Chen, S. *J. Am. Chem. Soc*. **2000**, *122*, 7420-7421.

16. Hicks, J. F., Miles, D. T., and Murray, R. W. *J. Am. Chem. Soc*. **2002**, *124*, 13322-13328.

17. Guo, R.; Georganopoulou, D.; Feldberg, S. W.; Donkers, R.; Murray, R. W. *Anal. Chem.* **2005,** *77*, 2662.

18. Lee, D.; Donkers, R. L.; Wang, G.-L.; Harper, A. S.; Murray, R. W. *J. Am. Chem. Soc.* **2004**, *126*, 6193.

19. Katz, E.; Lioubashevski, O.; Willner, I. *Chem. Commun*. **2006**, 1109-1111.

20. Yamada, M.; Nishihara, H. *Langmuir* **2003**, *19*, 8050-8056.

21. Li, D.; Zhang, Y.; Jiang, J.; Li, J. *J. Colloid Interface Sci*. **2003**, *264,* 109-113.

22. Green, S. J.; Stokes, J. J.; Hostetler, M. J.; Pietron, J.; Murray, R. W. *J. Phys. Chem. B* **1997**, *101*, 2663-2668.

23. Hostetler, M. J.; Green, S. J.; Stokes, J. J.; Murray, R. W. *J. Am. Chem. Soc*. **1996**, *118*, 4212-4213.

24. Wolfe, R. L.; Murray, R. W. *Anal. Chem*. **2006**, *78*, 1167-1173.

25. Zamborini, F. P.; Hicks, J. C.; Murray, R. W. *J. Am. Chem. Soc*. **2000**, *122*, 4514-4515.

26. Hicks, J. F.; Seok-Shon, Y.; Murray, R. W. *Langmuir* **2002**, *18*, 2288-2294.

27. Uosaki, K.; Kondo, T.; Okamura, M.; Song, W. *Faraday Discuss*. **2002**, *121*, 373-389.

28. Brennan, J. L.; Branham, M. R.; Hicks, J. F.; Osisek, A. J.; Donkers, R. L.; Georganopoulou, D. G.; Murray, R. W. *Anal. Chem*. **2004**, *76*, 5611-5619.

29. Xu, H.; Hong, R.; Wang, X.; Arvizo, R.; You, C.; Samanta, B.; Patra, D.; Tuominen, M. T.; Rotello, V. M. *Adv. Mater*. **2007**, *19*, 1383-1386.

30. Chen, S.; Pei, R.; Zhao, T.; Dyer, D. *J. Phys. Chem. B* **2002**, *106*, 1903-1908.

31. Zhao, W. B.; Park, J.; Caminade, A, M.; Jeong, S. J.; Jang, Y. H.; Kim, S. O.; Majoral, J. P.; Cho, J.; Kim, D. H. *J. Mater. Chem.* **2009**, *19*, 2006-2012.

32. Cho, J.; Caruso, F. *Chem. Mater*. **2005**, *17*, 4547-4553.

33. Isaacs, S. R.; Choo, H.; Ko, W. B.; Shon, Y. S. *Chem. Mater*. **2006**, *18*, 107-114.

34. Zamborini, F. A.; Leopold, M. C.; Hicks, J. F.; Kulesza, P. J.; Malik, M. A.; Murray, R. W. *J. Am. Chem. Soc.* **2002**, *124*, 8958-8964.

35. Krasteva, N.; Besnard, I.; Guse, B.; Bauer, R. E.; Yasuda, A.; Vossmeyer, T. *Nano. Lett*. **2002**, *2*, 551-555.

36. Krasteva, N.; Krustev, R.; Yasuda, A.; Vossmeyer, T. *Langmuir* **2003**, *19*, 7754-7760.

37. Yu, A.; Liang, Z.; Cho, J.; Caruso, F.; *Nano. Lett*. **2003**, *3*, 1203-1207.

38. Chirea, M.; Morales-Garcia, V.; Manzanares, J. A.; Pereira, C.; Gulaboski, R.; Silva, F. *J. Phys. Chem. B* **2005**, *109*, 21808-21817.

39. Terzi, F.; Zanardi, C.; Zanfrognini, B.; Pigani, L.; Seeber, R.; Lukkari, J.; Aaritalo, T.; Kankare, J. *J. Phys. Chem. C* **2009**, *113*, 4868-4874.

40. Hao, E.; Lian, T. *Chem. Mater*. **2000**, *12*, 3392-3396.

41. Chan, E. W. L.; Lee, D. C.; Ng, Man-Kit, Wu, G.; Lee, K. Y. C.; Yu, L. *J. Am. Chem. Soc*. **2002**, *124*, 12238-12243.

42. Tien, J.; Terfort, A.; Whitesides, G. M. *Langmuir* **1997**, *13*, 5349-5355.

43. Sardar, R.; Beasley, C. A.; Murray, R. W. *J. Am. Chem. Soc.* 2010, *132,* 2058-2063.

44. Bard, A. J.; Faulkner, L. R. *Electrochemical Methods: Fundamentals and Applications*, 2nd ed.; Wiley: New York, 2001.

45. Anson, F. C.; Barclay, D. J. *Anal. Chem*. **1968**, *40*, 1791-1798.

46. Takada, K.; Diaz, D. J.; Abruna, H. D.; Cuadrado, I.; Casado, C.; Alonso, B.; Moran, M.; Losada, J. *J. Am. Chem. Soc*. **1997**, *119*, 10763-10773.

47. Decher, G. *Science* **1997**, *277*, 1232-1237.

48. Harris, J. J.; DeRose, P. M.; Bruening, M. L. *J. Am. Chem. Soc.* **1999***, 121*, 1978–1979.

49. Xiao, K.P.; Harris, J. J.; Park, A.; Martin, C. M.; Pradeep, V.; Bruening, M. L. *Langmuir* **2001**, *17*, 8236-8241.

50. Bertrand, P.; Jonas, A.; Laschewsky, A.; Legras, R. *Macromol. Rapid. Commun*. **2000**, *21*, 319-348 and references therein.

51. Dotzauer, D. M.; Dai, J.; Sun, L.; Bruening, M. L. *Nano Lett.* **2006,** *6,* 2268-2272.

52. Miles, D. T.; Murray, R. W. *Anal. Chem*. **2003**, *75*, 1251-1257.

53. Green, S. J.; Pietron, J. J.; Stokes, J. J.; Hostetler, M. j.; Vu, H.; Wuelfing, W. P.; Murray, R. W. *Langmuir* **1998**, *14*, 5612-5619.

54. Lenhard, J. L.; Murray, R. W. *J. Am. Chem. Soc.* **1978,** *100,* 7870-7875.

55. Kuo, K.-N.; Moses, P.R.; Lenhard, J. R.; Green, D. C.; Murray, R. W. *Anal. Chem.* **1979,** *51,* 745-748.

56. Smith, D. F. ; Willman, K.; Kuo, K.; Murray, R. W. *J. Electroanal. Chem.* **1979,** *95,* 217-227.

57. Abruna, H. D.; Meyer, T. J.; Murray, R. W. *Inorg. Chem.* **1979,** *18,* 3233-3240.

58. Itaya, K.; Bard, A. J. *Anal. Chem.* **1978,** *50,* 1487-1489.

59. Kaufman, F. B.; Engler, E. M. *J. Am. Chem. Soc.*, **1979,** *101*, 547–549**.**

60. Wrighton, M. S.; Palazzotto, M. C.; Bocarsly, A. B.; Bolts, J. M.; Fischer, A. B.; Nadjo, L. *J. Am. Chem. Soc.* **1978,** *100,* 7264-7271.

61. Beasley, C. A. Unpublished results, 2006.

Chapter Three

Deposition and Growth of Highly-Ionic Redox-Labeled Au Nanoparticle Films

3.1 Introduction

Herein is described the controlled electrodeposition of multi-monolayer redox-labeled highly-ionic Au nanoparticle films, of an average composition $Au_{225}(S(CH_2)_{10}COOH)_{26}(S(CH_2)_6Fc)_{17}$ (6 nm dia.). These depositions are akin to those reductively formed[1-3] in solutions of vinyl-labeled $[Ru(bpy)_3]^{2+}$ complexes, and the versatility of the depositions promises to be comparable. Scanning electron microscopy of the films on an Au electrode reveals a porous structure and significant islanding at higher coverages. Electrochemical quartz crystal microbalance (EQCM) measurements demonstrate that in electrolyte/MeCN solutions, the nanoparticle films exhibit permselective behavior in regard to counterion entry/egress, with accompanying transfer of solvent. The principal points of the chapter are that (*i*) the use of highly ionic nanoparticles allows nanoparticle electrodeposition of multilayer films, without the aid of cross-linking metal/carboxylate coordination,[4-7] (*ii*) an easily controlled growth of the multilayer nanoparticle films, whose stability is ascribed to an entropic advantage of multiple interactions per nanoparticle, and (*iii*) electron transfers within the film are facile, allowing exhaustive electrochemical reaction of the ferrocene sites attached to as many as 200 monolayers of nanoparticles (NPs). The peak potential separations (ΔE_{PEAK}) observed in

cyclic voltammograms arise solely from uncompensated resistance effects within the film, i.e., the rates of ion permeation.

Our laboratory has previously described the exceptionally strong adsorption onto electrodes, from organic media, of Au_{225} NPs multiply labeled with ferrocene redox sites and/or quaternary ammonium groups.[8-12] The nearly irreversible adsorption of fully-ferrocenated Au NPs (AuFc) onto bare electrodes and SAM-modified electrodes is believed to reflect multiple ion-pair bridges formed vertically between the NP and the electrode surface and also laterally between the NPs themselves. These stably adherent films contained electrochemically reactive surface coverages of ferrocene sites up to 3.5×10^{-10} mol/cm^2. The correspondingly strong adsorption of Au_{225} NPs (AuTEAFc) labeled with both cationic quaternary ammonium (TEA) and ferrocene (Fc) further confirmed our hypothesis[10,11] that the adsorption process was entropically driven due to the multidentate nature of interaction of the highly-ionic NPs with an electrified metal/electrolyte interface.

Considerable research has been aimed at the preparation of Au NP films for various applications, including chemiresistor and biological sensors.[13-17] The most commonly used methods for preparation of Au NP films involve transfer of Langmuir-Blodgett monolayers,[18] drop-casting,[19] and layer-by-layer film growth[20] from alternating exposure to oppositely charged NPs (LbL, both covalent and electrostatic). Leopold et al.[4] prepared films of carboxylic acid-terminated AuNPs using bridging carboxylate/metal ion coordination in a LbL-like fashion. Luo et al.[20] took advantage of hydrogen bonding between carboxylic acid groups to form films of Au NPs and study the mass flux at the film/solution interface. Variants of the bridging-ligand LbL technique have also been used to assemble nanoparticle

films of many layers.[5-7] Sih at al.[21] have prepared Au NP films using electrodeposition by polymerizing a thiophene derivative.

Fundamental understanding of NP film formation and behavior is central to the development of devices containing nanoparticles. The present paper utilizes a measurement tool, the electrochemical quartz crystal microbalance (EQCM), in the described exploration of deposition and properties. EQCM allows unique examination of mass changes associated with interfacial processes at a film/solution interface.[22,23] There is a ready analogy with redox-active polymer films, where a large body of work exists on studying film behavior, including mobile species transport across the film/solution.[24-29] Poly(vinylferrocene) (PVF) films have been the subject of many investigations due to the ease of film preparation. We make use of ideas from these earlier works in an investigation of the electrodeposition and behavior of redox-labeled, mixed-monolayer Au NP films. Coverages up to $\Gamma_{Fc} = 3.8 \times 10^{-8}$ mol Fc/cm^2 are reported. Voltammetric response with large ΔE_p for the Fc/Fc^+ couple will be discussed. Finally, a trapping phenomenon, due to Fc^+ decomposition will also be discussed.

3.2 Experimental Methods

Chemicals. *t*-Octylammonium bromide (Oct_4NBr, >98%), sodium borohydride ($NaBH_4$, >98%), *t*-butylammonium perchlorate (Bu_4NClO_4, electrochemical grade), 11-mercaptoundecanoic acid from Aldrich and toluene (reagent grade), acetonitrile (MeCN, Optima), tetrahydrofuran (THF, HPLC grade), ethanol (HPLC grade) and 1 M tetrabutylammonium hydroxide (diluted to 1 mM in THF) from Fisher were used without further purification. $HAuCl_4\ xH_2O$ (from 99.999% pure gold) was synthesized using a

literature procedure[30] and stored in a freezer at -20 °C. Water was purified using a Barnstead (Thermo Scientific, Waltham MA) NANOpure system (18 MΩ). ^{1}H NMR spectra were collected on a Varian (Cary, NC) AMX300. XPS spectra were collected on a Kratos (Chestnut Ridge, NY) Axis Ultra^{DLD} with an Al Kα 1486.6 eV source. Profilometry was performed using a Tencor (Milpitas, CA) Alphastep 200. Scanning electron microscopy and EDAX were performed on a Hitachi (Hitachi High Technologies America, Dallas, TX) S-4700 Cold Cathode Field Emission Scanning Electron Microscope with a 2.0 kV accelerating voltage.

Synthesis of Ferrocene hexanethiol. Ferrocene hexanethiol (HSC_6Fc) was synthesized as previously described.[9] ^{1}H NMR (400 MHz, CD_2Cl_2) of the thiol gave the appropriate NMR peaks: δ = 4.0 (Fc, s, 9 H), 2.49 (*CH*$_2$SH, q, 2H *J=7.2 Hz)*,, 2.30 (*CH*$_2$Fc, t, 2H, *J=7.6 Hz*), 1.56 (*CH*$_2$CH$_2$SH, m, 2 H), 1.46 (*CH*$_2$CH$_2$Fc, m, 2 H), and 1.32 (m, 4 H) ppm with no dithiol peaks (t, 4H, 2.66 ppm) present and no significant broadening, indicating that nearly all, if not all, ferrocene groups were in the reduced state .

Synthesis of Fully Ferrocenated Au Nanoparticles. $Au_{225}(SC_6Fc)_{43}$ was synthesized according to previously reported literature.[8] Briefly, 3.19 g $HAuCl_4 \bullet xH_2O$ was dissolved in 100 mL deionized water with constant stirring. Separately, 5.20 g Oct_4NBr was dissolved in 200 mL toluene and added to the gold salt solution and the stirring was continued for 30 minutes at room temperature until a clear aqueous phase and an orange-brown toluene phase resulted. The aqueous phase was removed, and HSC_6Fc (2:1 ligand-to-Au mole ratio) was added to the organic solution. After 20 minutes of stirring the solution became clear indicating formation of the Au(I)-thiolate polymer. This solution was then placed in an ice

bath. 3.8 g of $NaBH_4$ was dissolved in 20 mL water and the solution was cooled to 0 ^{0}C for 30 minutes after which time it was added to the Au(I)-thiolate polymer solution with vigorous stirring. Immediately after the addition of reducing agent, the solution turned black and formation of gas was observed. Rapid stirring was continued for 1 h at 0 °C, after which the dark organic phase was collected and the solvent removed on a rotary evaporator at room temperature. The black solid suspension was stirred in 400 mL of MeCN for 6 h, and the solid product collected and washed with MeCN on a fine glass frit. The average Au core size and the number of ligands, as presented elsewhere,[8] were based on transmission electron microscopy, UV-vis absorbance spectroscopy, cyclic and differential pulse voltammetry, and constant potential coulometry.

Ligand Exchange Synthesis of Mixed-Monolayer Au Nanoparticles (AuMUAFc). $Au_{225}(SC_6Fc)_{43}$ (0.3 g) was dissolved in 25 mL THF. 55 mg of 11-mercaptoundeanoic acid (MUA, ~1:1 with SC_6Fc) were added to the flask and the solution was stirred for two hours. Excess MeCN was added to the flask, resulting in precipitation. Solvent was decanted until approximately 5 mL remained. Additional MeCN was added to the flask and again solvent was decanted off until 5 mL remained. This procedure was repeated two more times at which point all solvent was removed. Product was a fine, free-flowing, black powder. ^{1}H NMR revealed no excess thiol and an *average* composition of $Au_{225}(S(C_{10}COOH)_{26}(SC_6Fc)_{17}$ (AuMUAFc) based on the ratio of Fc peaks to MUA peaks.

Electrochemistry. Depositions were carried out in 0.04 mM AuMUAFc solutions in 1 M TBAP/THF containing 0.25 eq of TBAOH (relative to MUA) by cycling the potential of the working electrode between 0 and 0.8 V. Electrodes were rinsed with copious amounts of THF and MeCN after deposition. Voltammetry of films was typically done in 0.1 M

electrolyte/MeCN solutions. Surface coverages are reported as Γ_{Fc} (mol Fc/cm^2), based on the charge, q, under the ferrocene oxidation peak using

$$q = A_m F \Gamma_{Fc} \qquad (1)$$

where A_m is the Pt working electrode area, corrected for roughness by determining the charge under the hydrogen desorption peak in voltammetry of 0.10 M H_2SO_4, using the standard 210 μC cm^{-2}.[31] The experimentally determined values of Γ_{Fc} are compared to estimates of a model monolayer, of $\Gamma_{Mono,Fc}$ = 8.8 X 10^{-11} mol Fc cm^{-2} (assuming 32.2 nm^2/ AuNP, and based on an overall particle radius of ca. 3.2 nm). A 2 mm diameter Pt disc and a Pt mesh were used as the working and counter electrodes, respectively in voltammetric and impedance studies. Ag/AgCl/ 4M KCl (aq) was used as the reference electrode. Measurements were performed on a Pine Research Instrumentation WaveNow USB Potentiostat (Raleigh, NC) or a CH Instruments model 760C Electrochemical Workstation (Austin, TX).

Electrochemical Quartz Crystal Microbalance (EQCM) studies were performed using a Stanford Research Systems QCM-200 (Sunnyvale, CA) interfaced to a PC using vendor-provided software. One inch diameter 5 MHz AT-cut quartz crystals with Cr/Au contacts were also from Stanford Research Systems. The working electrode area was 1.37 cm^2 and the area of overlap (area of resonance) between the top and bottom Cr/Au contacts was 0.4 cm^2. Simultaneously, voltammetric data were acquired using a CH Instruments model 900 electrochemical analyzer. Data were exported and combined in Microsoft® Excel 2003 or Origin® 6.1. QCM data were interpreted gravimetrically based on the Sauerbrey[32] equation

$$\Delta f = -\frac{2nf_0^2}{\left(\rho_q \mu_q\right)^{1/2}} \cdot \Delta m \qquad (2)$$

where n is the harmonic at which the crystal is drive (n = 1 in this case), f_0 is the resonant frequency of the crystal in Hz, ρ_q is the density of quartz and μ_q is the shear modulus of quartz. For a 5 MHz AT-cut quartz at room temperature, (2) simplifies to

$$\Delta f = -C_f \Delta m \qquad (3)$$

where C_f equals 56.6 Hz cm^2/ug.

Theoretical modeling of voltammograms was done using BASi DigiSim 3.03 (West Lafayette, IN). See Appendix for details regarding modeling.

3.3 Results and Discussion

Nanoparticle Characterization

^{1}H NMR (not shown) reveals peaks ascribed to both the Fc and MUA ligands and gives an *average* composition of the nanoparticles as $Au_{225}(S(CH_2)_{10}COOH)_{26}(S(CH_2)_6Fc)_{17}$ (AuMUAFc). Transmission electron microscopy (TEM) of the AuFc particles prior to ligand exchange with MUA showed that the particles had an average core diameter of 2.0 (±0.3) nm. Previous results show that similar particles do not change size upon ligand exchange.[11] Figure 1 shows voltammetry of a 0.04 mM AuMUAFc solution in 1.0 M Bu_4NClO_4/THF; there is a single redox couple feature with E^0 of 0.451 V as measured from the peak potential average. Several features are noteworthy in the voltammogram. Anodic and cathodic peak currents are different owing to the deposition of nanoparticles bearing Fc^+ sites on the electrode. The reduction peak shape is more reminiscent of a surface-localized species than a freely-diffusing one; this is seen by its scant diffusional tailing. Finally, both peaks are more narrow than typical for a diffusion-controlled one electron transfer reaction, owing to lateral interactions between Fc sites on the nanoparticles.[8,33]

Film preparation and Initial Characterization

Previous reports from our laboratory have described the formation of films of fully-ferrocenated (AuFc)[8,9] or partially-ferrocenated (AuTEAFc) AuNPs[10,11]. These stably adherent films are the result of entropic gains during adsorption due to the multidentate nature of the NP/surface interaction, analogous to Decher's[34] original work on layer-by-layer growth of polyelectrolyte films. Repeated cycling of potential through the Fc/Fc^+ couple, of a bare electrode, or of a triethylammonium thiolate ($-S(CH_2)_{11}N(CH_2CH_3)_3ClO_4$)

Figure 3.1. Cyclic voltammogram of 0.04 mM AuMUAFc in 1 M Bu_4NClO_4/THF, 0.1 V/s, 2 mm diameter Pt WE, Pt Mesh CE. Note that the dashed line represents zero current; arrow indicates direction of scan.

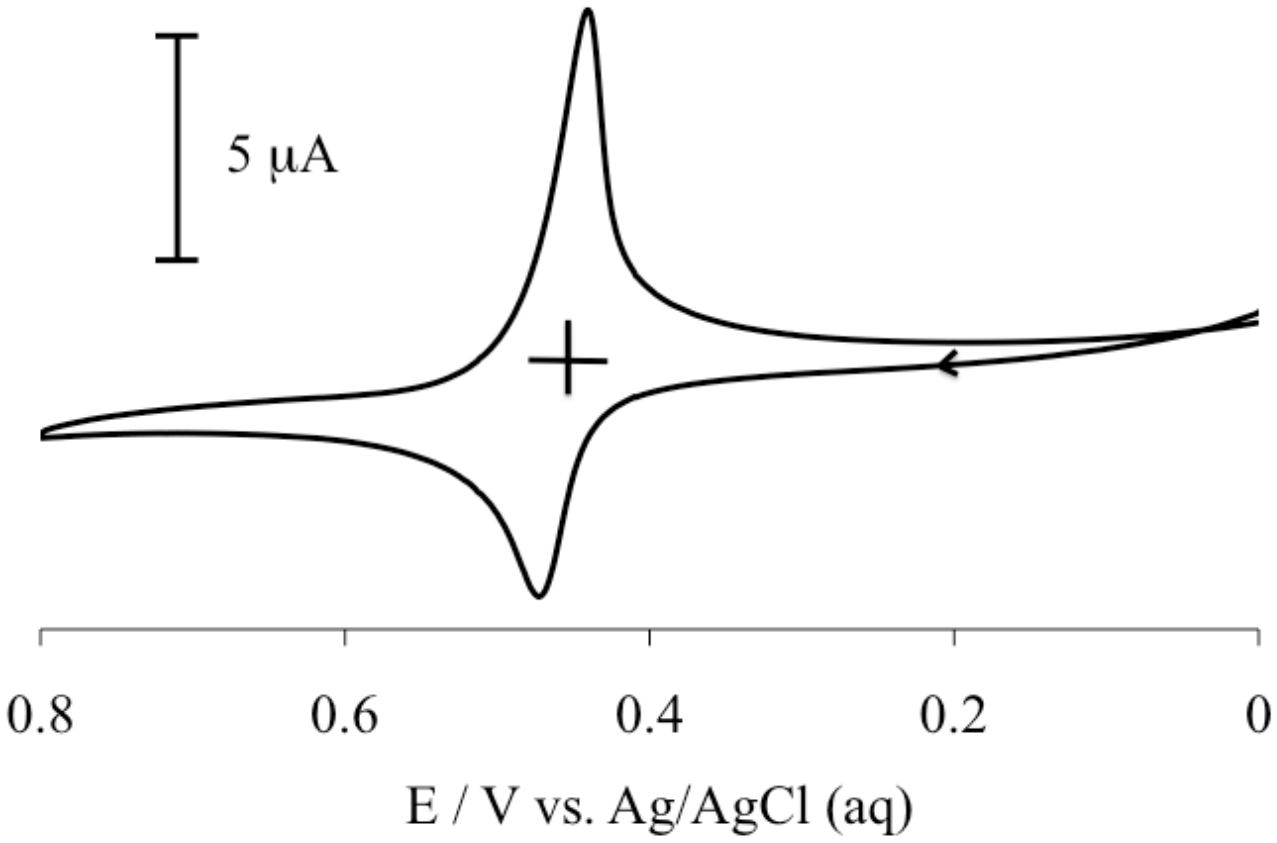
5 µA
0.8
0.6
0.4
0.2
0
E / V vs. Ag/AgCl (aq)

SAM-modified electrode, in the presence of AuFc produces films with coverages up to 2.7 x 10^{-10} and 3.5x10^{-10} mol Fc/cm^2, respectively. One complete cycle of a bare electrode in the presence of AuTEAFc produced films with coverages up to 1.1 x 10^{-10} mol Fc/cm^2. Repeated cycling produced no additional film growth for AuTEAFc. A monolayer is ca 8.8 x 10^{-11} mole Fc/cm^2.

Cycling the potential of the working electrode in a solution of the nanoparticles discussed in this report, AuMUAFc, produces stably adherent films, but, unlike AuTEAFc, repeated potential cycling cause increased and continual increases in nanoparticle film, with Γ_{Fc} values over 3.8 x 10^{-8} mol Fc/cm. Thicker films are judged to be possible but have not been investigated; at sufficiently thick films one must expect to encounter incomplete film redox transformation due to finite rates of electron-hopping charge transfer within the film during voltammetry. The discussion here will be limited to films where charge transfer is complete and concentration polarization is not significant.

Scanning electron microscopy of an AuMUAFc film, with Γ_{Fc} = 1 x 10^{-8} mol Fc/cm^2, reveals a porous film with significant islanding (Figure 3.2). Previous research[8] suggested that deposition with $Au_{225}(S(CH_2)_6Fc)_{43}$ was a stochastic process resulting in up to monolayer coverage after 25 scans. The slow deposition was thought to take place over the entire electrode surface. The deposition process reported here is more rapid, resulting in coverages equivalent to several monolayers in just one scan depending on deposition conditions. Therefore, smaller coverages were not subject to SEM at this time.

Energy Dispersive Analysis of X-Rays (EDAX), shown in Figure 3.3, confirms the presence of Fe in the islands. More uniform films can be prepared (results not shown) by first

Figure 3.2. SEM images of AuMUAFc Film electrodeposited on a quartz crystal with Cr/Au contacts by cycling 100 times at 0.1 V/s in a 0.04 mM AuMUAFc solution in 1 M Bu_4NClO_4/THF. Scale in lower right is 50 μm. Inset: Zoom of an island. Scale in lower right is 500 nm.

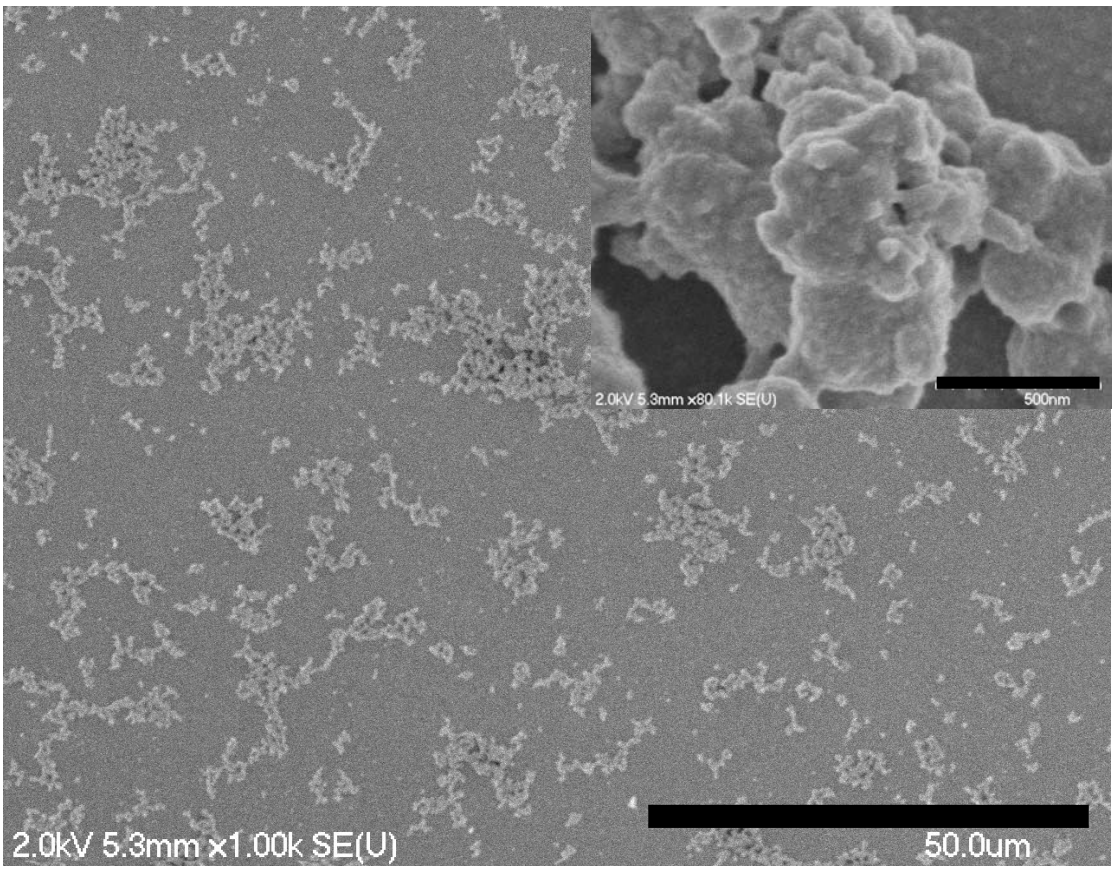
2.0kV 5.3mm x80.1k SE(U)
500nm
2.0kV 5.3mm x1.00k SE(U)
50.0um

modifying the surface of the electrode with a triethylammonium thiolate SAM prior to nanoparticle film formation, which presumably avoids or levels nucleation effects leading to larger islands. Studies utilizing such films with more uniform coverage of AuMUAFc are underway.

Average film thicknesses (ignoring islanding) based on the area under the ferrocene oxidation wave were estimated and compared with surface profilometry for purposes of modeling voltammetric responses (vide infra). Film thicknesses were estimated according to

$$d = \frac{\Gamma_{Fc}}{\Gamma_{Mono,Fc}} \cdot d_{Mono} \cdot \rho \quad (4)$$

where Γ_{Fc} the experimentally determined Fc coverage, $\Gamma_{Mono,Fc}$ is theoretical monolayer coverage (8.8×10^{-11} mol Fc/cm^2), d_{Mono} is the theoretical thickness of a monolayer (6.4 nm) and ρ is the maximum packing density for a random close pack system (0.64)[35]. Profilometry of two films showed that the theoretical thicknesses, 1.2 μm and 0.5 μm matched up reasonably well with experimentally determined average thicknesses (n = 5) of 1.5 μm and 0.6 μm, respectively. The islanding thus should not appreciably distort analysis of EQCM results.

Figure 3.3. EDAX of AuMUAFc Film electrodeposited on a QCM crystal with Cr/Au contacts by cycling 100 times at 0.1 V/s in a 0.04 mM AuMUAFc solution in 1 M Bu_4NClO_4/THF.

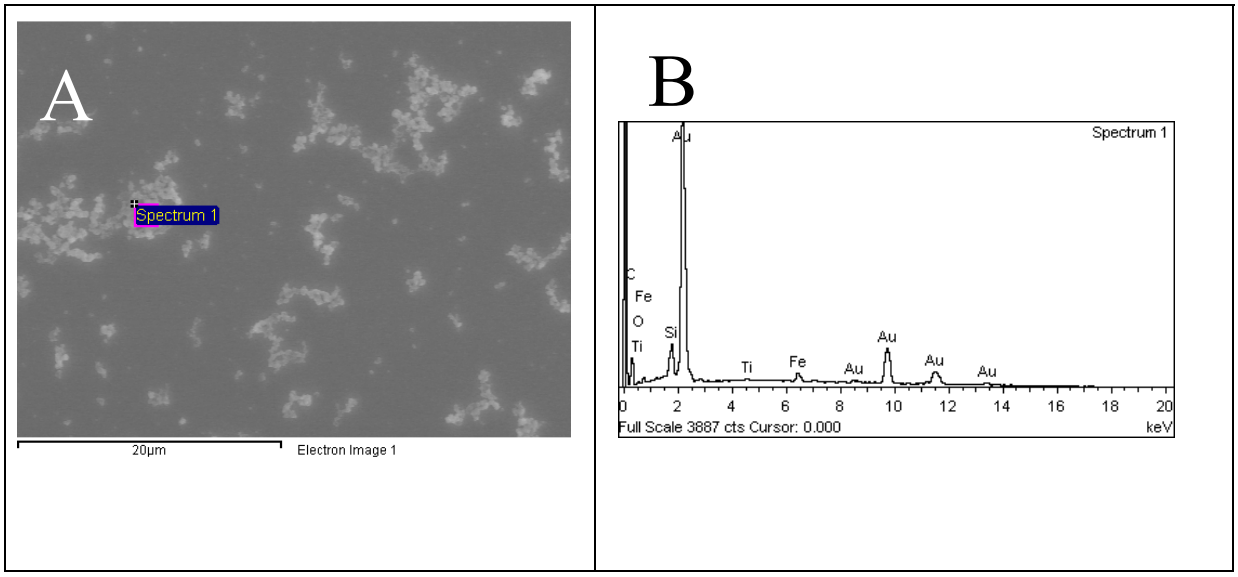
A
Spectrum 1
20µm
Electron Image 1
B
Spectrum 1
Au
C
Fe
O
Ti
Si
Ti
Fe
Au
Au
Au
Au
0
2
4
6
8
10
12
14
16
18
20
Full Scale 3887 cts Cursor: 0.000
keV

Voltammetry and Ac Impedance of AuMUAFc Films

As noted above, the potential cycling of the working electrode in the presence of AuMUAFc causes film growth. Currents of voltammograms of four different potential cycles, Figure 3.4A, during film formation increase in magnitude due to film growth. No attempt is made to interpret the overall peak shape or position during deposition. The frequency response during deposition, Figure 3.4B, shows a significant decrease indicating the addition of AuMUAFc mass to the electrode surface. The inset in Figure 3.4B is the frequency response for a single cycle (the 36^{th} of 100 cycles) during deposition. The arrows contained in the inset mark the beginning and end of the individual cycle. Note the frequency decrease overall, indicating the addition of AuMUAFc mass. The sharp frequency decrease and subsequent increase during the cycle are the entry and egress of anion and solvent during the oxidation and reduction and will be discussed later in light of film redox cycling. No attempt is made to interpret the voltammetry observed during deposition other than to note the increase in current during cycling, indicative of film growth.

Converting the frequency decrease observed during deposition to a mass correlates to a Γ_{Fc} of 8.5 x 10^{-9} mol Fc/cm^2. Voltammetry of the film at several potential scan rates after removing the QCM holder, rinsing with copious amounts of THF and MeCN, followed by immersion in 0.1 M Bu_4NClO_4/MeCN, shown in Figure 3.5, gave a calculated Γ_{Fc} of 8.3 x 10^{-9} mol Fc/cm^2, which agrees with the above mass change. The last cycle during deposition has a decrease in frequency of 150 Hz which compares well to the 125 Hz decrease obtained during cycling of the film in electrolyte. These results indicate that the mass increase is indeed correlated with the electrodeposition of ferocenated nanoparticles, and that no significant quantity is lost upon rinsing with solvent and transfer to fresh electrolyte.

Figure 3.4. EQCM of NP deposition from 0.04 mM AuMUAFc in 1 M Bu_4NClO_4/THF, 0.1 V/s, 100 Cycles. A: Black – 1st cycle, Red – 25th cycle, Orange – 50th cycle, Blue – 100th cycle. B: Frequency response during deposition. Black arrows indicate beginning and end of deposition. Inset: Frequency response for a single cycle.

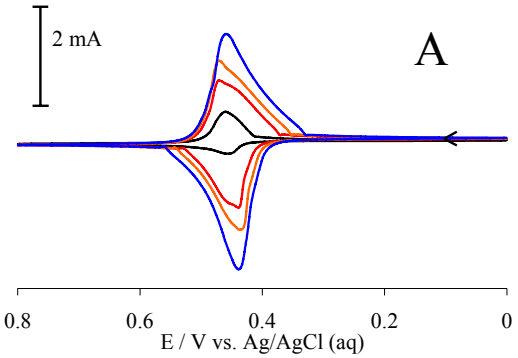
2 mA
A
0.8
0.6
0.4
0.2
0
E / V vs. Ag/AgCl (aq)

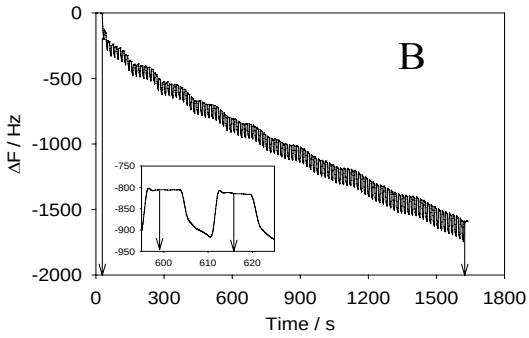
B
0
-500
-1000
-1500
-2000
ΔF / Hz
0
300
600
900
1200
1500
1800
Time / s
-750
-800
-850
-900
-950
600
610
620

Figure 3.5. Cyclic voltammetry at different scan rates of an AuMUAFc Film in 0.1 M Bu_4NClO_4/MeCN, 1.37 cm^2 Au WE, Pt mesh CE. Red – 0.005 V/s, blue – 0.01 V/s, purple – 0.02 V/s, brown – 0.05 V/s, black – 0.1 V/s. Arrow indicates direction of scan.

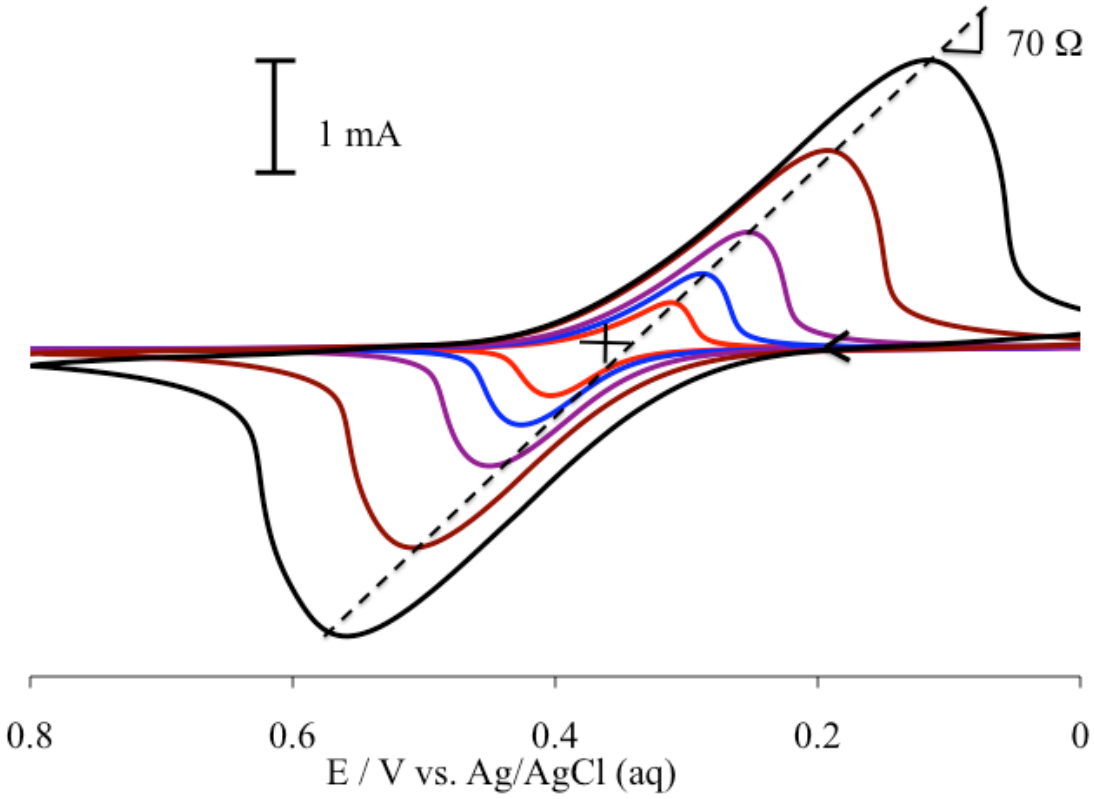
70 Ω
1 mA
0.8
0.6
0.4
0.2
0
E / V vs. Ag/AgCl (aq)

Note the large ΔE_p values in Figure 3.5. At first glance, this can be attributed to the large currents and uncompensated resistance, R_u. This is not surprising considering that voltammetry (not shown) of a 50 mM ferrocene solution (0.1 Bu_4NClO_4/MeCN), prepared to give similar currents to those observed in redox cycling of the film, has a ΔE_p of 300 mV. Even optimal electrode placement (< 1 cm separation between all three electrodes) still results in significant peak splitting. Drawing an approximate line from the anodic peaks through the cathodic peaks gives a slope of 70 Ω. Also, the absence of *significant* diffusional tailing, suggests complete charge depletion of Fc sites (i.e., no concentration polarization of Fc sites within the film on the timescales sampled here). Therefore, theoretical modeling was undertaken to confirm the peak separation was an artifact due to R_u.

The large peak separation for a film can be modeled two different ways. Method one involves inputting a large diffusion coefficient (0.999 cm^2/s in this instance) and small film thickness so that no concentration polarization occurs. This method is appropriate if only R_u is to be examined. The second method utilizes calculated diffusion coefficients and film thicknesses. We chose the latter method in order to also examine the small amount diffusional tailing observed.

Electrochemical impedance spectroscopy (EIS) was used to calculate the diffusion coefficient of ClO_4^- in the film. The diameter of the semi-circle in a Nyquist plot is a measure of the resistance to charge transfer, R_{CT} (i.e. the impedance to moving a ClO_4^- in and out of the film).[36] The R_{CT} can then be used to calculate an ionic conductivity, σ, according to the equation,

$$\sigma = \frac{d}{A}\frac{1}{R_{CT}} \qquad (6)$$

where d is the film thickness and A is the electrode area. The ionic conductivity can then be used to calculate the diffusion coefficient of an anion in the film based on the Nernst-Einstein relation,

$$\sigma = \frac{F^2}{RT}\left(z_{Fc}^2 D_{Phys} C_{Fc} + z_{ClO4}^2 D_{ClO4} C_{ClO4}\right) \qquad (7)$$

where D_{Phys} is the diffusion coefficient of Fc in the film, C_{Fc} is the concentration of Fc in the film, D_{ClO4} is the diffusion coefficient of the ClO_4^- in the film, and C_{ClO4} is the concentration of ClO_4^- in the film. The first term in the parenthesis is assigned a value of zero since the charge on Fc is zero and there is no physical diffusion of Fc in the film. Since ClO_4^- would be the counter ion to Fc^+ in the film, C_{ClO4} was assigned a value based on the probability[37] that a Fc site was oxidized to Fc^+ at 0.1 V or 0.2 V, the potentials at which EIS was performed. The probability of an Fc site being oxidized was then multiplied by the total concentration of Fc in the film (0.147 M) to give C_{ClO4}. D_{ClO4} was estimated to be 4×10^{-7} cm^2/s based on two different films (see Figures 3.6 and 3.7).

Our interpretation of the impedance data has been kept relatively simple solely for the purpose of calculating a correct order-of-magnitude diffusion coefficient. The impedance data could be modeled in a number of ways including a distribution of resistance/capacitance values due to surface inhomogeneity, inductive effects depressing the semi-circle below the x-axis and/or a distribution of resistance values due to a distribution of E^0 values associated with different Fc sites. Therefore at this time, we model our film as a simple Randles

Figure 3.6. EIS plot of a 170 nm thick AuMUAFc film in 0.1 M Bu_4NClO_4/MeCN at 0.1 V vs Ag/AgCl. 5 mV amplitude. 100 kHz to 1 Hz.

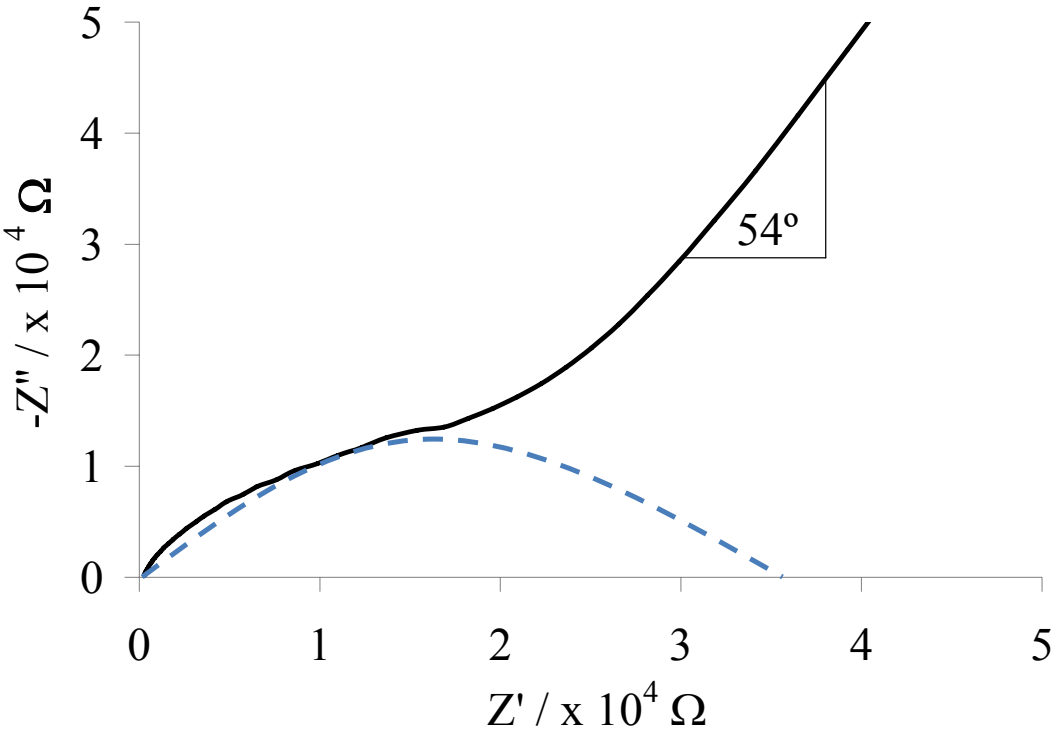
5
4
3
2
1
0
-Z'' / x 10^4 Ω
54º
0
1
2
3
4
5
Z' / x 10^4 Ω

Figure 3.7. EIS plot of an 800 nm thick AuMUAFc film in 0.1 M Bu_4NClO_4/MeCN at 0.2 V vs Ag/AgCl. 5 mV amplitude. 100 kHz to 1 Hz.

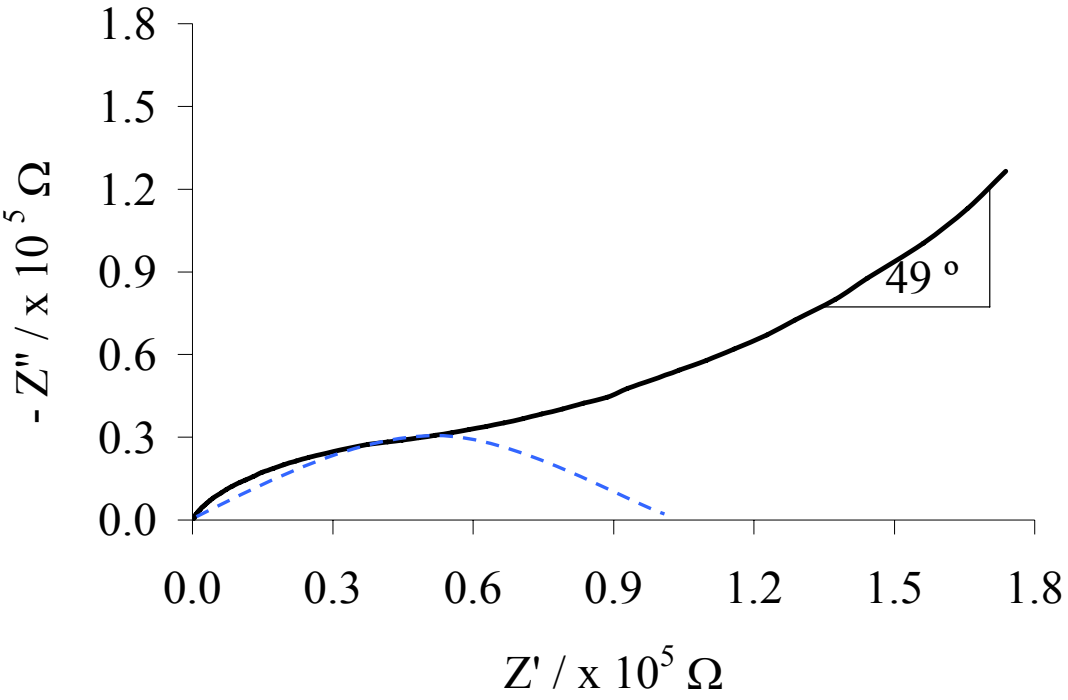
1.8
1.5
1.2
0.9
0.6
0.3
0.0
- Z'' / x 10 5 Ω
49 º
0.0
0.3
0.6
0.9
1.2
1.5
1.8
Z' / x 10^5 Ω

equivalent circuit containing a Constant Phase Element, for the purpose of grouping nonidealities,[38] in series with R_{CT}.

Feldberg recently described the effect of R_u on voltammograms of an electrochemically reversible surface attached redox couple.[39] Using Feldberg's equation R_u was calculated to be approximately 90 Ω.

Theoretical models were generated using DigiSim (see Appendix for model details) based on data extracted from experimentally obtained results. Four different comparisons, 0.01, 0.02, 0.05, and 0.1 V/s are shown in Figure 3.8. At 0.1 and 0.2 V/s, the models match up well (ΔE_p) with experimentally obtained voltammograms. At 0.5 and 0.1 V/s, ΔE_p begins to differ and more significant diffusional tailing emerges which can be modeled by increasing film thickness. Since the film varies in thickness, it is a reasonable assumption that the thicker areas of the film contribute to diffusional tailing. We will also examine an alternate possibility behind the diffusional tailing.

The hopping diffusion of the electron in films and melts is thought to be rapid since in the ion atmosphere relaxation model, self-exchange constants (k_{EX}) are typically quite high. The self-exchange constant for $Fc^{0/+}$ is indeed 8.1 x 10^6 M^{-1} s^{-1}.[40] The apparent diffusion coefficient (D_{APP})is given by the Dahms-Ruff equation[41-43]

$$D_{APP} = D_{PHYS} + D_E = D_{PHYS} + \frac{k_{EX}\delta^2 C}{6} \qquad (8)$$

where D_{PHYS} is the diffusion coefficient of Fc in the film (assumed to be zero in this case), δ is the center-to-center distance between donor and acceptor (assuming a cubic lattice

Figure 3.8. Comparison of Theoretical (black curves) and Experimental (red curves) Cyclic Voltammetry of an AuMUAFc Film in 0.1 M Bu_4NClO_4/MeCN. A – 0.01 V/s, B – 0.02 V/s, C – 0.05 V/s, D – 0.1 V/s.

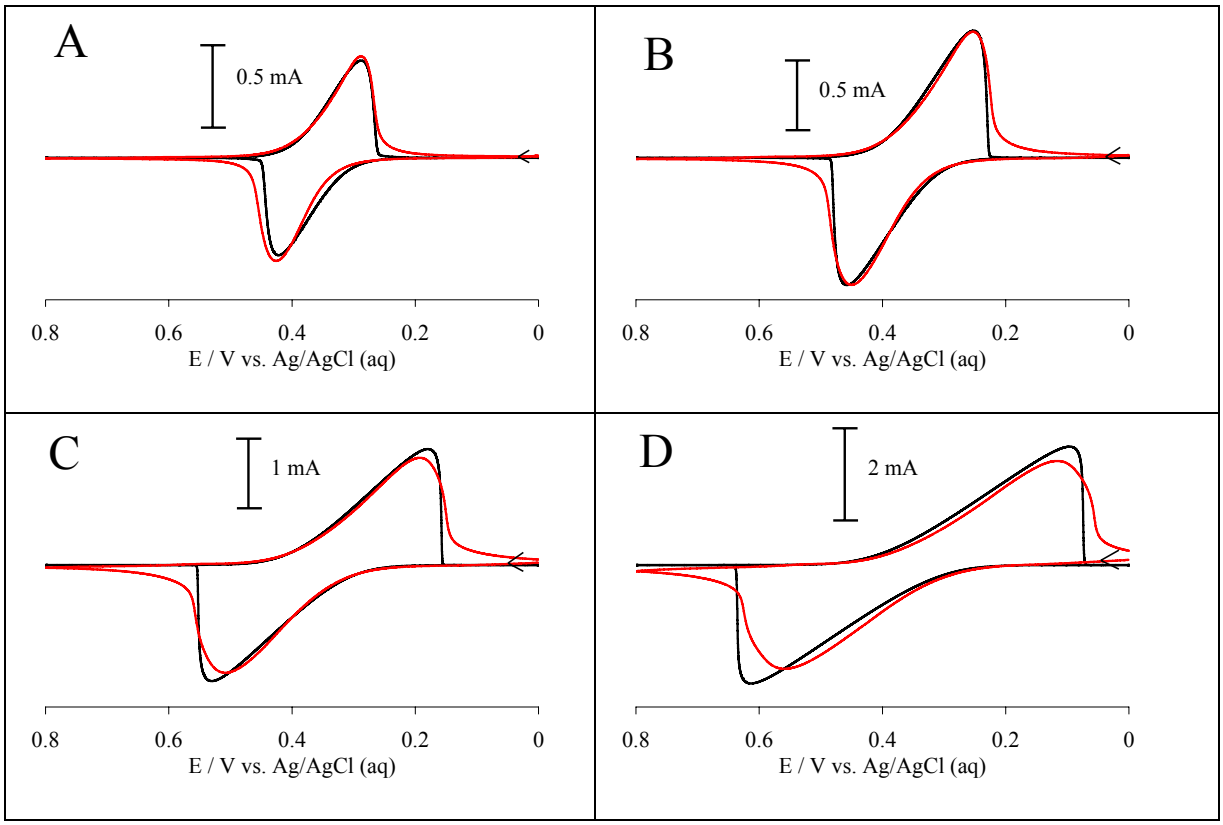
A
0.5 mA
0.8
0.6
0.4
0.2
0
E / V vs. Ag/AgCl (aq)
B
0.5 mA
0.8
0.6
0.4
0.2
0
E / V vs. Ag/AgCl (aq)
C
1 mA
0.8
0.6
0.4
0.2
0
E / V vs. Ag/AgCl (aq)
D
2 mA
0.8
0.6
0.4
0.2
0
E / V vs. Ag/AgCl (aq)

model), and C is the overall concentration of Fc in the film. Electron hopping between the Fc sites on the surface of a particle or with a neighboring particle or even with the particle core (see Figure 3.9) give the use of the cubic lattice model validity. It would also be valid to assume that electron hopping only takes place on the surface of the particle at the ends of the ligands, however, the center-to-center distance between donor and acceptor is only slightly increased from 2.24 nm to 2.58 nm. The second term in (8) is now divided by four to account for a square-planar model rather than the cubic-lattice model. D_E values for the cubic-lattice and square-planar models are 1 x 10^{-8} cm^2/s and 2 x 10^{-8} cm^2/s, respectively. This difference is not significant and therefore, the smaller cubic-lattice model value was chosen when comparing experimental voltammograms to theoretical voltammograms. Theoretical voltammograms at 0.05 V/s generated for the film discussed directly above, at varying thicknesses, using D = 1 x 10^{-8} cm^2/s, are shown in Figure 3.10. Also shown in is a theoretical voltammogram with D = 4 x 10^{-7} cm^2/s. The results show that the slower diffusion coefficient is better able to model the diffusional tailing observed experimentally. Several thicknesses are shown for comparison and show that at 50 mV/s, even doubling the film thickness surpasses the limit of complete charge accessibility on the experimental timescale. The most important conclusion from the comparisons, though, is that the peak splitting observed in the voltammograms is due solely to R_u effects.

Figure 3.9. Cartoon Representation for Mobile Species Movement during Oxidation of AuMUAFc Film in 0.1 M Bu_4NClO_4/MeCN. $C^+ = Bu_4N^+$, $A^- = ClO_4^-$, S = MeCN.

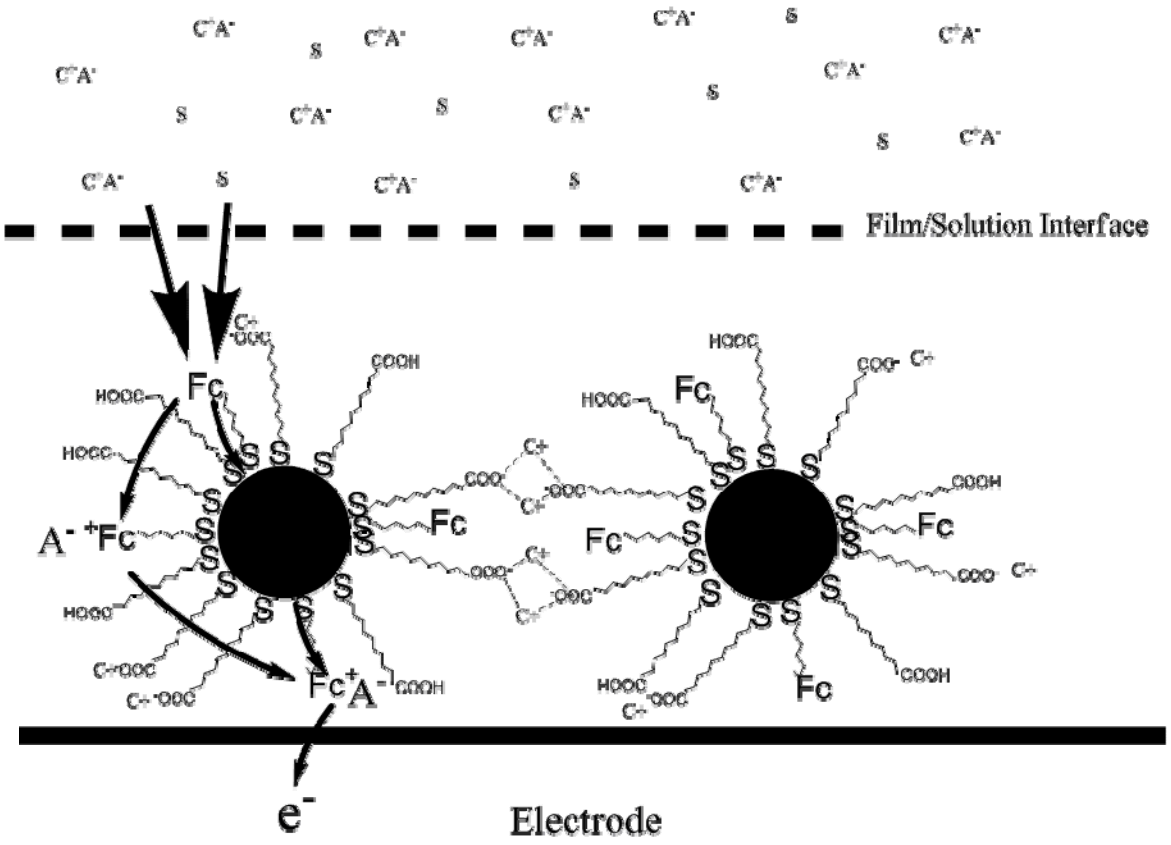
Film/Solution Interface
Fc
A⁻ ⁺Fc
Fc⁺A⁻
e⁻
Electrode

Figure 3.10. Comparison of Theoretical and Experimental Curves for Cyclic Voltammetry of AuMUAFc Films at Varying Thicknesses and Diffusion Coefficients in 0.1 M Bu_4NClO_4/MeCN at 0.05 V s^{-1}. Red – Experimental, Black – 1 μm, D = 4 x 10^{-7} cm^2/s; Orange – 1 μm, D = 1 x 10^{-8} cm^2/s; Blue – 2 μm, D = 1 x 10^{-8} cm^2/s; Green – 3 μm, D = 1 x 10^{-8} cm^2/s.

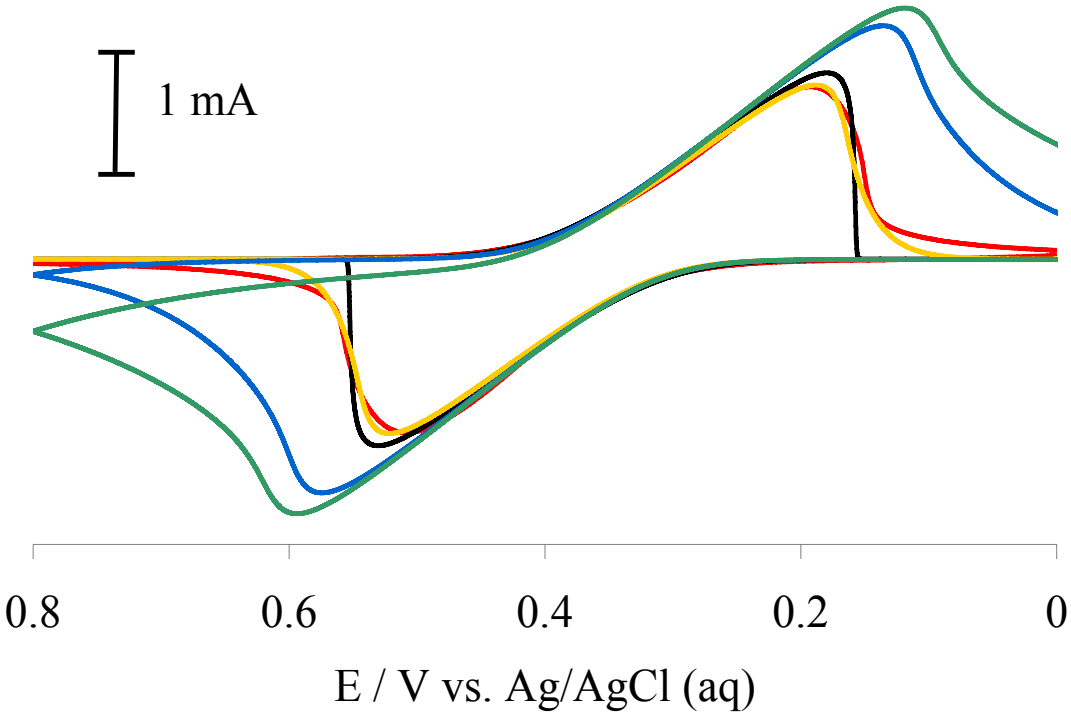
1 mA
0.8
0.6
0.4
0.2
0
E / V vs. Ag/AgCl (aq)

EQCM Behavior of AuMUAFc Films

Ion and solvent entry/egress during redox cycling of electroactive polymer films has seen extensive research.[22,25,27,29] AuMUAFc films were subjected to redox cycling while concurrently monitoring film mass changes. Mass-charge (Δm-q) plots, obtained from the combination of gravimetric and voltammetric data, provide a measure of ion, solvent and electrolyte population changes throughout a partial or complete redox cycle. Varying the experimental timescale, in the form of different scan rates, reveals differences in kinetic and thermodynamic.

The ability to access all oxidizable sites in a film is of crucial important should redox-labeled AuNPs be used to fabricate charge storage devices. The amount of charge accessed should not vary as a function of scan rate if all oxidizable sites are being accessed. Although at some higher scan rate, the amount of charge accessed will decrease due to the reduced experimental timescales preventing charge propagation through the film. Figure 3.11 is a plot charge versus the square root of the scan rate for an AuMUAFc film in 0.1 M Bu_4NClO_4/MeCN. Interestingly, the amount of charge accessed 0.005 and 0.01 V/s is less than the amount of charge accessed at 0.02, 0.05, and 0.1 V/s. Subjecting the film to repeated cycling reduces the amount of charge accessed during each cycle and also shows that the failure to return to the original film mass as shown in Figure 3.12.

The mass change during an experiment is a sum of all mobile species into and out of the film. Fc oxidation requires the injection or ejection of anion or cation, respectively in order to maintain electroneutrality throughout redox cycling. Movement of solvent into or out of

the film is necessary to maintain activity. Partitioning of supporting electrolyte (SE) is also possible. Therefore, the total mass change (Δm_T) is given by the equation

$$\Delta m_T = \Delta m_A + \Delta m_C + \Delta m_{SE} + \Delta m_S \qquad (9)$$

where Δm_A is the mass change due to anion, Δm_C is the mass change due to cation, Δm_{SE} is the mass change due to SE and Δm_S is the mass change due to solvent. During redox cycling the film gains mass continuously throughout oxidation and loses mass continuously during reduction. This result means that it is unlikely that cation is being ejected during oxidation and injected during reduction because doing so would require nonmonotonic ion flux. It is possible that cation ejection or anion injection can dominate during different parts of the cycle, as been evidenced by previous authors,[25,44] however, to the best of our knowledge no group has observed simultaneous cation ejection and anion injection. Previous work from our lab of highly ionic Au NP films support the hypothesis that the change in mass is due to anion and solvent injection during oxidation.[10,11]

The overall end-to-end (fully-reduced to fully-oxidized) slope during each cycle shown in Figure 3.12 is 200 g/mol indicating the transfer of one ClO_4^- (99.5 g/mol) and 2.45 MeCN (41 g/mol). A comparison between 0.05 M and 0.1 M Bu_4NClO_4 in MeCN (data not shown) confirmed that the trapped species was MeCN and not likely electrolyte. Based on previous EQCM;[45] and neutron reflectivity results[46] for poly(vinylferrocene) films, SE will not typically partition into films when concentrations in solution are $\leq$ 0.1 M. The slope of the Δm-q plot for 0.05 M Bu_4NClO_4 was

Figure 3.11. Plot of q vs $v^{1/2}$ for an AuMUAFc film in 0.1 M Bu_4NClO_4/MeCN.

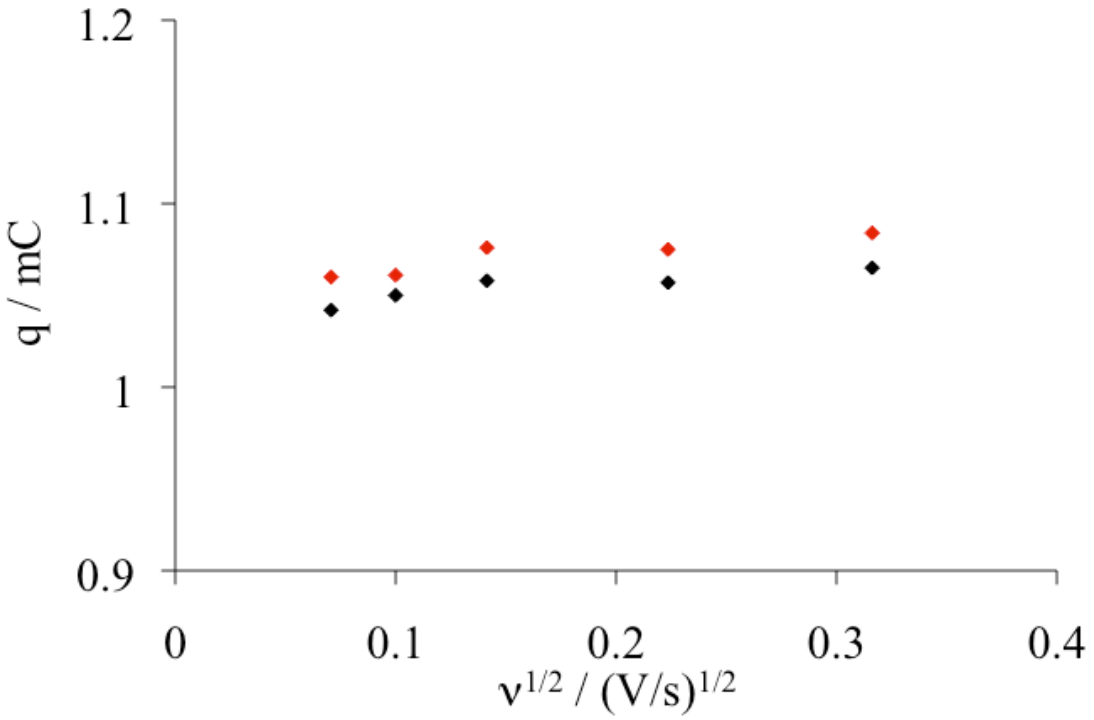
1.2
1.1
1
0.9
q / mC
0
0.1
0.2
0.3
0.4
ν^1/2 / (V/s)^1/2

Figure 3.12. Change in mass as a function of AuMUAFc Film oxidation level for five cycles at 0.005 V/s. Grey – cycle 1, Red – cycle 2, Blue – cycle 3, Maroon – cycle 4, Brown – cycle 5.

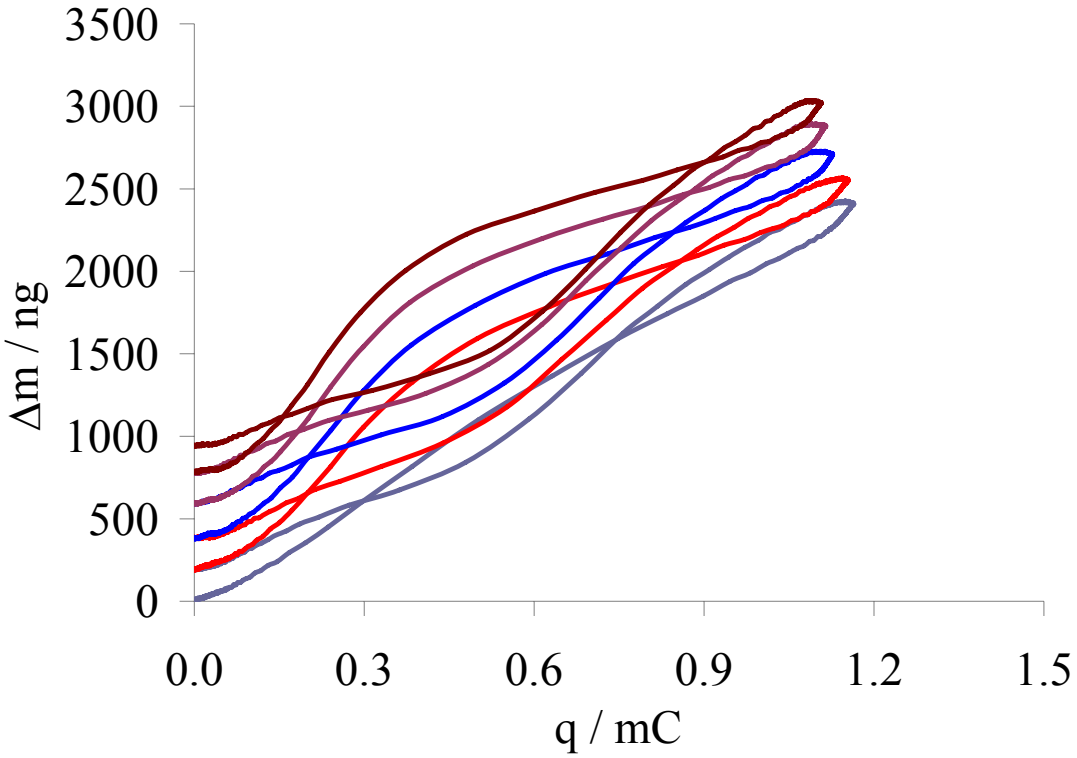
3500
3000
2500
2000
1500
1000
500
0
Δm / ng
0.0
0.3
0.6
0.9
1.2
1.5
q / mC

206 g/mol while the slope for 0.1 M Bu_4NClO_4 was 197 g/mol confirming that it is unlikely that SE is partitioning into the film and is not the source of the Fc site disconnection.

Considering the total change in mass is due to anion and solvent, the change in solvent population can be calculated throughout the complete redox cycle. The change in solvent population, not the absolute solvent population, is given by the equation

$$\Delta\Gamma_S = MM_S^{-1}\left(\Delta m_T - MM_A\frac{q}{F}\right) \qquad (10)$$

where MM_S is the molar mass of the solvent, MM_A is the molar mass of anion, q is the charge and F is Faraday's Constant.[44] The films change in solvent and ion content (directly related to charge), along with potential can be represented as a vector in 3D compositional space (E, q, $\Delta\Gamma_S$) to provide more information on kinetic and thermodynamic effects during redox cycling of the AuMUAFc film. The use of 3D compositional space to examine thermodynamic and kinetic effects of model mobile species in redox films has been studied extensively by Hillman and coworkers.[44,45] Two different scan rates were chosen to examine kinetic effects.

Figures 3.13 and 3.14 are 3D representations for an AuMUAFc film during redox cycling at 0.1 and 0.005 V/s, respectively. Hysteresis in the $\Delta\Gamma_s$-q plane at 0.1 V/s indicates differences in ion and solvent flux while curvature upwards is indicative of an attractive force between the film and solvent at low levels of film oxidation. Upon reversal, solvent exit is more linear indicating that there is neither an attractive force nor a repulsive force. This is a possible manifestation of the two-phase behavior observed by Daum and Murray[48] for PVF films in perchloric acid.

Note that at 0.005 V/s, little hysteresis is observed, meaning kinetic effects have been lessened or removed and thermodynamic effects can dominate the response. The lack of hysteresis suggests that both anion and solvent flux rates are similar. Again, as in Figure 3.12, the trapping of a species is seen as a failure of Δm to return to zero at the end of the cycle.

Plotting the real-time molar differential changes due to anion and solvent enables examination of rate limiting processing throughout the cycle. Figures 3.15 and 3.16 show the molar differentials as a function of potential for 0.1 and 0.005 V/s, respectively. The rate of transfer of MeCN during the first portion of both oxidation and reduction is initially faster than ClO_4^- at 0.1 V/s. At the end of oxidation and end of reduction, MeCN flux slows compared to ClO_4^-. The rates of transfer of MeCN and ClO_4^- during oxidation and reduction are similar throughout the complete redox cycle at 0.005 V/s and indicate that solvent egress is not thermodynamically unfavorable.

An alternative hypothesis to the decrease in charge per cycle is that Fc, once oxidized to Fc^+, is decomposing at these slow scan rates. Abbott and Whitesides[49] have reported similar phenomenon of Fc-terminated SAMs in $NaClO_4$ decomposing at oxidizing potentials. The half-life of Fc^+ in an organic solvent is typically on the order of hours. Dividing the amount of charge that becomes inaccessible per cycle by the time it takes to traverse from initial oxidation to final reduction can give a rough estimate of a half-life.

In this instance, the half-life of Fc^+ in the film ranged from 1-3 hours depending on the film. The trapping phenomenon observed at 0.005 V/s is thus likely a combination of Fc^+ decomposing and trapping solvent and electrolyte.

Figure 3.13. 3D Representation of EQCM Data for a Complete Voltammetric Cycle for an AuMUAFc Film in 0.1 M Bu_4NClO_4/MeCN at 0.1 V/s. Arrows Indicate Direction of Scan.

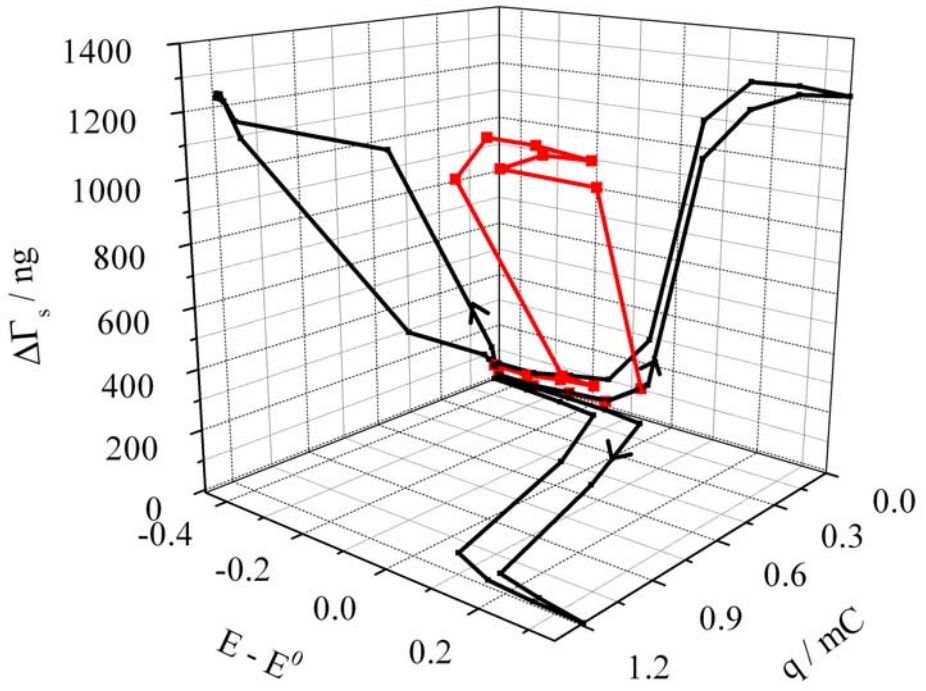
1400
1200
1000
800
600
400
200
0
$\Delta\Gamma_s$ / ng
-0.4
-0.2
0.0
0.2
E - E^o
0.0
0.3
0.6
0.9
1.2
q / mC

Figure 3.14. 3D Representation of EQCM Data for a Complete Voltammetric Cycle for an AuMUAFc Film in 0.1 M Bu_4NClO_4/MeCN at 0.005 V/s. Arrows Indicate Direction of Scan.

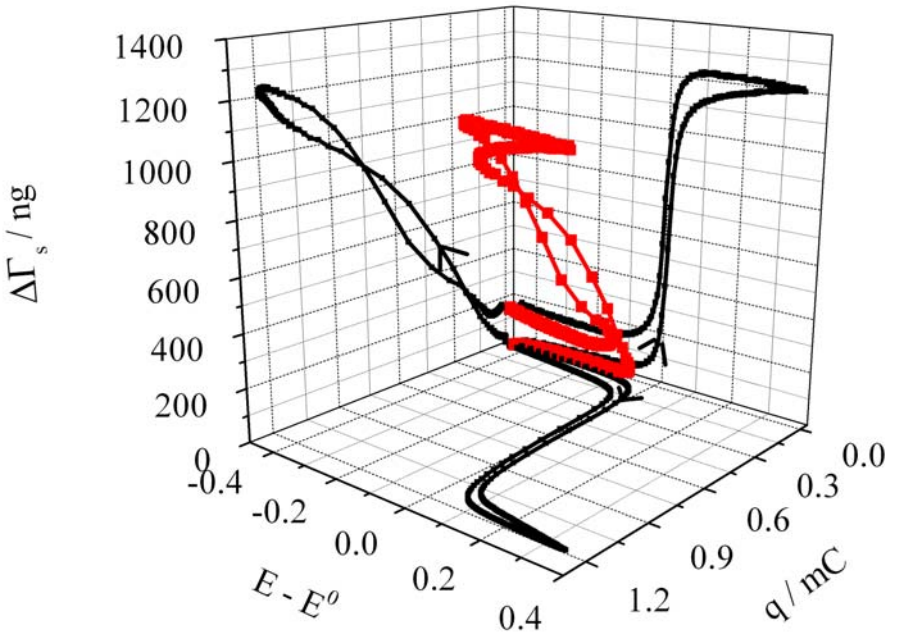
1400
1200
1000
800
600
400
200
0
$\Delta\Gamma_s$ / ng
-0.4
-0.2
0.0
0.2
0.4
E - E^o
0.0
0.3
0.6
0.9
1.2
q / mC

Figure 3.15. Mass Differential for the Redox Cycling of AuMUAFc in 0.1 M Bu_4NClO_4/MeCN at 0.1 V/s.

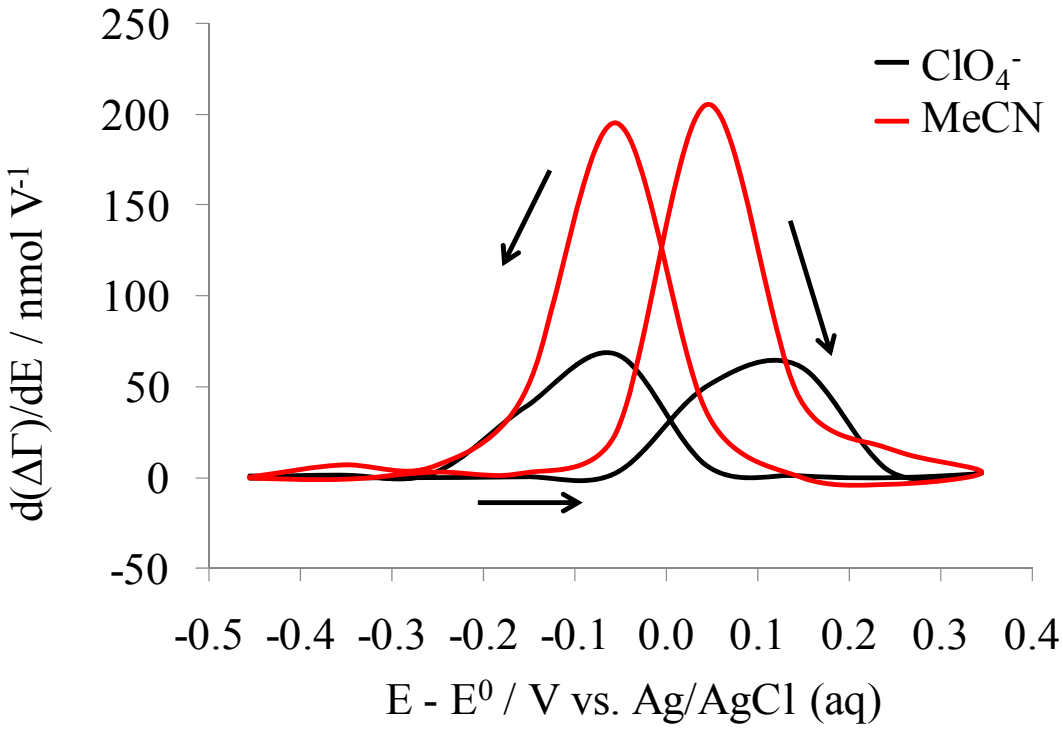
250
200
150
100
50
0
-50
d(ΔΓ)/dE / nmol V-1
ClO4-
MeCN
-0.5 -0.4 -0.3 -0.2 -0.1 0.0 0.1 0.2 0.3 0.4
E - E0 / V vs. Ag/AgCl (aq)

Figure 3.16. Mass Differential for the Redox Cycling of AuMUAFc in 0.1 M Bu_4NClO_4/MeCN at 0.005 V/s. Arrows Indicate Direction of Scan.

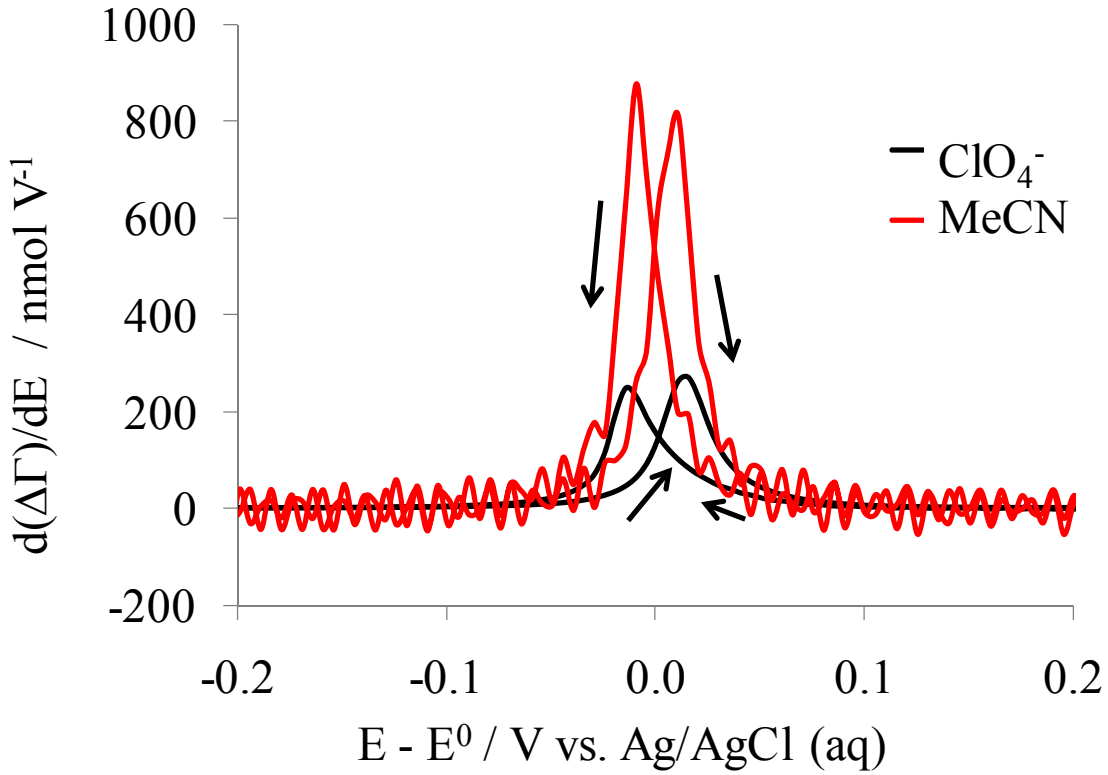
1000
800
600
400
200
0
-200
d(ΔΓ)/dE / nmol V-1
-0.2
-0.1
0.0
0.1
0.2
E - E0 / V vs. Ag/AgCl (aq)
ClO4-
MeCN

3.4 Conclusion

The controlled formation of highly-ionic AuMUAFc films simply by controlling the number of cycles during cyclic voltammetry is reported. The large ΔEp for the Fc/Fc^+ couple is attributed solely to uncompensated resistance, i.e. ion movement within the film. EQCM experiments show that anion and solvent enter during film oxidation and exit during reduction. Charge lost during each cycle at 0.005 V/s is attributed to a combination of mobile species trapping and Fc^+ decomposition during redox cycling.

3.5 Acknowledgement

This research was supported in part by grants from the Office of Naval Research and the National Science Foundation.

3.6 References

1. Abruna, H. D.; Denisevich, P.; Umana, M.; Meyer, T. J.; Murray, R. W. *J. Am. Chem. Soc.* **1981**, *103*, 1.
2. Denisevich, P.; Abruna, H. D.; Leidner, C. R.; Meyer T. J.; Murray, R. W. *Inorg. Chem.* **1982**, *21*, 2153.
3. Bommarito, S. L.; Lowery-Bretz, S. P.; Abruna, H. D. *Inorg. Chem.* **1992**, *31,* 495-502.
4. Leopold, M. C.; Donkers, R. L.; Georganopoulou, D.; Fisher, M.; Zamborini, F. P.; Murray, R. W. *Faraday Discuss.* **2004**, *125,* 63-76.
5. Russell, L. E.; Pompano, R. R.; Kittredge, K. W.; Leopold, M. C. *J. Mater. Sci.* **2007**, *42,* 7100-7108.
6. Pompano, R. R.; Wortley, P. G.; Moatz, L. M.; Tognarelli, D. J.; Kittredge, K. W.; Leopold, M. C. *Thin Solid Films* **2006,** *510,* 311-319.
7. Vakarelski, I. U.; Maenosono, R.; Kwek, J. W.; Higashitani, K. *Colloids Surf., A* **2009**, *340,*193-198.

8. Wolfe, R. L.; Balasubramanian, R.; Tracy, J. B.; Murray, R. W. *Langmuir* **2007**, *23,* 2247-2254.

9. Sardar, R.; Beasley, C. A.; Murray, R. W. *Anal. Chem.* **2009**, *81,* 6960-6965.

10. Sardar, R.; Beasley, C. A.; Murray, R. W. *J. Am. Chem. Soc.* **2010,** *132,* 2058-2063.

11. Beasley, C. A. Sardar, R.; Barnes, N. M.; Murray, R. W. manuscript in preparation.

12. Hostetler, M. J.; Green, S. J.; Stokes, J. J.; Murray, R. W. *J. Am. Chem. Soc.* **1996,** *118,* 4212-4213.

13. Yu, A.; Liang, Z.; Cho, J.; Caruso, F.; *Nano. Lett*. **2003,** *3*, 1203-1207.

14. Krasteva, N.; Krustev, R.; Yasuda, A.; Vossmeyer, T. *Langmuir* **2003,** *19*, 7754-7760.

15. Krasteva, N.; Besnard, I.; Guse, B.; Bauer, R. E.; Yasuda, A.; Vossmeyer, T. *Nano. Lett*. **2002,** *2*, 551-555.

16. Zamborini, F. A.; Leopold, M. C.; Hicks, J. F.; Kulesza, P. J.; Malik, M. A.; Murray, R. W. *J. Am. Chem. Soc.* **2002,** *124*, 8958-8964.

17. Murray, R. W. *Chem. Rev.* **2008,** *108,* 2688-2720.

18. Chen, S. *Langmuir* **2001,** *17,* 6664-6668.

19. Laaksonen, T.; Ruiz, V.; Murtomäki, L.; Quinn, B. M. *J. Am. Chem. Soc.* **2007,** *129,* 7732-7733.

20. Luo, J.; Kariuki, N.; Han, L.; Maye, M. M.; Moussa, L. W.; Kowalski, S. R.; Kirk, F. L.; Hepel, M.; Zhong, C.-J. *J. Phys. Chem. B* **2002,** *106,* 9313-9321.

21. Sih, B. C.; Teichert, A.; Wolf, M. C. *Chem. Mater.* **2004,** *16,* 2712-2718.

22. Buttry, D. A.; Ward, M. D. *Chem. Rev.* **1992,** *92,* 1355-1379.

23. Deakin, M. R.; Buttry, D. A. *Anal. Chem.* **1989,** *61,* 1147A-1154A.

24. Bruckenstein, S.; Jureviciute, R.; Hillman, A. R. *J. Electrochem. Soc.* **2003,** *150,* E285-291.

25. Jureviciute, I.; Bruckenstein, S.; Hillman, A. R. *Electrochim. Acta* **2006,** *51,* 2351-2357.

26. Bruckenstein, S.; Krtil, P.; Hillman, A. R. *J. Phys. Chem. B* **1998,** *102,* 4994-5003.

27. Hillman, A. R.; Bruckenstein, S. *J. Chem. Soc., Faraday Trans.* **1993,** *89,* 3779-3782.

28. Jackson, A.; Hillman, A. R.; Bruckenstein, S.; Jureviciute, I. *J. Electroanal. Chem.* **2002,** *524-525,* 90-102.

29. Hillman, A. R. *Solid State Ionics* **1997,** *94,* 151-160.

30. Brauer, G. *Handbook of Preparative Inorganic Chemistry;* Academic Press: New York, **1965**.

31. Bard, A. J.; Faulkner, L. R. *Electrochemical Methods*, 2nd ed.; Wiley: New York, **2001**.

32. Sauerbrey, G. *Z. Phys.* **1959,** *155,* 206-222.

33. Stiles, R. L.; Balasubramanian, R.; Feldberg, S. W.; Murray, R. W. *J. Am. Chem. Soc.* **2008,** *130,* 1856-1865.

34. Decher, G. *Science* **1997,** *29,* 1232-1237.

35. Song, C.; Wang, P.; Makse, H. A. *Nature* **2008,** *453,* 629–632.

36. *Impedance Spectroscopy: Theory, Experiment, and Applications,* 2nd ed.; Barosoukov, E.; MacDonald, J. R., Eds.; Wiley-Interscience: New York, **2005**.

37. Probability of Fc being oxidized at a given potential: Probability of Fc^+ = $1/(1+\exp(F/RT*(E-E^0))$.

38. Brug, G. J.; Van Den Eeden, A. L. G.; Sluyter-Rehbach, M.; Sluyters, J. H. *J. Electroanal. Chem.* **1984,** *176,* 275-295.

39. Feldberg, S. W. *J. Electroanal. Chem.* **2008,** *624,* 45-51.

40. Nelsen, S. F.; Chen, L.-J; Ramm, M. T.; Voy, G. T.; Accola, M. A.; Seehafer, T.; Sabelko, J.; Pladziewicz; J. R. *J. Org. Chem.* **1996,** *61*, 1405-1412.

41. Dahms, H. *J. Phys. Chem.* **1968,** *72,* 362-364.

42. Ruff, I.; Friedrich, V. *J. Phys. Chem.* **1971,** *75,* 3297-3302.

43. Majda, M. In *Molecular Design of Electrode Surfaces;* Murray, R. W., Ed.; John Wiley & Sons: New York, **1992**; 159−206.

44. Hillman, A. R.; Mohamoud, M. A. *Electrochim. Acta* **2006,** *51,* 6018-6024.

45. Hillman, A. R.; Mohamoud, M. A.; Bruckenstein, S. *Electroanal.* **2005,** *17,* 1421-1432.

46. Glide, A.; Cooper, J.; Hillman, A. R.; Bailey, L.; Jackson, A.; Webster, J. R. P. *Langmuir* **2003,** *19,* 7746-7753.

47. Hillman, A. R.; Daisley, S. J.; Bruckenstein, S. *Electrochim. Acta* **2008,** *53,* 3763-3771.

48. Daum, P.; Murray, R. W. *J. Phys. Chem.* **1981,** *85*, 389-396.

49. Abbott, N. L.; Whitesides, G. M. *Langmuir* **1994,** *10,* 1493-1497.

3.7 Appendix

DigiSim Parameters – These are the parameters for a 1 μm film at 50 mV/s with D = 4 x 10^{-7} cm^2/s.

source program: DigiSim for Windows 95
program version: 3.05
file type: CV

charge transfer reactions:
reaction[1]: A(0) + e = A(1)
reaction[2]: A(1) + e = A(2)
reaction[3]: A(2) + e = A(3)

experimental parameters:
Estart (V): 0
Eswitch (V): 0.8
Eend (V): 0
v (V/s): 0.05
temperature (K): 298.2
Ru (Ohms): 90
Cdl (F): 2E-005
cycles: 1
electrode geometry: planar
area (cm2): 1.37
diffusion: finite
thickness (cm): 0.0001
pre-equilibrium: enabled for all reactions

charge transfer parameters:
E0[1] (V): 0.35
alpha[1]: 0.5
ks[1] (cm/s): 1000
E0[2] (V): 0.355
alpha[2]: 0.5
ks[2] (cm/s): 1000
E0[3] (V): 0.36
alpha[3]: 0.5
ks[3] (cm/s): 1000

species parameters:
Canal[A(0)] (M/l): 0.04 (blocked right boundary)
Cinit[A(0)] (M/l): 1.2041E-019
D[A(0)] (cm2/s): 4.4E-007
Canal[A(1)] (M/l): 0.04 (blocked right boundary)

Cinit[A(1)] (M/l): 9.8947E-014
D[A(1)] (cm2/s): 4.4E-007
Canal[A(2)] (M/l): 0.04 (blocked right boundary)
Cinit[A(2)] (M/l): 9.8865E-008
D[A(2)] (cm2/s): 4.4E-007
Canal[A(3)] (M/l): 0 (blocked right boundary)
Cinit[A(3)] (M/l): 0.12
D[A(3)] (cm2/s): 4.4E-007

model parameters:
expanding space factor: 0.1
potential step (V): 0.0001
iterations: 1
noise_level (A): 0
D/k: 50
thickness/dx: 200
r0 minimum: 20

simulation statistics:
CPU-time: 2.468
maximum number of boxes: 48
model diffusion coefficient: 3197.1
total number of corrections: 0
number of potential steps with corrections: 0
Imin: -0.0016341
Imax: 0.001634
Cmax: 0.12

Chapter Four

Voltammetry and Redox Charge Storage Capacity of Ferrocene-Functionalized Silica Nanoparticles

4.1 Introduction

As methods of nanoparticle synthesis and characterization improve, their envisioned applications continue to gain interest. Nanoparticles can be designed for unique and optical, electronic, and magnetic properties, allowing a wide range of functionality. Our laboratory and others have contributed work on redox-active nanoparticles. These previous reports utilizing ferrocene functionalized gold monolayer protected clusters have focused on a variety of issues including synthesis and characterization,[1-7] kinetics of ligand exchange,[8] redox sensing,[9-11] and formation of nanoarchitectures[11-14]. Our recent report[15] on gold monolayer-protected clusters having 1.1 to 2.2 nm diameter cores and coated with full monolayers of thiolated ferrocenes show that these new materials offer substantial redox charge storage capacity, as much as 7×10^9 C m^{-3}, which arises from the combination of a dense surface coverage by ferrocene sites, and the very small nanoparticle dimensions. This discussion expands on that idea, using inexpensive and easily fabricated nanoparticle materials, with a study of silica nanoparticles bearing a full monolayer of attached ferrocenes and having overall 15 nm diameters (including the ferrocene layer).

Several combinations of silica nanoparticles with redox moieties have been previously described, but none thus far have demonstrated exhaustive, kinetically rapid reactions of the redox sites. Ferrocene-doped silica nanoparticles have been proposed as electron transfer mediators for glucose determination, in one case entrapping the ferrocene within 15 nm diameter silica nanoparticles[16] and in the other amide-linking it to the surfaces of 80 nm nanoparticles.[17] Ling et al.[18] prepared 60 nm diameter ferrocenyl-functionalized silica nanoparticles, aiming at improving guest-host interactions with β-CD coated nanoparticles. These nanoparticles had a low ferrocene (10-15%) coverage, and their solution dispersions exhibited sluggish electron transfer (large ΔE_{PEAK}) in cyclic voltammetry, and mixed diffusion-adsorption behavior. Budny et al.[19] functionalized large (140 to 735 nm diameter) nanoparticles with various redox-active species and, although surface coverages were higher (*ca*. 50% in the case of ferrocene), the ferrocenes were incompletely redox-active. A similar result was reported by Plumeré and Speiser,[20] who used hydrosilanization to covalently attach ferrocene to 200 nm diameter particles. These previous incomplete reactivity outcomes are possibly a result of the large nanoparticle dimensions, as we discuss later. Xu and Aoki[21] described vinylferrocene-immobilized polystyrene latex particles of various sizes, where only those Fc groups within ~70 nm of the electrode were thought to be electroactive.

Finally, two other recent reports have described freely diffusing redox-active silica nanoparticles, but lacking fully reversible electrochemistry. Jiang et al.[22] report that silver nanoparticles on 200 nm silica nanoparticle surfaces could migrate to the working electrode surface. Sun et al.[23] used 12 nm lithium modified silica nanoparticles as a lithium cation source to prepare lithium conductive gel electrolytes; these nanoparticles

were freely diffusing but so were the lithium ions, which moved freely between electrode and nanoparticles during voltammetry.

The aim of the present study was to prepare full redox monolayers on very small silica nanoparticles by straightforward synthetic means, to achieve a complete analytical characterization of surface coverage, and to demonstrate a fully reactive redox layer—with an eye on potential usefulness in redox-based supercapacitors (charge storage devices).[24-26] In the latter light, it was important to attain a reasonable level of nanoparticle solubility and well-behaved, reversible ferrocene voltammetry. Complete reactivity of siloxane-attached ferrocene sites on 15 nm diameter silica nanoparticles (abbrev. $FcSiO_2$) was attained, at what was estimated to be a complete ferrocene monolayer coverage of *ca*. 600 ± 24 Fc per nanoparticle. The coverage was determined by three different measurement procedures. Well-behaved voltammetry was accessible in both dilute methanol solutions and in concentrated slurries in acetonitrile. This is the first report of diffusion-controlled voltammetry of fully reactive ferrocene-labeled silica nanoparticles devoid of any substantial adsorption effects. This is also a proof-of-concept of redox functionalization of silica nanoparticles as potential charge storage media.

4.2 Experimental

Chemicals. (3-Aminopropyl)trimethoxysilane (APTMS), ferrocenecarboxylic acid, N-(3-dimethylaminopropyl)-N'-ethylcarbodiimide hydrochloride (EDAC), tetrabuylammonium perchlorate (Bu_4NClO_4), $Cu(II)(ClO_4)\cdot 6H_2O$, were obtained from Aldrich and used as received. Organosilicasol MT-ST silica particles in MeOH were purchased from Nissan

Chemical Corp. (Houston, TX). Toluene (ACS grade), acetonitrile (ACS grade), dimethylformamide (DMF, Optima) was obtained from Fisher and used as received.

Instrumentation. ^{1}H NMR spectra were collected on a Varian AMX300. ^{29}Si NMR spectra were collected on a Varian AMX360 using CP/MAS at a spin rate of 10 kHz. XPS spectra were collected on a Kratos Axis Ultra^{DLD} with an Al Kα 1486.6 eV source. Electrochemistry was performed using a standard three-electrode cell interfaced to a CH Instruments CH660A potentiostat, using solutions of methanol, acetonitrile, and Bu_4NClO_4 electrolyte (electrochemical grade). TEM images were acquired on a Philips (FEI) CM12, operating at 100 kV. Digital images were collected with a Gatan camera system. Centrifugation was performed using an Eppendorf 5810 centrifuge with a fixed-angle rotor at 6000 rpm for 15 minutes.

Synthesis of N-(3-(trimethoxysilyl)propyl)ferrocene.[19] To a solution of ferrocenecarboxylic acid in CH_2Cl_2 (1.0 g, 4.3 mmol) was added 0.98 g (5.1 mmol) of EDAC. The solution was sonicated for 10 minutes followed by the addition of (3-aminopropyl)trimethoxysilane (0.67 g, 3.7 mmol). The solution was then stirred for four hours. The product was purified by filtration through Celite to remove by-products, followed by column chromatography over silica gel using 12/88 vol:vol CH_2Cl_2/acetone as eluent. 1H NMR (300 MHz, CD_2Cl_2) δ (ppm): 5.95 (broad s, 1H, NH), 4.64 (t, 2H, Fc), 4.35 (t, 2H, Fc), 4.21 (s, 5H, Fc), 3.57 (s, 9H, OCH_3), 3.34 (q, 2H, $NHCH_2$), 1.69 (m, 2H, CH_2), 0.71 (t, 2H, $SiCH_2$).

Preparation of Ferrocene-Functionalized Silica Nanoparticles, $FcSiO_2$.[27] 3 g of MT-ST silica particles were precipitated from MeOH (the purchased solution in which they were

delivered) by adding toluene. Particles were washed four times by centrifugation followed by redispersion in toluene. 300 mg of N-(3-(trimethoxysilyl)propyl)ferrocene in 10 mL toluene was added to the MT-ST silica particles in toluene followed by heating at 80 °C for 18 hours. The nanoparticles were then washed four times by centrifugation and redispersion in toluene, and then four times with methanol and left dispersed in methanol for experimental use. We have seen no visual evidence of hydrolytic cleavage loss of ferrocenes from the nanoparticles; the solvent layer is colorless after centrifuging the nanoparticles out of solution, including following electrochemical studies.

TEM of $FcSiO_2$. Particles were dropcast from dilute solutions onto a 200 mesh copper grid with a Formvar Carbon support film (Electron Microscopy Sciences, Hatfield, PA).

4.3 Results and Discussion

Nanoparticle phase behavior. The solubilities of the silica nanoparticles as received in methanol solution *vs*. after ferrocene functionalization are different and display novel characteristics in the latter case. The slightly opaque dispersion of the as-received nanoparticles in methanol is quite stable, although the nanoparticles can be centrifuged into a compact layer. Addition of toluene to the methanol dispersion causes precipitation as a gel, which is incompletely dispersed by shaking; large agglomerates remain and the toluene phase is more opaque than the original methanol solution. TEM (see Figure 4.1) revealed that the ~13 nm diameter silica nanoparticles in such agglomerates remain intact as discrete entities.

Following ferrocene-functionalization, the orange-colored nanoparticles (abbrev. $FcSiO_2$), now ~15 nm (~13 nm core plus ~2 nm ligand shell), are readily dispersed as a cloudy phase in polar organic solvents like methanol, ethanol, and DMF. The cloudiness may reflect scattering caused by some larger nanoparticle agglomerates; over days these slowly settle out, especially at functionalized nanoparticle concentrations higher than ~15 μM in methanol (MM = $1.75x10^6$ g/mol is used to estimate molar concentrations.[28])

When a supporting electrolyte (for voltammetry), typically 0.1 M $LiClO_4$, is added to a $FcSiO_2$ dispersion in methanol, the nanoparticles settle out (over a period of hours) into a separate, cloudy layer, leaving a clear solvent/supporting electrolyte layer above. The nanoparticle concentrations in the separated layer could be as high as *ca.* 60 μM, and the clear solvent layer above can be removed without evident consequence to the nanoparticle-containing phase. The latter is stable and is not a gel or aggregate. From its sensitivity to the presence of electrolyte (which would screen electrostatic repulsions), we infer that the nanoparticle solvent layer's stability is electrostatically based, probably due to residual silanols that give the silica nanoparticles an inherent negative charge.[29] We will arbitrarily refer to the nanoparticle phase (or layer) as a "slurry". We estimate that the average edge-edge spacing of the nanoparticles in a stable 60 μM $FcSiO_2$ slurry is *ca.* 55 nm. Formation of a $FcSiO_2$ slurry phase can also be provoked by addition of cosolvents. For example, adding acetonitrile to a >15 μM $FcSiO_2$ solution in methanol can cause prompt formation of an opaque nanoparticle slurry layer, leaving a clear solution phase above. Addition of acetonitrile to a more dilute, 5 μM $FcSiO_2$ solution in methanol did not cause formation of a slurry layer, at acetonitrile/methanol ratios as high as 3/1. Adding Bu_4NClO_4 electrolyte in acetonitrile at concentrations >10 mM to a 5 μM $FcSiO_2$ dispersion in an

Figure 4.1. TEM image of intact nanoparticles in agglomerate after the addition of toluene to the methanol solution of as-received nanoparticles.

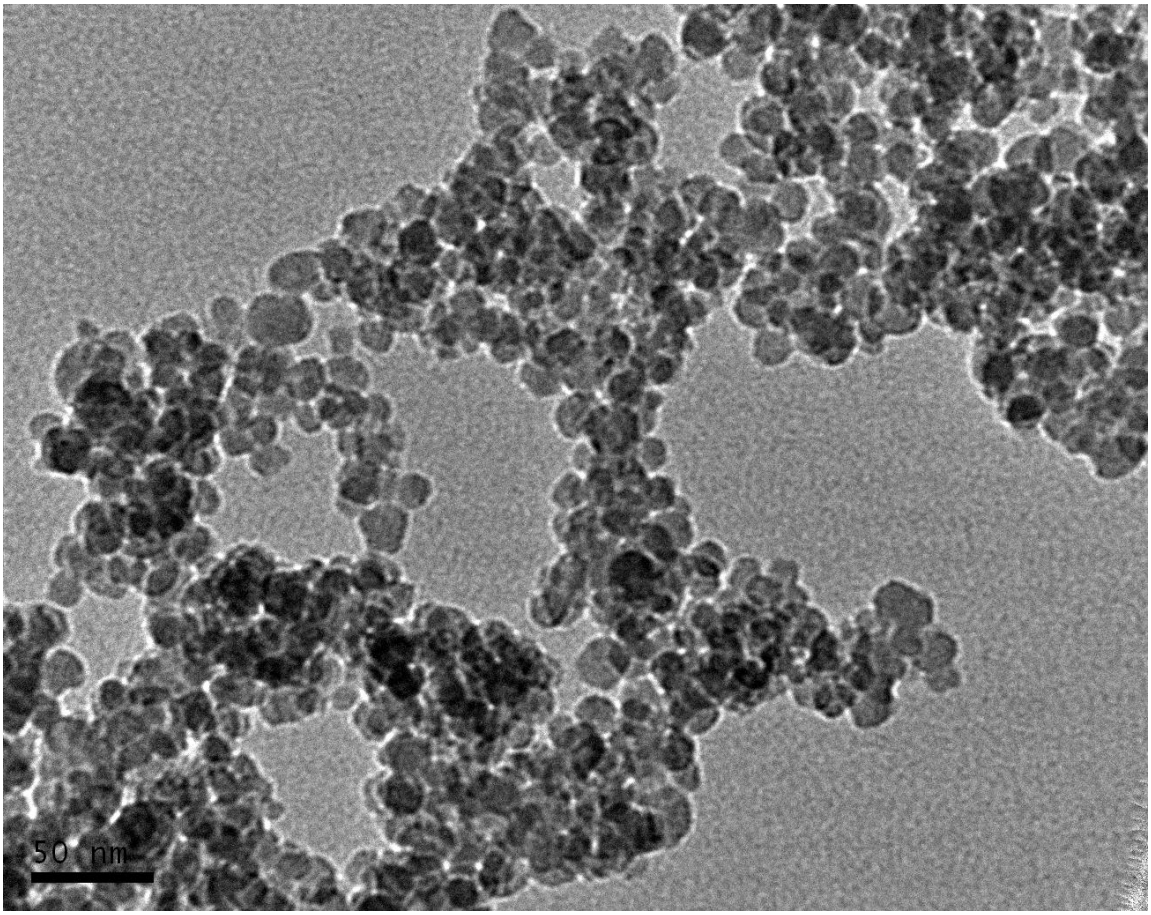
50 nm

equal volume of methanol caused formation of a nanoparticle slurry layer. The volume of the slurry layer formed was approximately the same as the volume of the methanol solution prior to the addition of acetonitrile and supporting electrolyte.

While the cause(s) of the nanoparticle slurry layer formation were not explicitly studied, the phenomenon was useful in making available different forms of ferrocenated silica nanoparticle dispersions for voltammetric investigation.

^{29}Si NMR. ^{29}Si NMR spectra of nanoparticles before and after functionalization (Figure 4.2) are consistent with covalent attachment of the ferrocene ligand, according to the general reaction

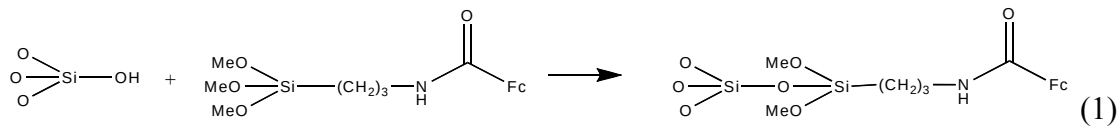

(1)

Prior to functionalization (Figure 4.2, curve a), resonances reflecting non-surface (bulk) silicon (Q^4 band) and silicon bonded to OH groups (Q^3 and Q^2 bands) are present. After functionalization (Figure 4.2, curve b), the Q^4/Q^3 and Q^4/Q^2 peak intensity ratios increased, as expected for consumption of nanoparticle surface silanol groups by binding of the ferrocene ligand. New peaks appear at chemical shifts expected for the ferrocene reagent, containing silicon bonded to both carbon and oxygen (T^3, T^2 and T^1 bands). The residual $Si(OCH_3)$ groups (T^2 and T^1 bands) are presumed to become hydrolyzed with subsequent handling of the nanoparticles. The peak assignments are based on literature chemical shift data.[30]

Nanoparticle surface coverage of the ferrocene reagent. X-ray photoelectron spectroscopy was used to assess the overall atomic composition of films of $FcSiO_2$

Figure 4.2. ^{29}Si NMR of Silica nanoparticles before (a) and after functionalization (b) (see text). Assignments based on literature chemical shift values (Ref. 30).

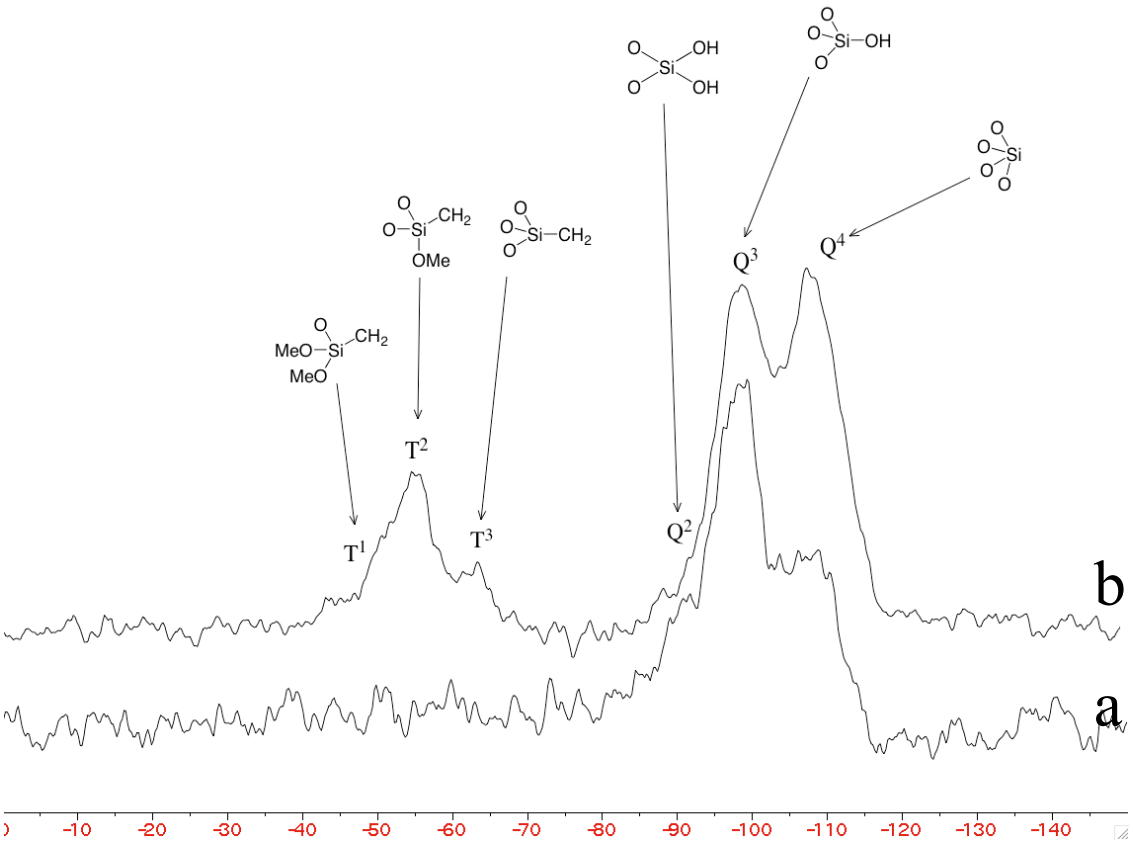
T1
T2
T3
Q2
Q3
Q4
b
a
-10
-20
-30
-40
-50
-60
-70
-80
-90
-100
-110
-120
-130
-140

Table 4.1. XPS data for elemental composition of $FcSiO_2$ nanoparticles

Element	% Atomic Composition
C	25.9
N	1.8
Fe	2.0
Si	22.5
O	47.9

Each concentration was calculated using the following equation:[32]

$$C_x = \frac{I_x / S_x}{\sum_i I_i / S_i}$$

where S is the atomic sensitivity factor, and I is the peak area.

nanoparticles cast on ITO glass slides. ITO coated glass slides were used to avoid interfering Si 2p peaks of glass, and to minimize charging effects. Nanoparticle atomic percentages are given in Table 4.1. The results for %Fe yield an estimate of *ca.* 630 ferrocene sites per nanoparticle. In a grafting study on silica particles, Harrak et al.[31] report that approximate monolayer coverage corresponds to reaction of one silane modifier per nm^2. The $FcSiO_2$ XPS result, and the surface area (520 nm^2) of a 13 nm diameter sphere (core), amounts to binding of slightly more (20%) than one ferrocene silane per nm^2. The experimental objective of a complete monolayer coverage in Reaction (1) appears to have been satisfactorily achieved. The possibly above-monolayer coverage indicated could reflect a minor amount of siloxane oligomerization of the ferrocene reagent on the nanoparticle surface.

A potentiometric titration gave a second and more direct measure of the average number of ferrocenes per $FcSiO_2$ nanoparticle (Figure 4.3). $Cu(II)(ClO_4)_2$ has been previously used for the titrimetric determination of ferrocene derivatives.[33] From the equivalence point, the total number of ferrocenes per silica nanoparticle was determined to be 590, in good agreement with the XPS result above. Though the presence of a single end point suggests that the ferrocene groups exhibit a single redox potential, previous work on redox polymers has shown that the sites on poly-redox substances should exhibit a statistical distribution of formal potentials provided that they react independently and serially.[34] This point will be discussed in the following section.

Voltammetry of $FcSiO_2$ nanoparticles. As noted above, a 60 μM solution of $FcSiO_2$ in methanol containing electrolyte (0.1 M $LiClO_4$) forms an opaque "slurry" nanoparticle phase. Cyclic voltammetry (Figure 4.4, curves B,C) in this phase reveals typical ferrocene behavior

Figure 4.3. Potentiometric titration of 10 μM $FcSiO_2$ with $Cu(ClO_4)_2$ in 0.1 M Bu_4NClO_4/methanol.

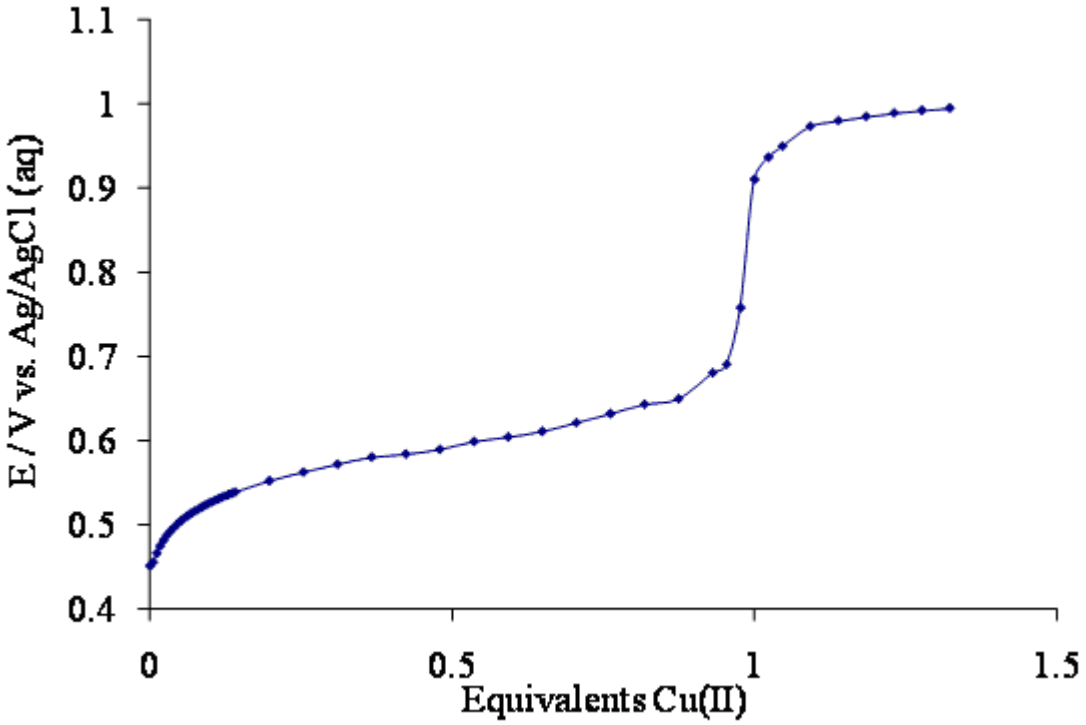
1.1
1
0.9
0.8
0.7
0.6
0.5
0.4
E / V vs. Ag/AgCl (aq)
0
0.5
1
1.5
Equivalents Cu(II)

Figure 4.4. Cyclic voltammetry of 60 μM $FcSiO_2$ in methanol (0.1 M $LiClO_4$). A: 20 mV/s, B: 400 mV/s, C: 3200 mV/s. The dashed vertical line represents the E°' for $FcSiO_2$. Positive-going potential scans initiated at the right.

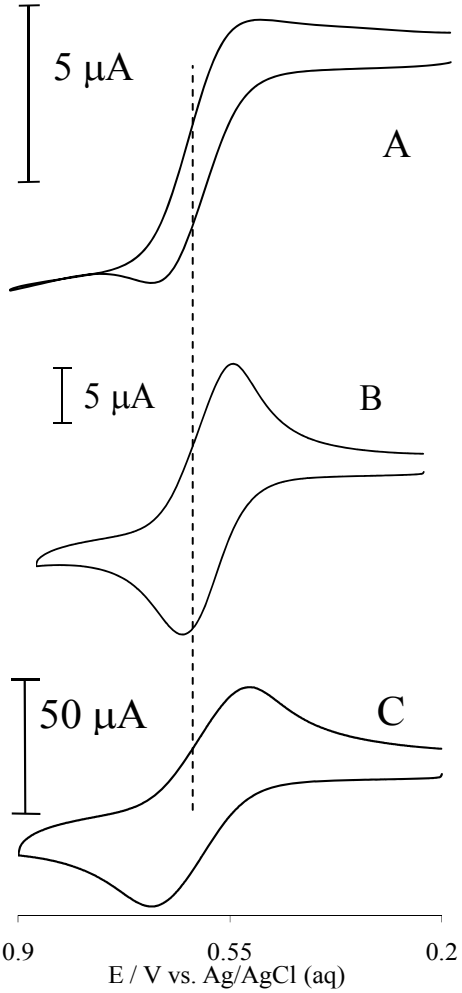
5 μA
A
5 μA
B
50 μA
C
0.9
0.55
0.2
E / V vs. Ag/AgCl (aq)

Figure 4.5. Plot of oxidation peak current (i_p) vs square root of potential scan rate for $FcSiO_2$ in methanol (triangles, $R^2 = 0.998$; $y = 1.66x10^{-5} + 1.82x10^{-5}$ x ; squares, $R^2 = 0.995$; $y = 2.24x10^{-5}$ x) and methanol /acetonitrile slurry (circles, $R^2 = 0.999$; $y = 1.36x10^{-5}$ x).

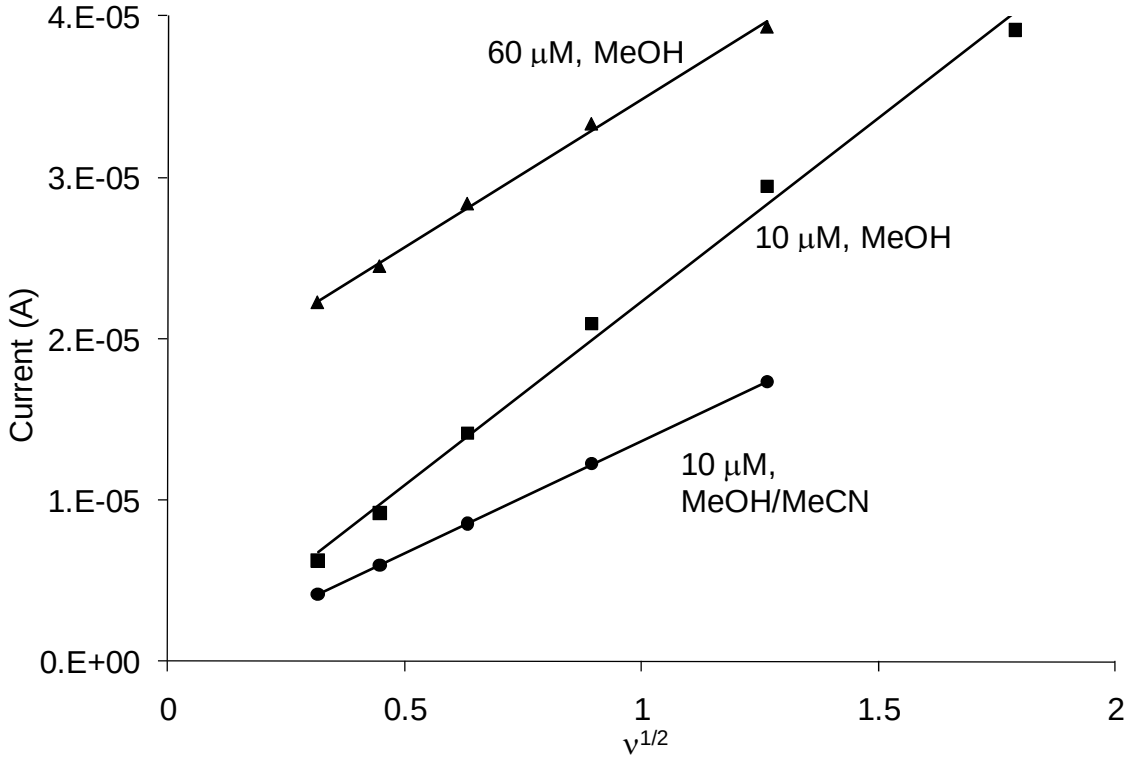
4.E-05
3.E-05
2.E-05
1.E-05
0.E+00
Current (A)
0
0.5
1
1.5
2
ν1/2
60 μM, MeOH
10 μM, MeOH
10 μM,
MeOH/MeCN

—a one-electron, chemically reversible wave with formal potential at 0.60 V vs. Ag/AgCl (aq). The wave shows no sign of splitting, indicating a relatively uniform environment for the ferrocene sites. Results at higher potential scan rates (curves B,C) show that the oxidation peak current is proportional to the square root of the potential scan rate, indicating control of currents by linear diffusion of nanoparticles (Figure 4.5, upper curve). However, the convective transport at slower scan rates (vide infra) in the 60 μM slurry and the large charging current background under the peak currents at higher scan rates result in a non-zero y-intercept. Therefore, the solution was diluted to 10 μM $FcSiO_2$ using methanol (0.1 M $LiClO_4$). The peak currents in the now well-behaved cyclic voltammograms (not shown) for the 10 μM $FcSiO_2$ are proportional to the square root of the potential scan rate (Figure 4.5, middle curve) and are expressed (ideally) by the equation

$$i_p = 2.69 \times 10^5 n^{3/2} A D^{1/2} C v^{1/2} \qquad (2)$$

where n is the number of electrons delivered (per ferrocene) by a diffusing species having diffusion coefficient D and net ferrocene concentration C (mol cm^{-3}; the product of nanoparticle concentration and the number of ferrocenes per $FcSiO_2$), and v is potential scan rate. The values of D and C are treated as nominal unknowns. The value of the nanoparticle D was estimated from the Stokes-Einstein equation as 5×10^{-7} cm^2 sec^{-1}, based on a hydrodynamic radius of 7.5 nm and methanol viscosity of 0.59 cP:

$$D = \frac{kT}{6\pi\eta r} \qquad (3)$$

Using this value of D, we calculate that C = 5.85×10^{-6} mol cm^{-3} in the slurry and consequently that there is an average of 585 ferrocenes per silica nanoparticle. Not-

withstanding the approximation inherent in the use of a pure solvent viscosity in Eqn. (3), the agreement with the XPS and potentiometric results provides strong confirmation that the ferrocene sites on the $FcSiO_2$ nanoparticles are fully reactive on the nanoparticle diffusion-controlled voltammetric timescale.

The single voltammetric wave in Figure 4.4 does not mean that all of the ferrocenes on the nanoparticle actually have the same formal potential. Based on previous analyses of poly-redox species (redox polymers, including polyvinylferrocene), it is rather expected that there is a statistical distribution of ferrocene site formal potentials, around the nominal formal potential inferred from the Figure 4.4 voltammetry.[34] A single, one electron waveshape is nonetheless expected provided that the multiple redox sites are non-interacting and react independently, which seems to be the case for the $FcSiO_2$ sites. This result has previously been observed in other analogous systems where molecules contain a number of non-interacting redox centers that react independently and serially.[1-3,35-37]

At slow potential scan rates (<0.1 V s^{-1}) in the methanol slurry of Figure 4.4 (Curve A), the voltammetry develops a pseudo-steady-state waveshape. The 1.6 mm diameter working electrode is much too large to anticipate any radial diffusion effects on waveshape. We interpret the aberrant voltammetric behavior at slow potential scan rates as convective transport caused by density gradients in the near-electrode solution, due to production of large, localized (on the nanoparticles) concentrations of ferrocenium species and their necessary counterions. Such density gradient-convective effects are well-known in analogous circumstances.[38,39]

Figure 4.6. Cyclic voltammetry of 10 μM $FcSiO_2$ in methanol / acetonitrile (1:1 vol:vol, 0.1 M Bu_4NClO_4), 0.1 V s^{-1}.

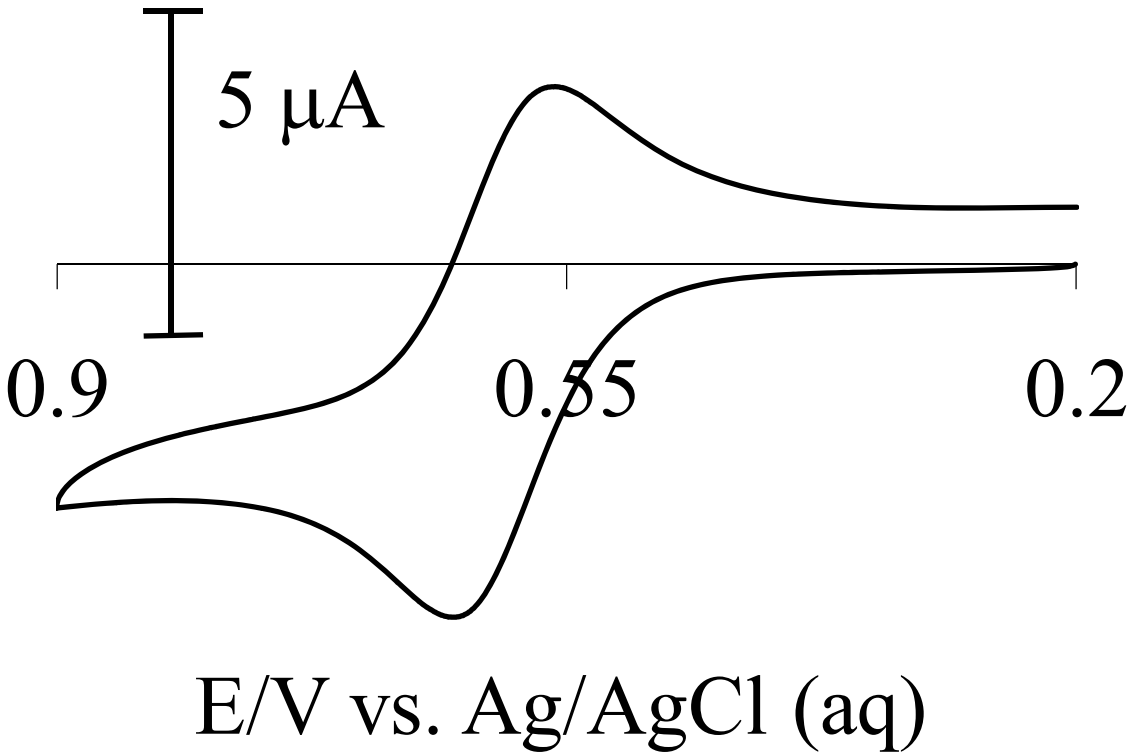
5 μA
0.9
0.55
0.2
E/V vs. Ag/AgCl (aq)

As noted above, dilute methanol dispersions of $FeSiO_2$ nanoparticles are stable with little evidence of settling. However, if an equal volume of acetonitrile containing 0.1 M Bu_4NClO_4 electrolyte is added to a 10 μM solution of $FcSiO_2$ in methanol, the nanoparticles fairly promptly settle into a translucent slurry layer, with a clear layer of solvent above. The volume of the nanoparticle slurry layer formed is approximately the same as the volume of the original methanol solution, and the concentration of $FcSiO_2$ nanoparticles in the slurry layer remains as 10 μM. (Cyclic voltammetry with the electrodes in the clear solvent layer reveals only background current.) Placing the working electrode into the slurry layer gives a well-defined wave attributed to ferrocene sites on $FcSiO_2$ nanoparticles (Figure 4.6). Varying the scan rate (Figure 4.5, lower curve) shows that the peak current is again proportional to the square root of the scan rate, an indication of diffusion-limited currents. The peak potential separation in Figure 2.6 is ΔE_{PEAK} = 69 mV, larger than the reversible 59 mV value. This is a minor uncompensated resistance effect; a plot of ΔE_{PEAK} versus $\nu^{1/2}$ is linear with a $\nu = 0$ intercept of 62 mV, close to the reversible expectation for ferrocene. As mentioned above, others have reported that not all of the redox groups immobilized on redox-active silica nanoparticles were electroactive[20] or exhibited sluggish electron transfers and mixed diffusion-adsorption voltammetry[18]. The present nanoparticles clearly differ in these respects.

An interesting issue in electrochemical reactions of redox-coated nanoparticles with non-conductive cores (as in $FcSiO_2$) is how all of the redox sites become electrochemically consumed. A requirement would seem to be nanoparticle rotational diffusion time constants that exceed the nanoparticle diffusion residence time at the electrode.[3] The rotational time constant can be estimated as $\tau_{rot} \sim 0.25$ μs, from the Debye theory of rotational diffusion

$$\tau_{rot} = \frac{V_{NP}\eta}{kT} \quad (4)$$

where V_{NP} is the nanoparticle volume. This value is much smaller than the 18 μsec diffusional residence time near the electrode, estimated from

$$l = \sqrt{2Dt} \quad (5)$$

assuming a diffusion path-length of twice the particle diameter (e.g., once in and out) and D = 5 x 10^{-7} cm^2 sec^{-1}.

One other possible scenario for how the redox sites all react is the process of electron hopping (i.e., electron "diffusion") along the surface of the particle, i.e.. The time required for an electron to half-circumnavigate a particle is given by,

$$\tau_E = \frac{2D_E}{L^2} \quad (6)$$

where L is the half-circumference and D_E is the electron diffusion coefficient. Taking 2.3 x 10^{-6} cm for L, and D_E as 7 x 10^{-8} cm^2 s^{-1},[3] predicts an electron hopping time constant of 40 μsec, which is significantly longer than the rotational time constant of 0.25 μsec. We conclude—as we did earlier[3] in discussing ferrocenated Au nanoparticles—that all of the ferrocene sites on the $FcSiO_2$ nanoparticles studied here should, during their reactions, be most rapidly accessible to the electrode by the process of rotational diffusion.

The above discussion emphasizes the probable importance of nanoparticle size in designing redox-coated nanoparticles to exhibit full reactivity of their surface redox

constituents. Note that nanoparticle volume V_{NP} varies as the cube of nanoparticle radius. Thus, a 75 nm nanoparticle radius would correspond to $\tau_{rot} \sim 250$ μsec which for D = 1 x 10^{-7} cm^2 sec^{-1} would almost surely yield limitations in adequate electrode/ferrocene contacts for exhaustive reaction. This effect may have been operative in the incomplete reactivities observed in past studies using larger SiO_2 nanoparticles.

While the voltammetry in Figure 4.6 is well behaved, the currents for the $FcSiO_2$ nanoparticles in the methanol/acetonitrile slurry layer are smaller (factor of 1.6, Figure 4.5, lower curve) than those for the same concentration of $FcSiO_2$ nanoparticles dispersed in methanol alone (Figure 4.5, middle curve). It would be expected, given the lower viscosity of the added acetonitrile, that currents (and D) would increase, not decrease, in the methanol/acetonitrile mixture (assuming that all of the Fc sites remain accessible).

We subsequently determined that the above discrepancy occurs by a slight settling of the $FcSiO_2$ nanoparticles just below the (down-facing) electrode (gravitationally or for some other reason), reducing the effective nanoparticle concentration and ferrocene flux to the electrode during voltammetry. Indeed, if the working electrode is allowed to remain immersed (undisturbed) in the slurry layer overnight, an ensuing voltammogram showed no ferrocene voltammetry and a resistive solvent (Figure 4.7). The apparent solution resistance (calculated from the slope of the current-potential curve) was *ca*. 10 MΩ. Thus, neither electrolyte or ferrocene-bearing nanoparticles are present in a thin layer of solvent directly under the electrode. This layer could not be visually seen owing to the opacity of the slurry layer. In contrast, if the working electrode was upward-facing (a simple folded-over Pt flag) during an overnight immersion in the nanoparticle slurry layer, a subsequent voltammogram (Figure 4.8) clearly displays the ferrocene oxidation wave. The wave is distorted, at least in

Figure 4.7. Cyclic voltammogram of $FcSiO_2$ in MeOH/MeCN (0.1 M Bu_4NClO_4) after electrode is left immersed in slurry overnight. 0.1 V/s.

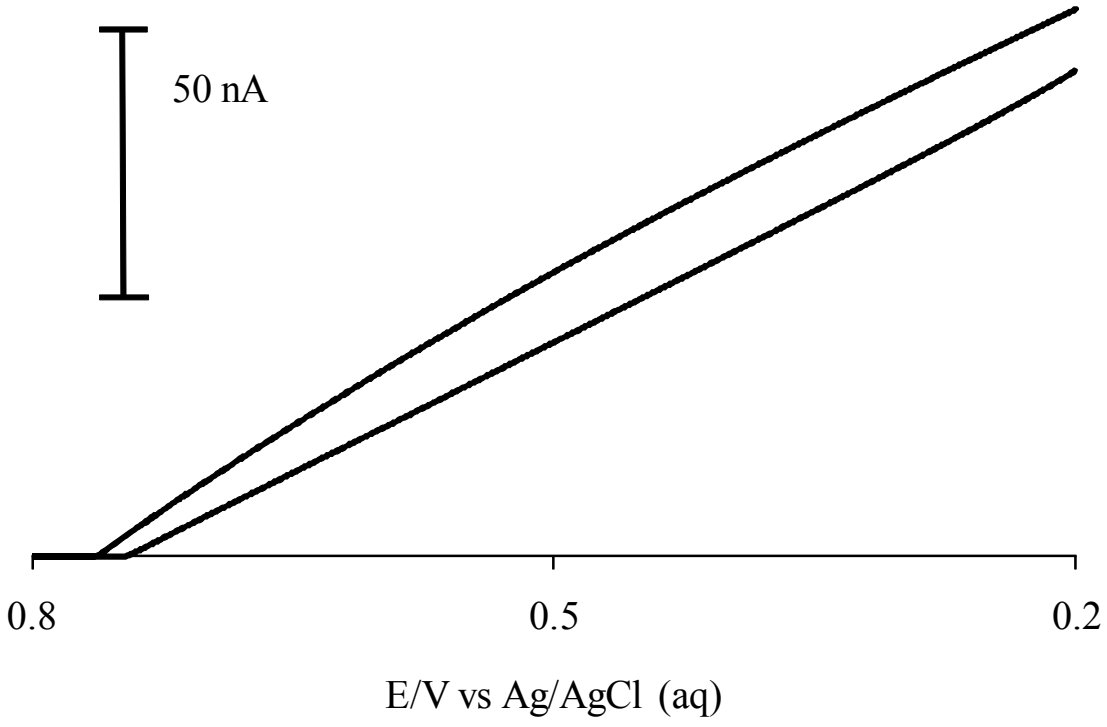
50 nA
0.8
0.5
0.2
E/V vs Ag/AgCl (aq)

Figure 4.8. Cyclic voltammogram of inverted flag electrode placed in 10 μM $FcSiO_2$ in methanol / acetonitrile (0.1 M Bu_4NClO_4), 0.1 V s^{-1}.

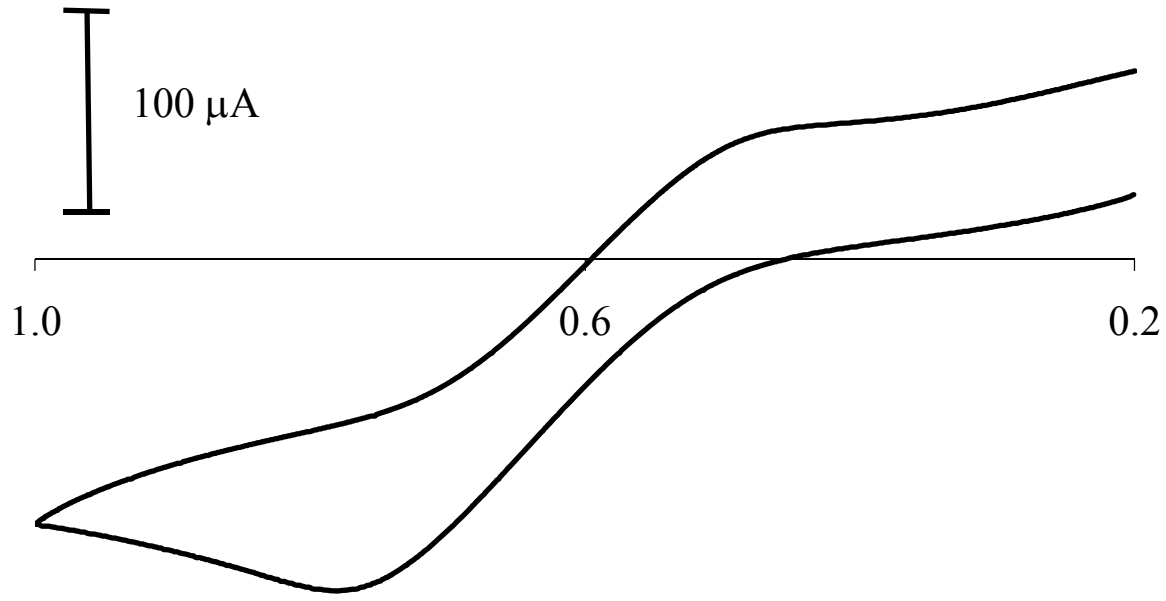
100 μA
1.0
0.6
0.2
E/V vs Ag/AgCl (aq)

part owing to the large currents attendant to the large area of the Pt flag electrode, and possibly some compaction of settled $FcSiO_2$ nanoparticles. No attempt was made to analyze the Figure 4.8 distortions in further detail.

The large resistance of the thin film of solution accumulated over time under a downward-facing electrode suggests that the inferred settling of the $FcSiO_2$ nanoparticles causes a sequestering of the electrolyte from this thin solution layer. Interactions between electrolyte ions and nanoparticle surfaces, when the nanoparticles seem marginally soluble as in this case, are an unfamiliar subject. The actual quantity of electrolyte sequestered from the thin solvent film must be quite small, since analysis of the solvent and electrolyte concentrations in the clear solvent layer above the nanoparticle slurry layer (formed when 0.2 M Bu_4NClO_4/acetonitrile is added to an equal volume of 10 μM $FcSiO_2$ in methanol), was still ~0.1 M. This was determined by evaporating a known volume of the clear layer and weighing the supporting electrolyte that it contained. The clear solvent layer contained, as determined by NMR, a 0.8:1 molar ratio, ~45:55 vol:vol, of acetonitrile/methanol, so the slurry phase is slightly enriched in acetonitrile.

Hydrodynamic voltammetry of $FcSiO_2$. Because of the large nanoparticle surface area/volume ratio, the ferrocene-coated silica nanoparticles contain up to 5 x 10^7 C m^{-3} of redox charge as a dry phase, and 6 x 10^5 C m^{-3} in a concentrated (60 μM) slurry.[40] Extraction of the large electrochemical charge from a nanoparticle slurry phase, were the slurry to be deployed as a supercapacitor element, is a challenging issue. Diffusion of the nanoparticles is relatively slow. Rotated-disk voltammetry (up to 7500 rpm) was tested in the concentrated $FcSiO_2$ nanoparticle slurry phase; while ferrocene currents were seen, the wave was very drawn out and a current plateau was not reached.

A more extreme form of hydrodynamic mass transport was tested by subjecting a 9 μM dispersion of $FcSiO_2$ in 0.1 M $LiClO_4$/methanol to sonication. The use of sonication to achieve fast hydrodynamic transport to electrodes is well documented.[41-43] With the cell placed in a sonication bath, with electrodes in the nanoparticle slurry phase, a scan of electrode potential produced the noisy voltammogram in Figure 4.9. The limiting current of *ca*. 40 μA corresponds to an effective diffusion transport layer thickness of 1.2 μm, calculated from

$$i_{\lim} = \frac{nFADC}{\delta} \qquad (7)$$

where A is electrode area, D the diffusion coefficient of the nanoparticles in methanol (5 x 10^{-7} cm^2 sec^{-1}), and C is the concentration of Fc sites. This transport layer thickness is equivalent to a rotated disk electrode rotation rate, ω, of $1.4x10^5$ rpm, using the equation,

$$\delta = 1.61 D^{1/3} \omega^{-1/2} \upsilon^{1/6} \qquad (8)$$

where υ is kinematic viscosity. This high apparent rate of mass transport may have some usefulness in supercapacitor discharge.

4.4 Conclusions

Silica nanoparticles containing a full monolayer of ferrocene, covalently bound through siloxane coupling have been prepared. The total number of ferrocenes per particle are 630, 585, and 590, as determined by XPS, cyclic voltammetry, and potentiometric titration, respectively. These particles also exhibit interesting behavior of settling into a slurry phase,

Figure 4.9. Cyclic voltammetry of a sonicated solution of 9 μM $FcSiO_2$ in methanol (0.1 M $LiClO_4$). The dashed line estimates the limiting current.

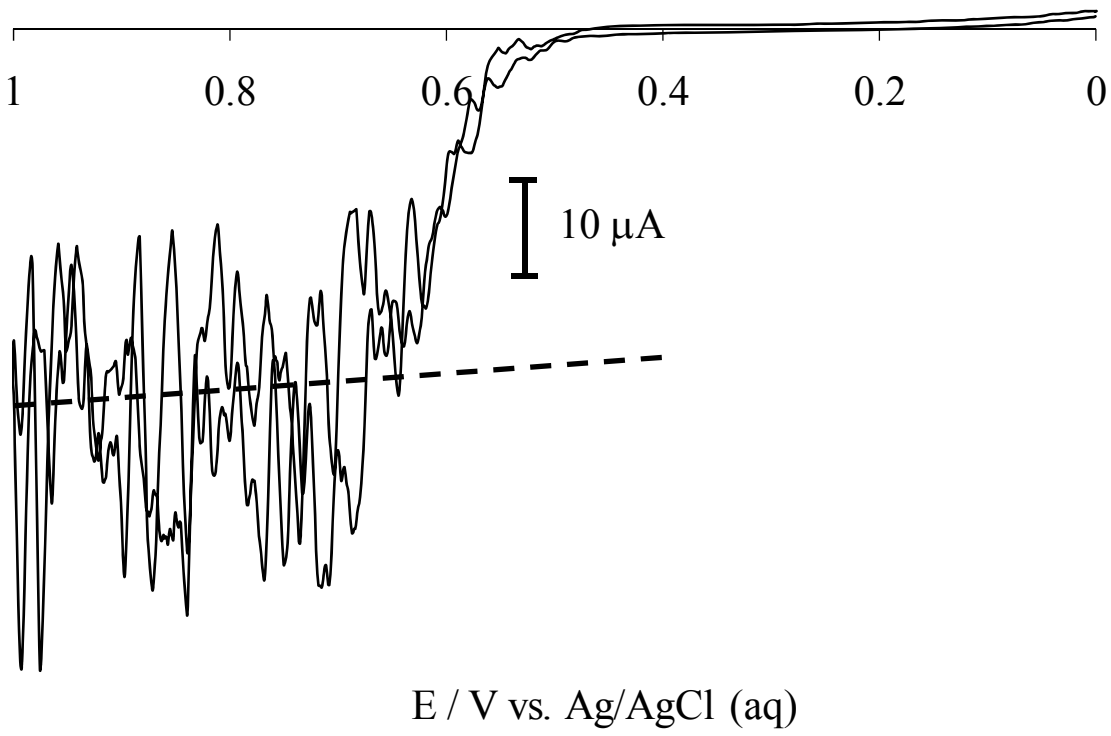
1
0.8
0.6
0.4
0.2
0
10 μA
E / V vs. Ag/AgCl (aq)

yet still yielding typical solution electrochemistry results. All ferrocenes are electrochemically accessible and non-interacting. The redox-coated nanoparticles containing a substantial electrochemical charge, amounting as a dry phase to 5 x 10^7 C m^{-3} and to 6 x 10^5 C m^{-3} in a concentrated slurry.[40]

4.5 Acknowledgements

This research was supported in part by grants from the Office of Naval Research and the National Science Foundation.

4.6 References

1. Hostetler, M. J.; Green, S. J.; Stokes, J. J.; Murray. R. W. *J. Am. Chem. Soc.* **1996,** *118,* 4212-4213.

2. Green, S. J.; Stokes, J. J.; Hostetler, M. J.; Pietron, J.; Murray, R. W. *J. Phys. Chem. B* **1997,** *101,* 2663-2668.

3. Green, S. J.; Pietron, J. J.; Stokes, J. J.; Hostetler, M. J.; Vu, H.; Wuelfing, W. P.; Murray, R. W. *Langmuir,* **1998,** *14,* 5612-5619.

4. Qu, X.; Peng, Z.; Jiang, X.; Dong, S. *Langmuir* **2004,** *20,* 2519-2522.

5. Liu, J.; Xu, R.; Kaifer, A. E. *Langmuir* **1998,** *14,* 7337-7339.

6. Rucareanu, S.; Gandubert, V. J.; Lennox, R. B. *Chem. Mater*. **2006,** *18,* 4674-4680.

7. Li, D.; Zhan, Y.; Jiang, J.; Li, J. *J. Colloid Interface Sci.* **2003,** *264,* 109-113.

8. Hostetler, M. J.; Templeton, A. C.; Murray, R. W. *Langmuir* **1999,** *15,* 3782-3789.

9. Wang, J.; Li, J.; Baca, A. J.; Hu, J.; Zhou, F.; Yan, W.; Pang, D.-W. *Anal. Chem.* **2003,** *75,* 3941-3945.

10. Daniel, M.-C.; Ruiz, J.; Nlate, S.; Blais, J.-C.; Astruc, D. *J. Am. Chem. Soc.* **2003,** *125,* 2617-2628.

11. Labande, A.; Ruiz, J.; Astruc, D. *J. Am. Chem. Soc.* **2002,** *124,*1782-1789.

12. Chen, S. W. *Langmuir,* **2001,** *17,* 6664-6668.

13. Peng, Z.; Qu, X.; Dong, S. *Langmuir* **2004,** *20,* 5-10.

14. Stiles, R. L.; Balasubramanian, R.; Feldberg, S. W.; Murray, R. W. *J. Am. Chem. Soc.* **2008,** *130,* 1856-1865.

15. Wolfe, R. L.; Balasubramanian, R.; Tracy, J. B.; Murray, R. W. *Langmuir* **2007,** *23,* 2247-2254.

16. Zhang, F. F.; Wan, Q.; Wang, X. L.; Sun, Z. D.; Zhu, Z. Q.; Xian, Y. Z.; Jin, L.T.; Yamamoto, K. *J. Electroanal. Chem.* **2004,** *571*, 133-138.

17. Qiu, J. D.; Guo, J.; Liang, R. P.; Xiong, M. *Electroanalysis* **2007,** *22,* 2335-2341.

18. Ling, X. Y.; Reinhoudt, D. N.; Huskens, J. *Langmuir* **2006,** *22*, 8777-8783.

19. Budny, A.; Novak, F.; Plumeré, N.; Schetter, B.; Speiser, B.; Straub, D.; Mayer, H.A.; Reginek, M. *Langmuir* **2006**, *22,* 10605-10611.

20. Plumeré, N.; Speiser, B. *Electrochim. Acta* **2007,** *53*, 1244-1251.

21. Xu, C.; Aoki, K. *Langmuir* **2004,** *20*, 10194-10199.

22. Jiang, Z.-J.; Liu, C.-Y.; Li, Y-J. *Chem. Lett.* **2004,** *33,* 498-499.

23. Sun, J.; Bayley, P.; MacFarlane, D. R.; Forsyth, M. *Electrochim. Acta* **2007,** *52,* 7083-7090.

24. Winter, M.; Brodd, R. J. *Chem. Rev.* **2004,** *104,* 4245-4269.

25. Arico, A. S.; Bruce, P.; Scrosati, B.; Tarascon, J.-M.; Van Schalkwijk, W. *Nature Mater.* **2005,** *4*, 366-377.

26. Pandolfo, A. G.; Hollenkamp, A. F. *J. Power Sources* **2006,** *157,* 11-27.

27. Ranjan, R.; Brittain, W. J. *Macromol. Rapid Commun.* **2007**, *28*, 2084-2089.

28. a) MW calculation – density of 2.3 g/cm^3 is used to estimate the molar mass for the silica particles. b) Iler, R. K. *The Chemistry of Silica: Solubility, Polymerization, Colloid and Surface Properties, and Biochemistry.* Wiley: NY, 1979; p 22.

29. Caruso, F.; Lichtenfeld, H.; Giersig, M., Mohwald, H. *J. Am. Chem. Soc.* **1998,** *120,* 8523-8524.

30. Albert, K.; Bayer, E. *J. Chromatogr.* **1991,** *544*, 345-370.

31. El Harrak, A.; Carrot, G. ; Oberdisse, J.; Eychenne-Baron, C.; Boué, F. *Macromolecules* **2004,** *37,* 6376-6384.

32. Wagner, C.D.; Riggs, W.M.; Davis, L.E.; Moulder, J.F. In *Handbook of X-Ray Photoelectron Spectroscopy;* Muilenberg, G.E., Ed.; Perkin-Elmer Corporation: Eden Praire, MN, 1979; p 22. Assuming the MW of the nanoparticle (core + monolayer ligand) to be 1.75×10^{6} g/mol, an individual particle would weigh 2.9×10^{-18} g. Multiplying by 0.02 (Fe atomic composition) and dividing by the MW of Fe gives 1.04×10^{-21} g Fe per particle, equaling 630 Fc per particle.

33. Quirk, P. F.; Kratochvil, B. *Anal. Chem.* **1970,** *42,* 535-536.

34. Flanagan, J. B.; Margel, S.; Bard, A. J.; Anson, F. C. *J. Am. Chem. Soc.* **1978,** *100,* 4248-4253.

35. Oh, S.-K.; Baker, L. A.; Crooks, R. M. *Langmuir* **2002,** *18,* 6981-6987.

36. Valério, C.; Fillaut, J.-L.; Ruiz, J.; Guittard, J.; Blais, J.-C.; Astruc, D. *J. Am. Chem. Soc.* **1997,** *119,* 2588-2589.

37. Nlate, S.; Ruiz, J.; Sartor, V.; Navarro, R.; Blais, J.-C.; Astruc, D. *Chem. Eur. J.* **2000,** *6,* 2544-2553.

38. Bard, A. J; Faulkner, L. R. *Electrochemical Methods,* 2nd ed.; Wiley: NY, 2001; p 28-29.

39. Bagotskii, V. S., Ed. *Fundamentals of Electrochemistry;* Wiley: NY, 2006; p66.

40. Charge Density calculation assumes the volume of the particle to be 1.8×10^{-24} m^3; the charge density was calculated from

$$\frac{C}{m^3} = \frac{n \quad F \quad N_A}{V_{NP}}$$

where n is the number of Fc per particle, F is the Faraday constant, N_A is Avogadro's number and V_{NP} is the volume of the particle.

41. Maisonhaute, E; White, P. C.; Compton, R. G. *J. Phys. Chem. B* **2001,** *105,* 12087-12091.

42. Maisonhaute, E.; Brookes, B. A.; Compton, R. G. *J. Phys. Chem. B* **2002,** *106,* 3166-3172.

43. Compton, R. G.; Eklund, J. C.; Marken, F.; Rebbitt, T. O.; Akkermans, R. P.; Waller, D. N. *Electrochim. Acta* **1997,** *42,* 2919-2927.